Studies of excited states in the odd-odd nucleus ^{178}Au

Aaron Matthew Stott

Doctor of Philosophy

University of York
Physics

March 2023

Abstract

Atomic nuclei close to the Z = 82 shell closure are well known for exhibiting shape coexistence with one of the earliest examples of this being the neutron-deficient gold (Z = 79) nuclei close to the neutron mid shell gap at N=104. Subsequently, such isotopes have been examined with both laser-spectroscopy and decay studies.

The present investigation was motivated by the recent experiments at ISOLDE CERN to study the chain of gold isotopes $^{176-181}$Au. In the odd-odd nucleus, ^{178}Au (N=99), two α-decaying states were identified, a low spin ($I^{\pi} = 2^{+}, 3^{-}$) ground state ^{178}Au^{g}, and a high-spin ($I^{\pi} = 7^{+}, 8^{-}$) isomer. Laser-spectroscopy measurements have shown both isomers to be deformed with the high-spin state having slightly larger deformation.

In this thesis, excited states of ^{178}Au (Z=79, N=99) have been established for the first time by means of in-beam γ-ray spectroscopy. The previously established sub-microsecond isomers with half-lives of 294-ns and 373-ns were confirmed and their decay schemes to the α-decaying states of ^{178}Au were established with new multipolarity assignments.

The existence of sub-microsecond isomers of ^{178}Au allowed for isomer decay tagging to be utilised to identify excited states. A total of 3 rotational bands were established. Configuration assignments of these bands has been made on the basis of comparison with similar bands in neighbouring odd-odd Ir isotopes, with the $\pi i_{13/2} \otimes \nu i_{11/2}$ and $\pi h_{11/2} \otimes \nu f_{7/2}$ bands observed in ^{178}Au. The establishment of rotational bands is discussed and may also constrain the the spin-parity of both previously established α-decaying states ^{178}Au^{g,m}.

Declaration

I declare that this thesis is a presentation of original work and I am the sole author. This work has not previously been presented for an award at this, or any other, University. Parts of the work presented in this thesis are published previously in [1]. All sources are acknowledged as references.

Aaron Matthew Stott
March 2023

Acknowledgements

I would like to thank my supervisors: Andrei, your guidance, work ethic, patience and directness have been an inspiration throughout my studies. Stefanos, for the opportunities in Germany and Daresbury, and help in with the L3T which certainly helped in future employment. For both of you thank you for your support particularly in the difficult circumstances throughout 2020/2021.

Thanks to the many academics who have lead me here: Christian, for the opportunities you gave me during my undergraduate, I surely would not have reached this point without you. Ale, for your dry humour, advice and support as both a teacher and advisor. I wish you the best of luck to you and your family in France. To James and Stephen for their advise and help on many aspects of this work.

Thanks to my many colleagues in the nuclear physics group at York. Tetley, Rose, Richard and many others, thank you for sharing great conversations and knowledge, both in the office and the pub!

Finally the greatest thanks goes to my parents for there continued support and for putting up with me during lockdowns and beyond.

My PhD experience has been stranger than most but I think it may have best be summed up by another:

"I may not have gone where I intended to go, but I think I have ended up where I needed to be." - Douglas Adams

Table of contents

List of figures

List of tables

Chapter 1

Introduction

The nuclear shape is one of several properties to characterise the many body quantum system that is the atomic nucleus. The shape is of critical importance to understand as it reflects both the potential, which confines all the nucleons, and also influences the half-life and decay modes of the system. Whilst spherical shapes are seen in *"doubly magic"* nuclei, where the number of protons and neutrons corresponds to shell closures (e.g. ^{4}He, $N = Z = 2$ and ^{40}Ca, $N = Z = 20$), the ground states of most nuclei have the shape of a deformed spheroid. Nuclear deformation is evident with the observation of rotational bands as these bands must be a result of a deformed shape since quantum mechanically a spherical nucleus cannot rotate.

The quadrupole deformation parameter β_2, provides one measure for the deformation of the nucleus, with its value mapped for nuclear ground states in Fig. 1.1 with this quantity directly related to the nuclear quadrupole moment. It can be seen that throughout the chart of nuclides exist a collection of axially-symmetric, prolate and oblate nuclei, with a minority being spherical. Several clear β_2 minima are seen close to the *"magic numbers"* of protons and neutrons ($Z,N = 20,28,50,82...$), indicating spherical ground states for these nuclei. Together with the quadrupole deformation parameter, are higher order terms including that of the octupole-deformation parameter (β_3). This quantity provides a geometric description for more exotic shapes such as that of "pear-shaped" heavy nuclei ^{220,224}Rn [7].

Nuclei can also exist in multiple low energy configurations, each corresponding to different nuclear shapes. This phenomenon is known as "shape coexistence" and was first observed in the doubly-magic nucleus ^{16}O($N = Z = 8$) by Morinaga in 1956 [9]. Whilst the ground state of ^{16}O represents a spherical doubly-closed shell configuration, a rotational band was seen above the first excited 0^+ state and is shown in Fig. 1.2. The presence of this band was completely unexpected for a doubly magic nucleus and meant that whilst the ground state is

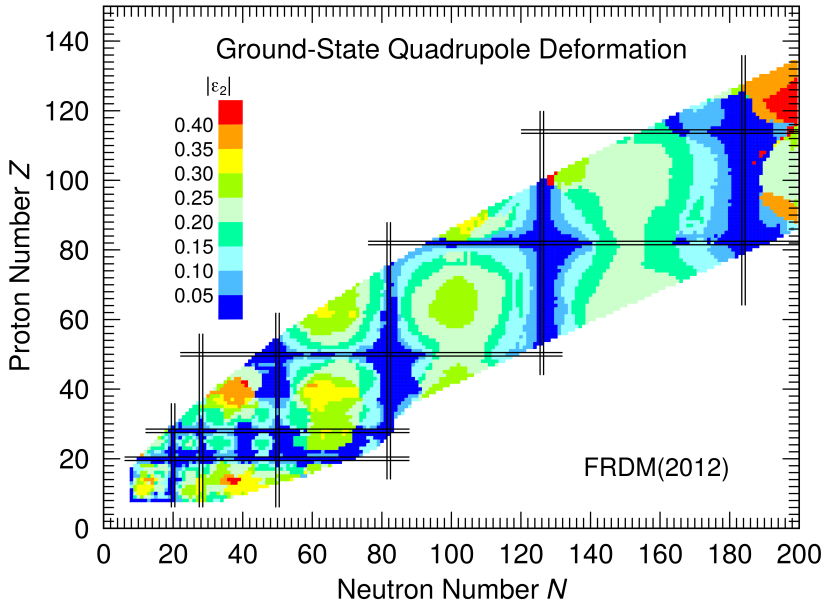

Fig. 1.1 Calculated quadrupole deformation $|\varepsilon_2|$ for nuclei with $N < 200$. Figure taken from [8].

spherical, the first excited 0^+_2 state to which the rotational band feeds, is a deformed shape.

In recent years shape coexistence has been, with the aid of modern experimental techniques, regularly observed throughout the nuclear chart and are most commonly seen close to proton shell closures [11]. Triple shape coexistence, where three distinct shapes exist has been observed in ^{186}Pb [12]. In this unique case it was observed that the same nucleus can occupy a nearly spherical ground state, and two additional low-energy configurations corresponding to a prolate and oblate shape illustrated in Fig. 1.3. A more recent example is that of ^{64}Ni (Z=28, N=36), in which the transition strength of a newly observed 0^+_4 state indicates a prolate shape [13]. This along with previously identified oblate 0^+_2 and spherical 0^+_3 states gives evidence for triple shape coexistence in a stable isotope.

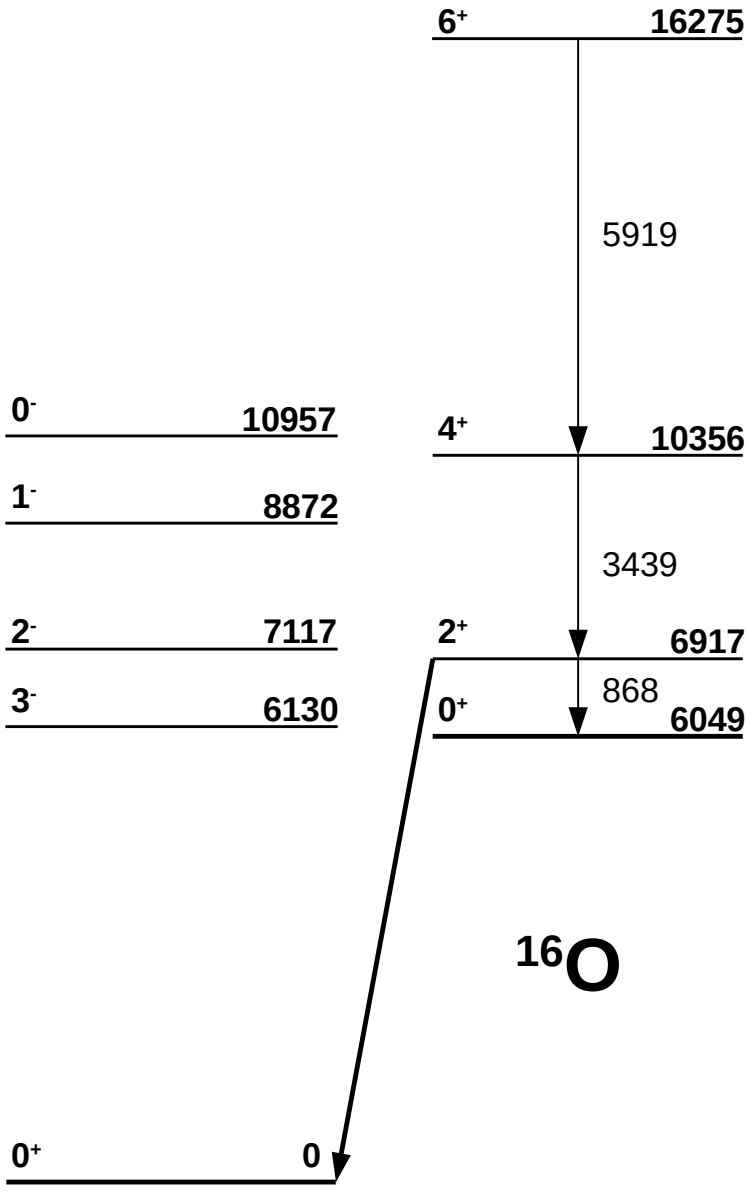

Fig. 1.2 Partial level scheme of ^{16}O. Rotational band above the first excited 0^+ state is shown. Data are taken from [10].

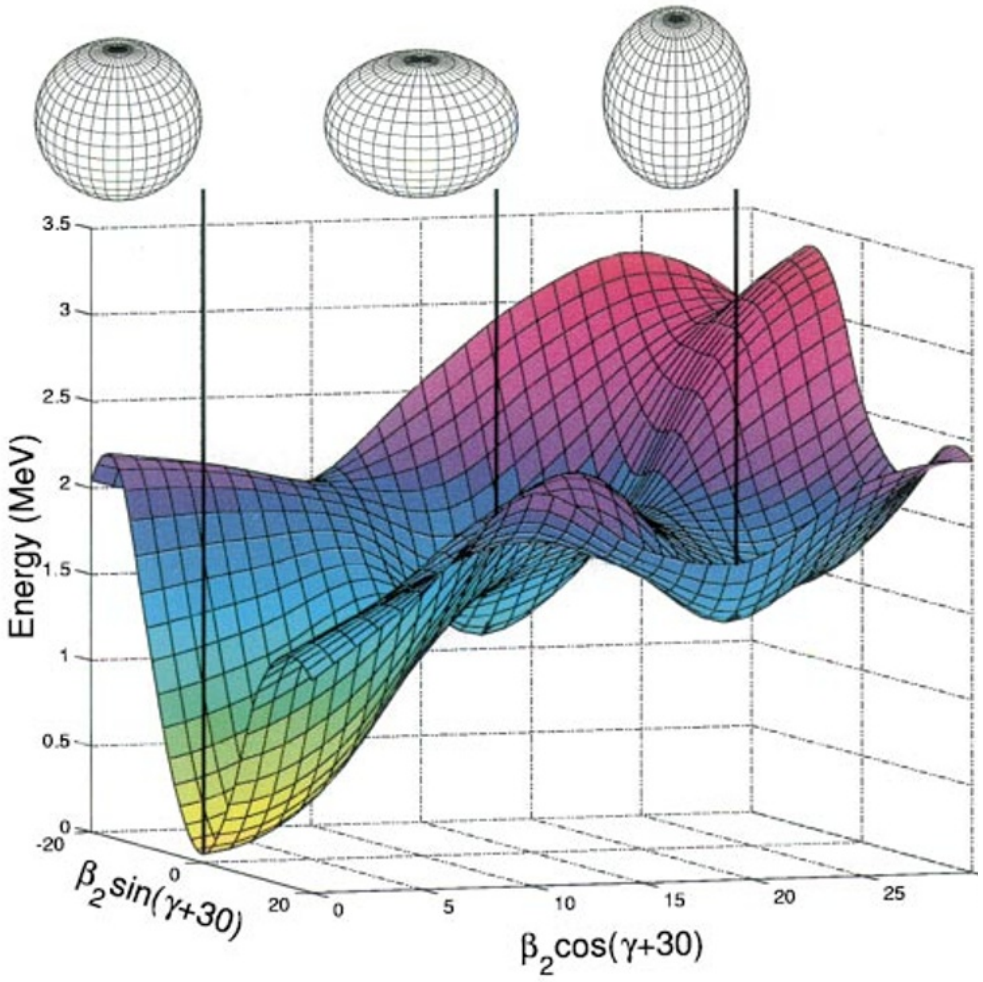

Fig. 1.3 Energy surface of ^{186}Pb, with all three shape configurations demonstrated [12]

1.1 Previous Studies of ^{178}Au and Motivation

Neutron-deficient isotopes close to both the proton shell at Z = 82 and neutron mid-shell at N = 104 lay in a prominent region of low-energy shape coexistence. Alpha-decay studies of nuclei in this region provide a crucial tool in the study of shape coexistence due to the strong overlap of the initial and final states in α-decay. Previous measurements of Au (Z=79) isotopes demonstrate that the charge radii of Au nuclei increase in a smooth manner for ^{187}Au ($N = 108$) upwards as shown in Fig. 1.4. However a sharp jump in the charge radii is seen between ^{186}Au and ^{187}Au, signifying a region of enhanced deformation relative to heavier Au isotopes. This region is explained by the concept of intruder states, where in this case the deformed $\pi 1h_{9/2}$ orbital reduces in energy below that of the normal spherical $\pi 2d_{3/2}$ orbital. This results in the reordering of states with the $\pi 1h_{9/2}$ intruder state inheriting the

ground state in Au nuclei close to the neutron mid shell.

This region of enhanced deformation was observed up to ^{183}Au, however more recently the Windmill collaboration at ISOLDE CERN extended the charge radii data to ^{176}Au, showing that deformation persists up to ^{180}Au, whilst ^{176,177,179}Au become more spherical and two deformed states were identified in ^{178}Au as discussed later.

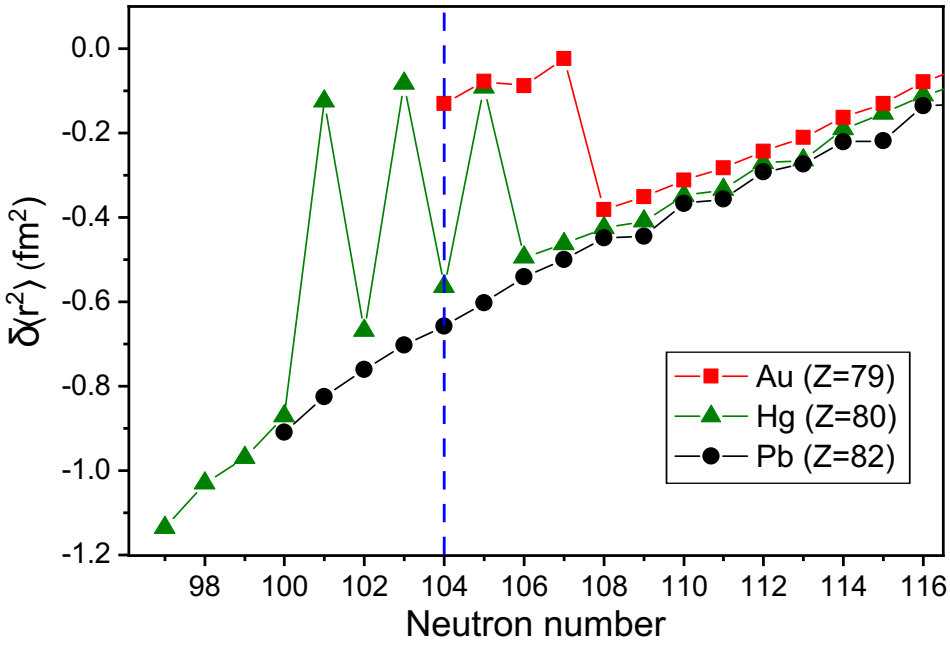

Fig. 1.4 Experimental mean-squared charge radii for isotopes close to the Pb (Z=82) region, relative to stable isotopes, ^{197}Au, ^{206}Hg, and ^{208}Pb. The N=104 mid shell is indicated in blue [14]. Au radii data are up to 1986 and Hg data is taken from [15]

A similar effect is seen in the famous staggering of ground state charge radii in Hg isotopes [15]. In this case, low energy shape coexistence results in two configurations competing for the ground state, resulting in a transition between a strongly deformed and nearly spherical ground state between odd and even mass isotopes.

The first observation of ^{178}Au was made by Siivola *et al.* [17] performing α-decay studies with nuclei produced using fusion evaporation reactions. In this study a single 5920(10)-keV α-decay was attributed to ^{178}Au, with a half-life of 2.6(5) s. The most recent

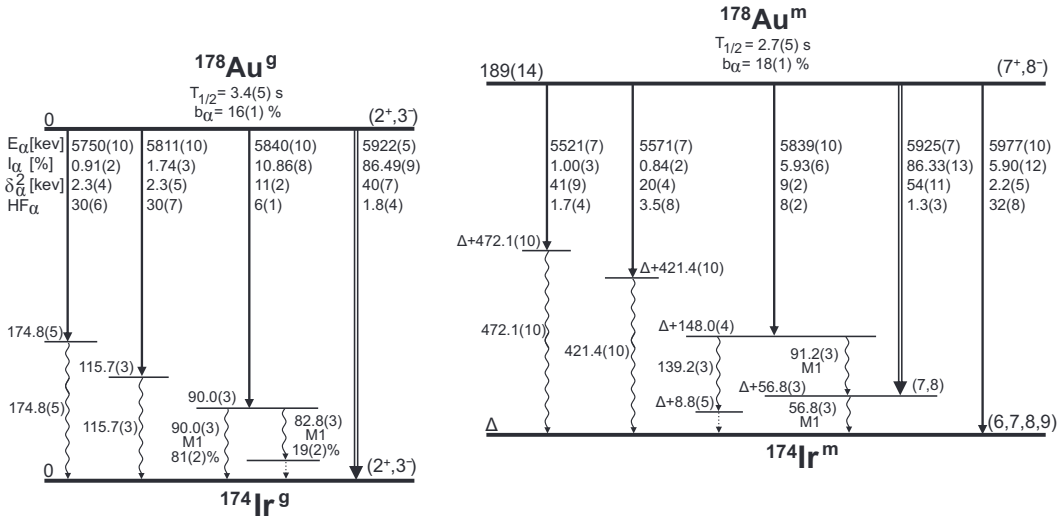

Fig. 1.5 α-decay scheme of ^{178}Au^{m,g} constructed from ISOLDE data [16]

and significant α-decay study of ^{178}Au however, was performed at ISOLDE CERN in 2015 [16]. The study utilised an **I**on **S**ource **O**n**L**ine (**ISOL** method) with an in-source resonant laser ionisation technique produces isotopically-pure as well as isomerically-pure beams. In this work a low-spin $(2^+,3^-)$ ground state ^{178}Au^{g}, and high-spin $(7^+,8^-)$ isomeric state ^{178}Au^{m}, were identified. Possible Nilsson configurations for both states were also discussed with it suggested that the odd neutron occupies the $\nu 5/2^-[512]$ orbital in the ground state and the $\nu 7/2^+[633]$ orbital in ^{178}Au^{m}. The experiment also facilitated the study of excited states in the daughter nucleus ^{174}Ir by analysis of α-γ coincidences. The alpha-decay scheme constructed from the ISOLDE study can be seen in Fig. 1.5. The deformation of both ^{178}Au^{g,m} was also deduced by means of charge radii measurements resulting in a strongly deformed high-spin isomer $\beta_2 \approx 0.3$ and a slightly less deformed ground state $\beta_2 \approx 0.25$ [14].

Excited states of ^{178}Au have previously been observed by means of an α-decay study of ^{182}Tl at ISOLDE [18], however due to the complexity of the α-decay scheme produced (see Fig. 1.6), limited knowledge of ^{178}Au could be established. Similarly an alpha decay study of ^{180}Tl was also performed in which excited states of the daughter ^{176}Au, were identified and a tentative ground state configuration of $\pi d_{3/2} \otimes \nu f_{7/2}$ was assigned [19].

To identify detailed structures of neutron deficient isotopes, in-beam studies are commonly used, of which several exist for light gold isotopes. For example ^{177,179}Au have been produced and studied at the University of Jyväskylä using fusion-evaporation reactions [20, 21]. Utilising both recoil-decay-tagging and isomer-decay-tagging techniques, bands

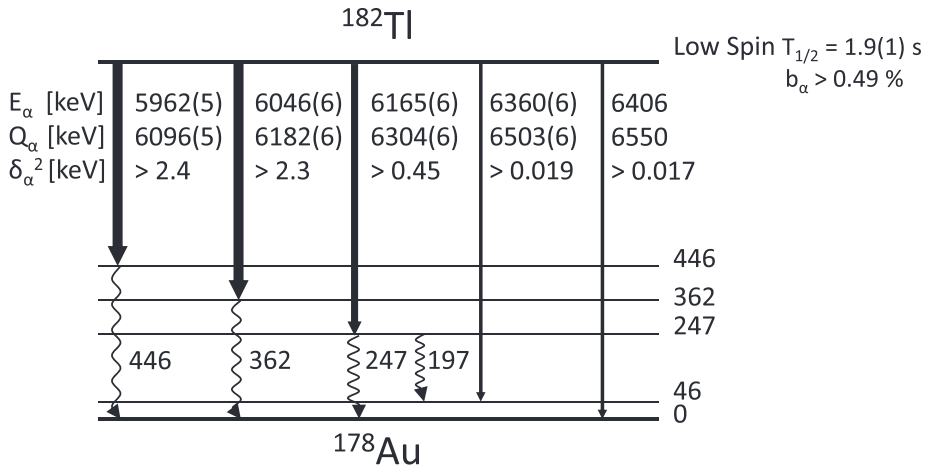

Fig. 1.6 α-decay scheme of ^{182}Tl with populated excited states in ^{178}Au [18].

corresponding to the $1i_{13/2}$ proton-intruder configuration were observed to strongly feed nearly spherical states associated with the $2d_{3/2}$ and $3s_{1/2}$ configurations in both nuclei.

For even-mass Au nuclei, excited states are far less established due the complexity of structures in odd-odd systems. Despite this, level-schemes for ^{174,176}Au were previously established using the recoil-decay-tagging technique with fusion evaporation reactions [22] and the estimated deformation of both nuclei being $\beta_2 \approx 0.12$. For heavier Au nuclei of mass A$\geq$ 182 more complete structures are identified, for example in the case of ^{182}Au [4].

The $\pi i_{13/2} \otimes \nu i_{13/2}$ band is known to be prominent in regions where the $\pi i_{13/2}$ proton orbital has lower energy. This occurs close to N=98 for Ir, and N=102 for Au isotopes. For example, in ^{177,179}Au bands associated with the $\pi i_{13/2}$ proton orbital have been identified [20, 21] and furthermore the $\pi i_{13/2}$ bands are yrast in Au nuclei close to N=98 [23]. For these reasons, the odd-odd ^{178,180}Au (N=99,101) are favourable isotopes to search for the $\pi i_{13/2} \otimes \nu i_{13/2}$ two-quasiparticle band however, no rotational bands of either nuclei are currently established.

Several two-quasiparticle bands in deformed odd-odd nuclei are known to exhibit *signature inversion* at low spins. There are several well-known configurations of bands that show signature inversion including the $\pi h_{11/2} \otimes \nu i_{13/2}$ and $\pi h_{9/2} \otimes \nu i_{13/2}$ [24]. More recently the $\pi i_{13/2} \otimes \nu i_{13/2}$ bands in ^{176}Ir, ^{178}Ir, ^{182}Au, and ^{184}Au have all been shown to exhibit signature inversion [2, 25, 3, 4, 26].

Building on the work of Cubiss *et. al*, in-beam studies of ^{178}Au were performed at the University of Jyväsklyä in 2015, using the JUROGAM-II RITU GREAT setup. This resulted in the identification of two sub-μs isomeric transitions in ^{178}Au by M. H. Al-Monthery [27]. Firstly a 50.3-keV transition with a 300(10)-ns half-life was seen to feed the ground state ^{178}Au^{g}, and the second transition was seen to feed the high-spin isomer ^{178}Au^{m} with an energy of 56.6-keV and 390(10)-ns half-life. Other than the previously mentioned α-decay study of ^{182}Tl, these two transitions were the only identified γ-ray transitions from excited states of ^{178}Au.

This work reports on the same data from the 2015 experiment at University of Jyväsklyä as from Al-Monthery. Identification of the two sub-μs isomeric transitions led to a partial level-scheme for both isomers with an additional 3 transitions with energies 60.0-, 63.4- and 113.4-keV, associated with the 294-ns isomer. Half-life measurements for the isomeric states was also refined with multipolarity assignments given for the isomeric transitions. Knowledge of sub-μs isomers has allowed for the identification of high-spin transitions in ^{178}Au by means of isomer-decay-tagging. This technique facilitates avoiding the recoil-decay-tagging technique that is problematic due to the long half-live and small alpha branching ratio of ^{178}Au.

An overview of models of the atomic nucleus and decays will be given in chapters 2 and 3. Chapter 4 will describe the experimental setup and techniques used for the study of ^{178}Au presented in this thesis.

Chapter 5 presents the results showing the deduced isomeric level scheme for both sub-μs isomers in ^{178}Au and the first ever in-beam γ-ray spectroscopy for ^{178}Au with a total of three rotational bands presented including the $\pi i_{13/2} \otimes \nu i_{13/2}$ band. Chapter 6 discusses the nature of the sub-μs isomers as well as the possible particle configurations and implications for the identified rotational bands in ^{178}Au.

Chapter 2

Nuclear Structure

2.1 Nuclear Models

Since the discovery of the atomic nucleus by Rutherford in 1911 [28], attempts have been made to formulate nuclear models that can capably describe properties of all nuclei. An effective model must be able to reproduce nuclear properties deduced from experiments as well as predicting results from future measurements. The atomic nucleus is a many-body quantum system governed by the complex interactions between protons and neutrons. To avoid such complexities however, many models employ effective theories rather than modelling the nucleus "ab initio". Here a brief introduction of the liquid drop model, spherical shell model and a deformed shell model will be presented.

2.1.1 Liquid Drop Model

One of the earliest and most famous nuclear models devised was the liquid drop model. Formulated in 1935 by Weizsäcker [29], this model treats the nucleus as a spherical incompressible charged liquid drop with radius defined as:

$$R = R_0 A^{1/3}, \tag{2.1}$$

where the approximation of $R_0 \sim 1.2$ fm is often taken and A is the nucleon number. This macroscopic model produces the Bethe-Weizsäcker formula, which gives the total binding energy of a given nucleus (B_{tot}) with contributions from 5 terms representing volume, surface, charge, as well as symmetry effects. The formula is as follows:

$$B_{\text{tot}}(A,Z) = a_V A - a_S A^{2/3} - a_C \frac{Z^2}{A^{1/3}} - a_{sym} \frac{(A-2Z)^2}{A} \pm E_\delta \tag{2.2}$$

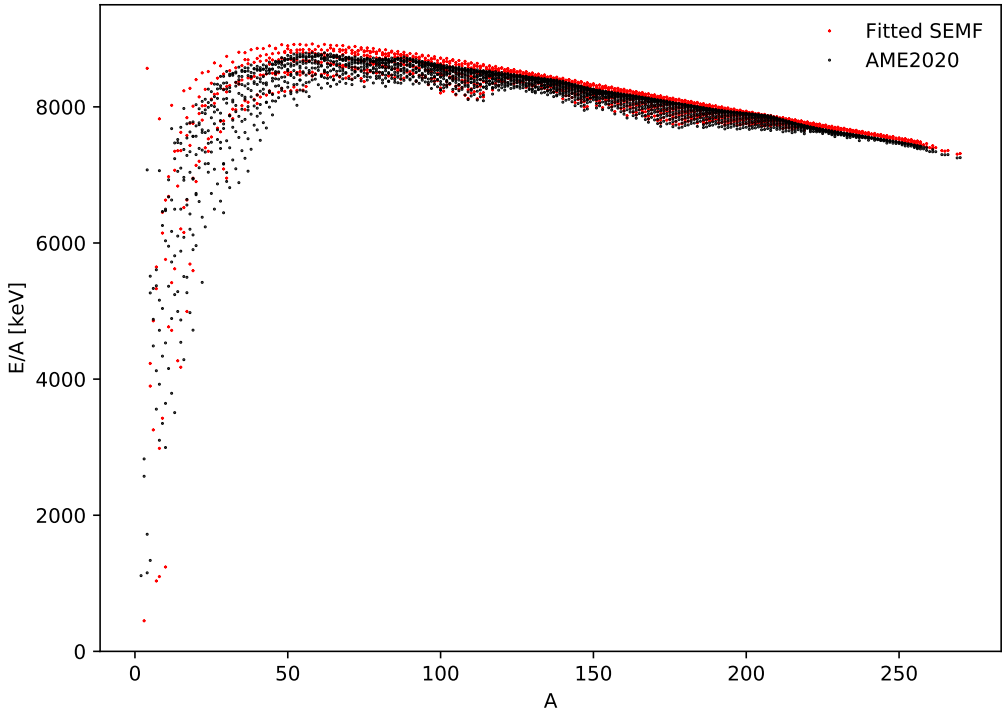

Fig. 2.1 Plot of experimental binding energy per nucleon as a function of mass number (AME2020), along with the SEMF using coefficients $a_V = 15.76$-MeV, $a_S = 17.81$-keV, $a_C = 0.711$-MeV, $a_{sym} = 23.702$-MeV and $E_\delta = 34$-MeV.

In this formula; also referred to as the semi-empirical mass formula (SEMF), Z is the number of protons in the given nucleus. The first term accounts for the volume and as such is proportional to the nucleon number, as the binding energy is proportional to the number of nucleons. The second term corrects for less bound surface nucleons which interact with fewer nucleons than those at the interior of the nucleus and therefore is proportionate to the surface area $A^{2/3}$. The third term corrects for Coulomb repulsion experienced by protons. Therefore this term is proportionate to the charge squared over the nuclear radius ($\frac{Z^2}{A^{1/3}}$). Effects of the Pauli exclusion principle, which states that a single quantum state can only be occupied by a single fermion, are accounted for by the fourth term. This leads to systems with isospin asymmetric $[(N-Z)/A]$ being less energetically favourable than symmetric systems $(N-Z \approx 0)$. Finally, the fifth term accounts for proton and neutron pairing, which produces additional binding energy when compared to single unpaired nucleons. This final term results in E_δ

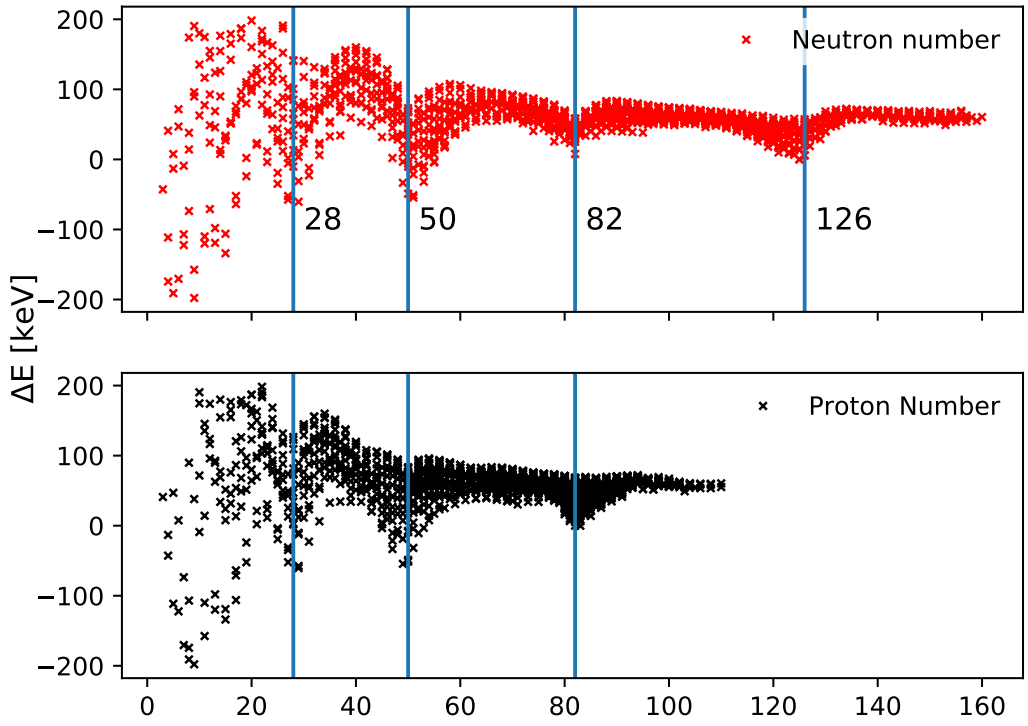

Fig. 2.2 Binding energy difference between the fitted SEMF and experimental data (AME2020) [10] for stable nuclei with magic numbers marked with vertical lines.

being positive for even-even nuclei, negative for odd-odd systems and zero in odd mass nuclei.

The coefficients (a_V, a_S, a_C, a_{sym} and E_δ) are fitted to experimental masses, hence earning its namesake *semi-empirical*. The SEMF gives binding energies close to experimental results in the case of stable nuclei as can be seen in Fig. 2.1. Notably however the SEMF deviates from experimental data at proton and neutron numbers 2, 8, 20, 28, 50, 82 and 126 shown in Fig. 2.2. At these values, known as magic numbers, a large increase in both the binding energy per nucleon when compared to neighbouring nuclei. For this reason the SEMF is not typically used to describe nuclear structure as it fails to incorporate the shell model in the atomic nucleus.

2.1.2 Spherical Shell Model

The nuclear shell model is similar to that of the atomic shell model in that it describes a nucleus as collection of nucleons each with specific orbits (or states) in a similar manner to that of electrons in an atom. The model uses a mean-field potential $V(r)$, which is chosen to replicate interactions between all nucleons. Then each particle is filled into the eigenstates calculated by solving the three-dimensional time-independent Schödinger equation whilst obeying the eigenstate degeneracy of $2j+1$, where $j = l+s$. l is the total angular momentum of the particle and s is its intrinsic spin. Early attempts used the harmonic oscillator potential of the form,

$$V(r) = -V_0[1-(r/R)^2], \tag{2.3}$$

Where V(r) is the potential at a distance r from the center of the nucleus, R is the nuclear radius and V_0 is the depth of the potential. The solution of the Schödinger equation for the harmonic oscillator gives eigenstate energies dependent on the principal orbital number N,

$$E = \hbar\omega_0[2(N-1)+l]+E_0 \tag{2.4}$$

$$\omega_0 = (\frac{2V_0}{MR^2})^{1/2}. \tag{2.5}$$

Here $E_0 = 3/2\hbar\omega_0$ and M is the nucleon mass. This approach reproduced the shell-closure gaps at the known magic numbers 2, 8 and 20, however, was unable to produce the additional magic numbers at 28, 50, 82, and 126 which had been previously identified. A small improvement was the development of the more realistic Wood-Saxon potential [30],

$$V_{WS}(r) = \frac{-V_0}{1+exp(\frac{r-R_m}{a})}. \tag{2.6}$$

This gives the potential at distance r from the centre of a nucleus with mean radius R_m. V_0 gives the depth of the nuclear potential at the centre where $V_0 \sim 50$ MeV. The Wood-Saxon potential produces shell gaps at 2, 8, 20, 40 and 70. Whilst these shell gaps are consistent with magic numbers also reproduced from the harmonic oscillator they deviate from the fourth shell onward. The solution, found by Mayer in 1949 [31], was to include a spin-orbit term $\vec{l}.\vec{s}$. This additional term results in the splitting of levels by the nucleon intrinsic angular momentum and spin, and is introduced by perturbation of the potential,

$$V_{so} = V(r)l \cdot s. \tag{2.7}$$

Due to this additional term, the angular momentum l, is no longer a good quantum number. Whilst the Hamiltonian is still spherical it commutes with the total angular momentum,

$$j = l + s, \tag{2.8}$$

in the nuclear case $s = 1/2$ so we have,

$$\langle l \cdot s \rangle = \begin{cases} l\frac{\hbar^2}{2} \text{ for } j = l + 1/2 \\ -(l+1)\frac{\hbar^2}{2} \text{ for } j = l - 1/2 \end{cases} \tag{2.9}$$

This results in a repulsive force for intrinsic spin-up giving lower energy, and an attractive force for the intrinsic spin-down increasing binding. This leads to the splitting and reordering of $l \neq 0$ states with effect of spin-orbital coupling shown in Fig. 2.3.

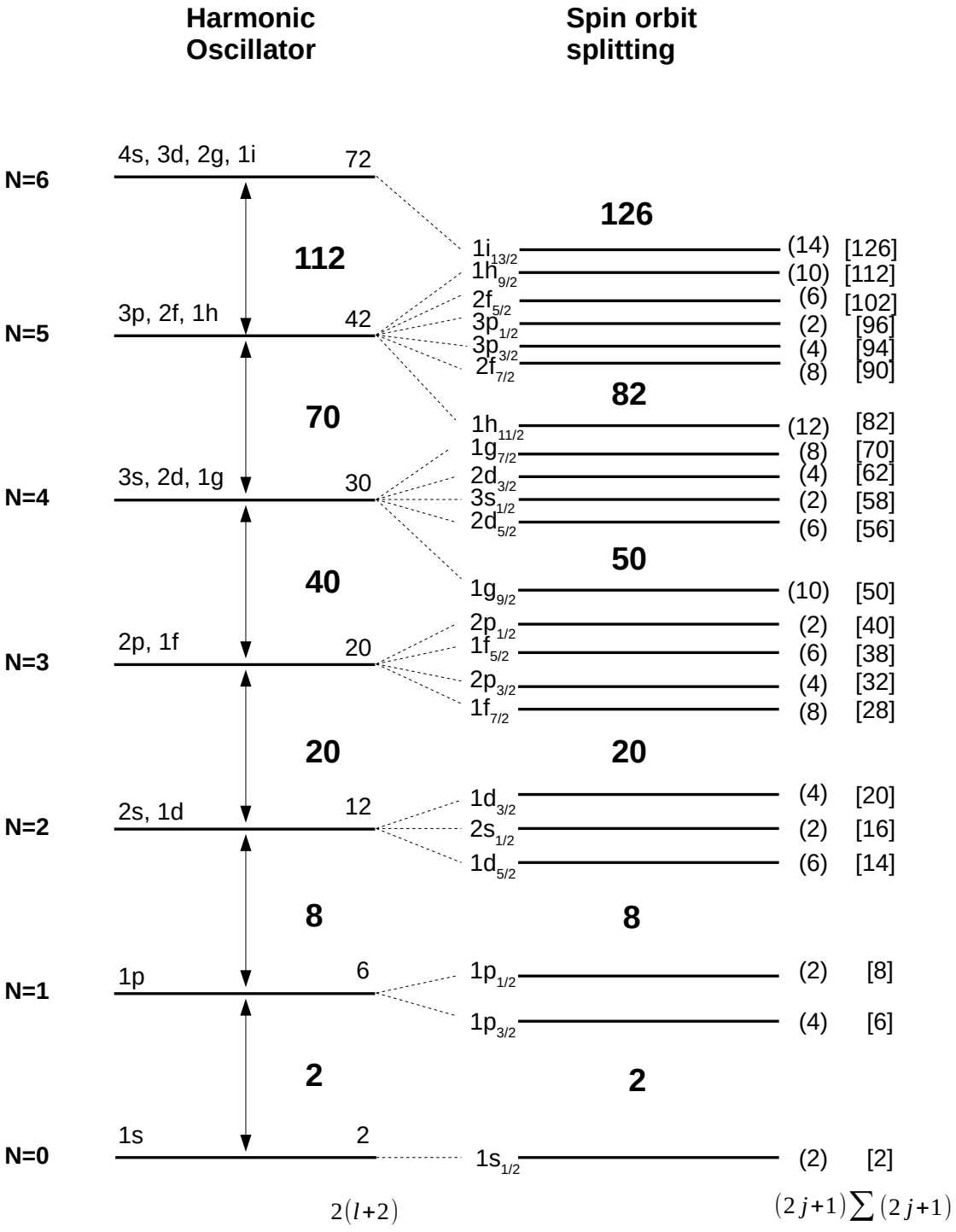

Fig. 2.3 Diagram of orbitals obtained from the spherical shell model with a harmonic oscillator potential (left) and the inclusion of spin-orbit coupling (right). The cumulative occupancy of shell gaps is shown in the final column. Spin-orbit corrections results in magic numbers at the shell gaps.

2.1.3 Deformed Shell Model

Whilst the Shell Model is successful in describing nuclei close to the magic numbers, it fails to accurately describe those outside of the closed shells. This can be attributed to the assumption of spherical symmetry which is regularly inaccurate. In 1955 a *deformed shell model*, was developed by Nilsson and Mottelson [32, 33] adding the effect of deformation on the shell-model states. The model is a modification of the spherical shell model introducing a quadrapole deformation perturbation to the potential. This breaks the $2j+1$ degeneracy present in the spherical shell-model states as the potential is different depending on the orientation relative to the deformed core and forms new Nilsson states with a degeneracy of 2.

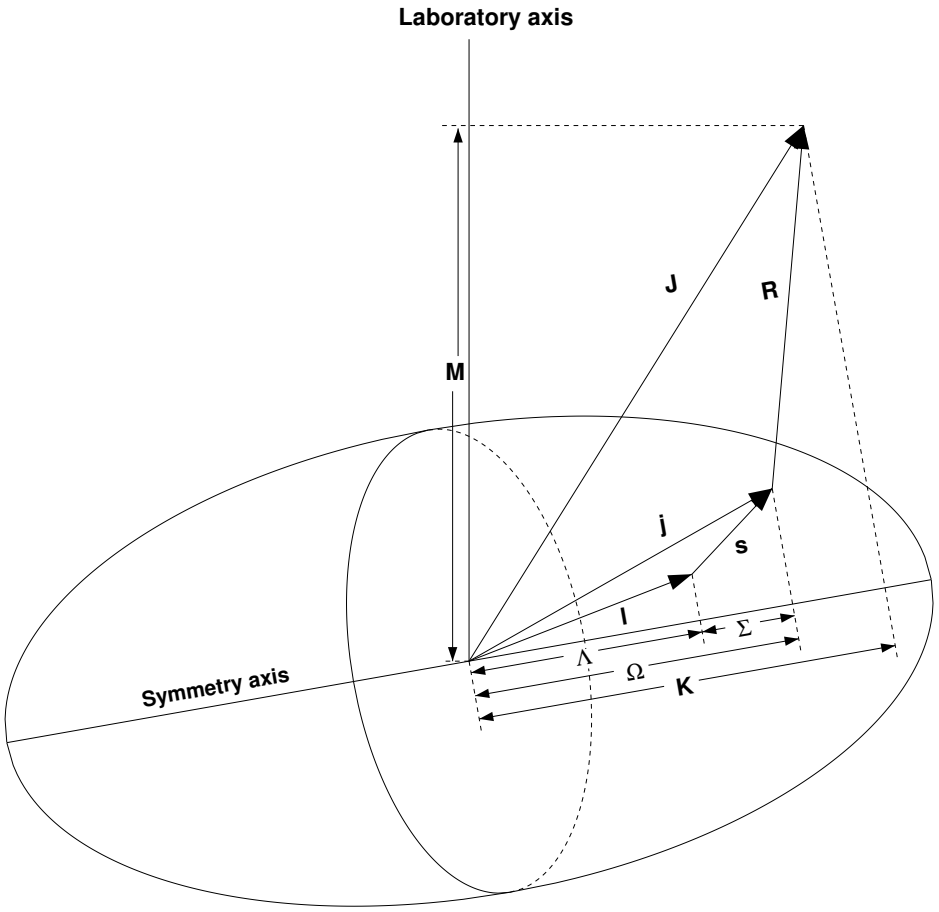

Fig. 2.4 Asymptotic quantum numbers for the Nilsson model. Taken from [6].

These new Nilsson orbitals are labelled with new asymptotic quantum numbers, $\Omega^{\pi}[Nn_z\Lambda]$ described in Fig. 2.4; Ω, the projection of the total angular momentum $(j = l+s)$ on the

symmetry axis; N, the total oscillator shell number; n_z, the number of the oscillator quanta in the z direction; and Λ, the projection of the angular momentum, l, on the symmetry axis such that $\Omega = \Lambda + \Sigma$ where Σ is the projection of the intrinsic spin. Nilsson level diagrams for protons and neutrons in the mass region of deformed rare-earth nuclei, are shown in Fig.2.5 and 2.6. In these plots the single-particle energies are plotted as a function of the Nilsson quadrupole deformation parameter ε_2 defined as

$$\varepsilon_2 = \delta + \frac{1}{6}\delta^2 + \frac{5}{18}\delta^3 + \frac{37}{216}\delta^4 + ... \tag{2.10}$$

Here $\delta = \frac{\Delta R}{R_{rms}}$ where ΔR is the difference in the semi-major and semi-minor axes of the ellipsoid nucleus. The quadrupole deformation parameter β_2 is related to the Nilsson quadrupole deformation parameter ε_2 by

$$\beta_2 = \sqrt{\frac{\pi}{5}} \sum_{n=1}^{\infty} (\frac{4}{3^n}\varepsilon_2^n) \tag{2.11}$$

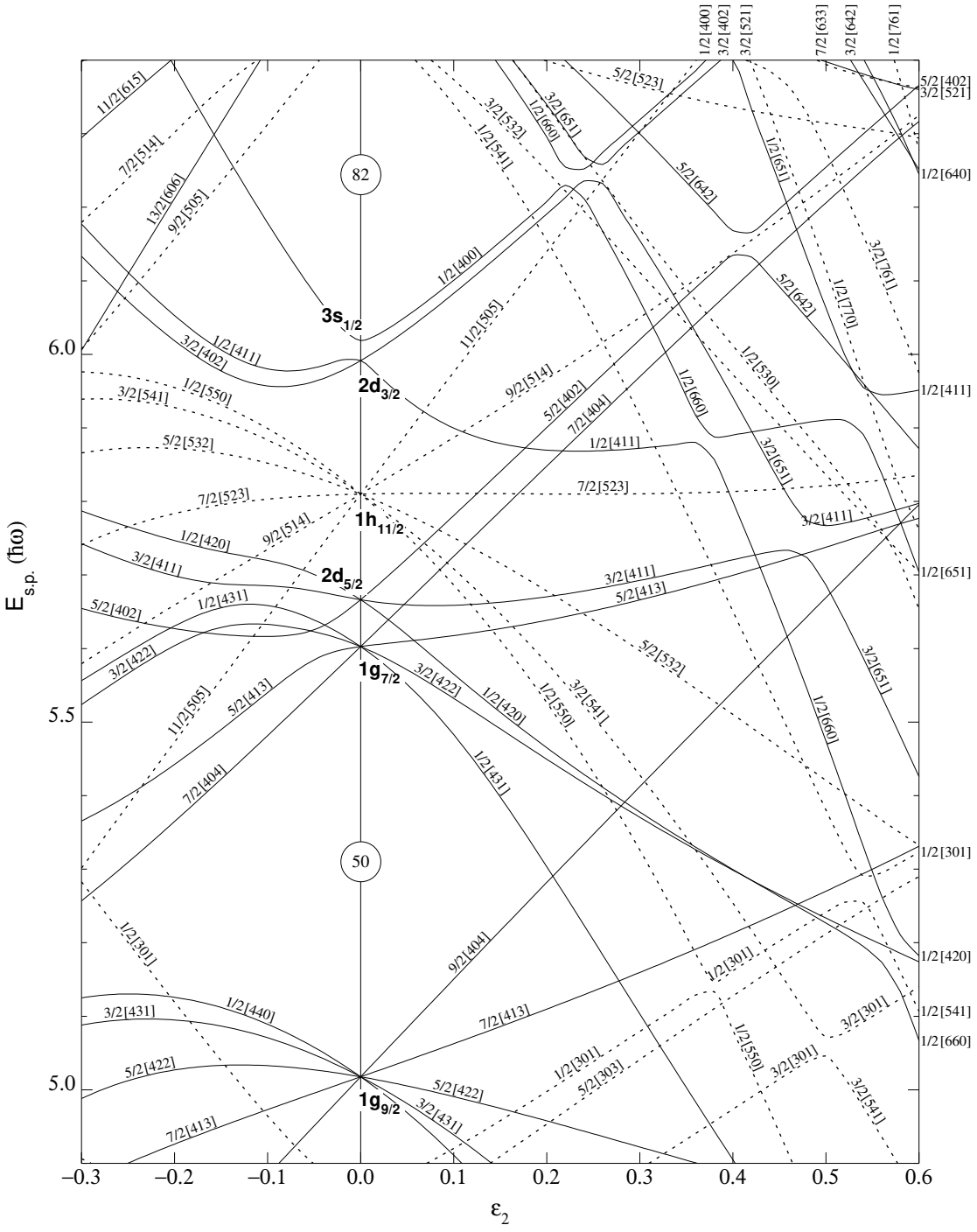

Fig. 2.5 Nilsson diagram for protons $50 \leq Z \leq 82$, calculations performed by [34]. Figure taken from [6].

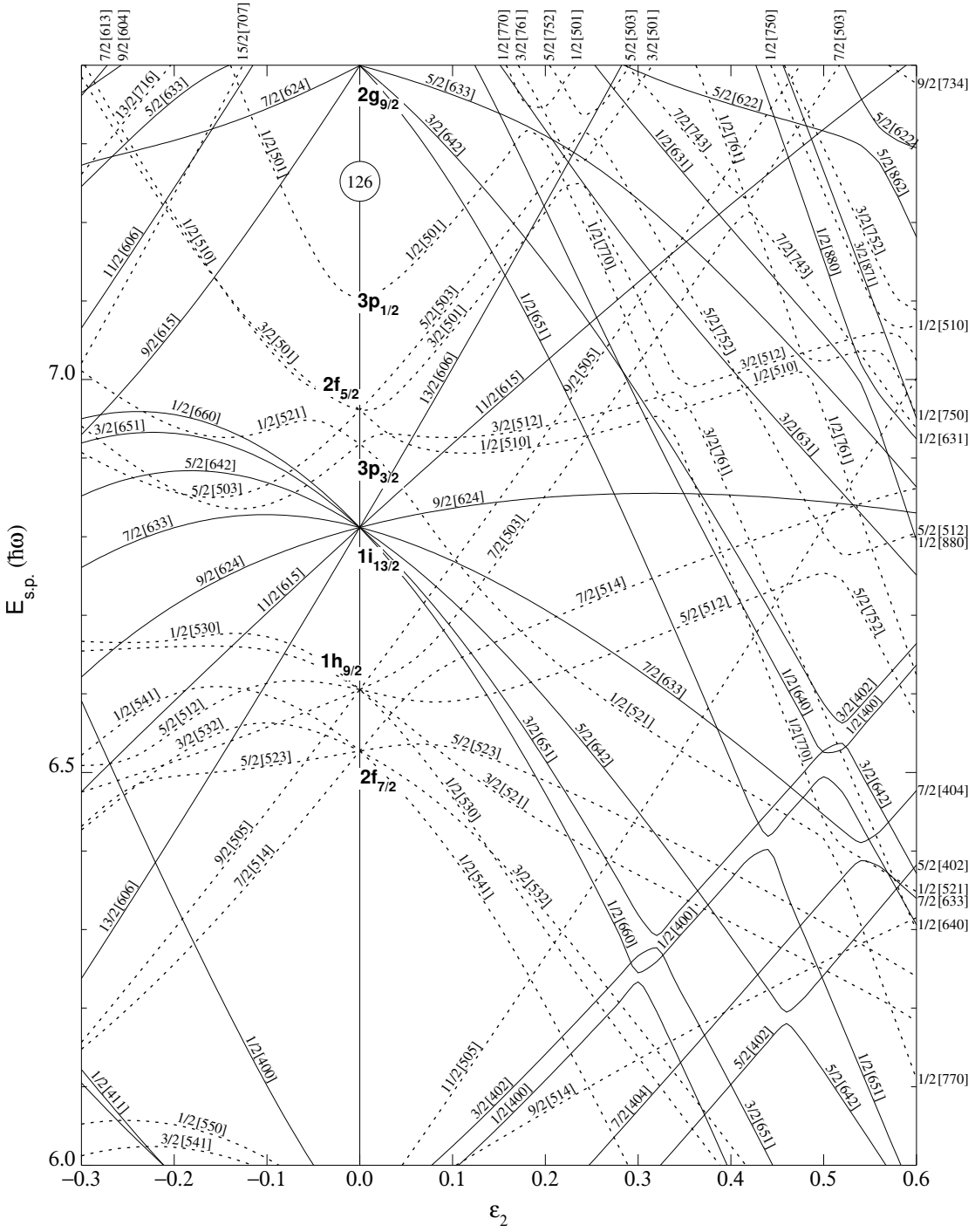

Fig. 2.6 Nilsson diagram for neutrons $82 \leq N \leq 126$, calculations performed by [34]. Figure taken from [6].

2.2 Collective models

The nuclear shell-model can give excellent explanations for low-lying excited states in odd-odd mass and odd-odd nuclei with extremely high accuracy close to the large shell gaps. Some phenomena however, cannot be explained by the shell model alone, but can be well described by collective models to explain such effects as vibrational and rotational states.

2.2.1 Vibrational states

In an atomic nucleus, any deformation results in an increase in the surface area and the surface term energy. For small increases in deformation, however this increase is parabolic. We can therefore consider the nucleus oscillating around its spherical minimum similar to a harmonic oscillator. Considering the surface as a function of time $R(t)$ at polar angles (θ, ϕ), the vibration of the nucleus can be described as:

$$R(t) = R_{av}\left[1 + \sum_{\lambda \geq 1} \sum_{\mu=-\lambda}^{+\lambda} \alpha_{\lambda\mu}(t) Y_{\lambda}^{\mu}(\theta, \phi)\right] \tag{2.12}$$

Here the parameter α describes the time dependent amplitudes around R_{av}, the average radius. $Y_{\lambda}^{\mu}(\theta, \phi)$ gives the spherical harmonics up to λ. λ describes each vibrational mode. $\lambda = 0$ (*monopole*) is forbidden in a liquid drop so is incorporated as $R_a v = R_0 A^{1/3}$. $\lambda = 1$ gives the *dipole* vibration, giving net displacement from the centre of mass. $\lambda = 2$ is the *quadrupole* vibration, where the nucleus oscillates from a prolate to oblate.

2.2.2 Nuclear Rotation

It is known that deformed nuclei exhibit collective rotational bands, considered as a series of excitations involving contributions of many nucleons. The excitation energy, E, for rotational bands is usually found to behave consistently as,

$$E_{rot} = \frac{\hbar^2}{2\Im} I(I+1) \tag{2.13}$$

Where $\Im$ is the static moment of inertia and I is the spin of the excited state. The classical model of the rigid rotor gives an equivalent result to Eqn 2.13

$$E_{\text{rot}} = \frac{1}{2}\Im\omega^2 \tag{2.14}$$

Where ω is the angular frequency of the rotor and $\omega = \frac{I}{\Im}$. This results in a series of states with continuously increasing energies and angular momenta known as a *rotational band*. The rigid-rotor approximation gives the well known result for an even-even rotational nucleus: $\frac{E(4^+)}{E(2^+)} = 3.33$. The lowest state of the band is referred to as the *bandhead*, K, with the possibility of several bandheads existing in a single nucleus corresponding to distinct configurations and rotational sequences. For a given angular momentum, the state with the lowest excitation energy is named the *yrast* state, with the locus of these states being the yrast line.

The static moment of inertia itself, depends on the shape of the object. For an ellipsoid this is given by:

$$\Im = \frac{2}{5} M R_{av}^2 (1 + 0.31\beta_2) \tag{2.15}$$

Where the deformation parameter β is related to the ellipsoid:

$$\beta_2 = \frac{4}{3}\sqrt{\frac{\pi}{5}}\frac{\Delta R}{R_{rms}} \tag{2.16}$$

Moments of Inertia

It is experimentally found that the static moment of inertia for a rotating nucleus is typically between 30-60% of the rigid body prediction. This is particularly due to pairing correlations in the nucleus and the fact that the nucleus has some fluidity. To better reveal the nuclear structure two quantities known as the the *kinematic* and *dynamic* nuclear moments of inertia were introduced and described by Bohr and Mottelson in 1981 [35]. The kinematic moment of inertia is expressed

$$\Im^{(1)} = \hbar \frac{I_x}{\omega} \tag{2.17}$$

and the dynamic moment of inertia as

$$\Im^{(2)} = \hbar \frac{dI_x}{d\omega} \tag{2.18}$$

Here I_x is the total aligned angular momentum on the rotational axis. This quantity is defined relative to the bandhead with spin K by the relation,

$$I_x = \sqrt{(I + \frac{1}{2})^2 - K^2} \tag{2.19}$$

These nuclear moments of inertia reflect changes in the rotational band with the kinematic moment, $\Im^{(1)}$, generally describing the nuclear rotation for a given rotational frequency ω and angular momentum I. The dynamic moment, $\Im^{(2)}$, is used additionally and is highly sensitive to the alignment. In the case of a classical rigid rotor the two nuclear moments of inertia are equal.

To extract the $\Im^{(1)}$ and $\Im^{(2)}$ experimentally, the known γ-ray energies for a rotational band of stretched quadrupole transitions can be utilised,

$$\Im^{(1)} = \frac{2I-1}{E_\gamma}\hbar^2 \tag{2.20}$$

$$\Im^{(2)} = \frac{4}{\Delta E_\gamma}\hbar^2 \tag{2.21}$$

where E_γ is the transition and ΔE_γ is the difference in energy between two successive γ-ray transitions. The rotational frequencies ω are experimentally obtained similarly using the expression,

$$\omega = \frac{dE}{dI_x} = [E(I+1) - E(I-1)]/[I_x(I+1) - I_x(I-1)]. \tag{2.22}$$

In order to isolate the effects of the aligned angular momentum (i_x) generated by the valence particles, the angular momentum of a reference rotor is subtracted from I_x,

$$i_x = I_x - I_{ref} \tag{2.23}$$

The reference angular momentum, I_{ref}, of the reference rotor is taken from the Harris expansion [36] as:

$$I_{ref}(\omega) = (J_0 + J_1\omega^2)\omega/\hbar \tag{2.24}$$

J_0 and J_1 are the Harris parameters and are usually adjusted such that the "core" characteristics of the moment of inertia are reproduced. If a nucleus with a number of odd neutron and/or an odd number of protons is studied then usually the parameters of the closest even-even core is taken. Plotting the aligned angular momentum against the rotational frequency of the nucleus can be used to show the single-particle effects. If there is sudden change in the relationship then this can be interpreted as a breaking of a pair of nucleons, known as back-bending. The theoretical interpretation is described by considering the Coriolis force in the nucleus. As the rotational frequency increases the Coriolis force ($= \omega \times v$) break a pair of two nucleons moving in the time reversed orbits and align their angular momenta along

the axis of rotation. When this occurs a sharp increase of the aligned angular momenta as a function of the rotational frequency will be observed resulting in a smaller energy between levels.

2.2.3 Signature

Each single-particle Nilsson configuration will have a lowest energy state at $J = K = \Omega$ with a corresponding distinct rotational band taking energies described in Eqn 2.13. Additionally, for a rotating system both Coriolis and centrifugal forces introduce an extra term involving a phase factor $\sigma = (-1)^{J+K}$. This is referred to as the signature and is the quantum number associated with the rotation operator. An alternating sign for successive J values results in two distinct families of rotational bands (for $K \neq 0$). The signature α is obtained for even mass nuclei represented by two quasiparticle sequences described by [37],

$$\begin{aligned} \alpha_t &= 0, J = 0, 2, 4, 6, ... \\ \alpha_t &= 1, J = 1, 3, 5, 7, ... \end{aligned} \tag{2.25}$$

In deformed odd-odd nuclei, the Coriolis force is expected to favour the signature α_f of a two-quasiparticle band such that,

$$\alpha_f = \frac{1}{2}[(-1)^{j_p - 1/2} + (-1)^{j_n - 1/2}] \tag{2.26}$$

where j_p and j_n are the angular momentum of the quasi- proton and neutron respectively. This can present itself in signature splitting, where the relative energy of both signatures differs usually favouring α_f. In some cases however Eqn.2.26, can be violated giving rise to *signature inversion*, where α_f is not favoured. A variety of explanations are given for this phenomena including a residual proton-neutron pairing force which counters the Coriolis [2].

2.3 Low energy shape coexistence

Low-energy shape coexistence is a phenomenon in which an isotope has multiple configurations of protons and neutrons, forming low-energy quantum states each resulting in a distinct nuclear deformation and shape. In such systems, each state exists in a local energy minima and if both configurations have similar energies they "compete" to be the ground state in the same nucleus. This competition can be observed in the example of Hg isotopes,

in which dramatic shape staggering is observed as seen in Fig. 2.7, where for odd mass Hg isotopes in the range $180 \leq A \leq 186$ the deformed state becomes the ground-state over the more spherical state.

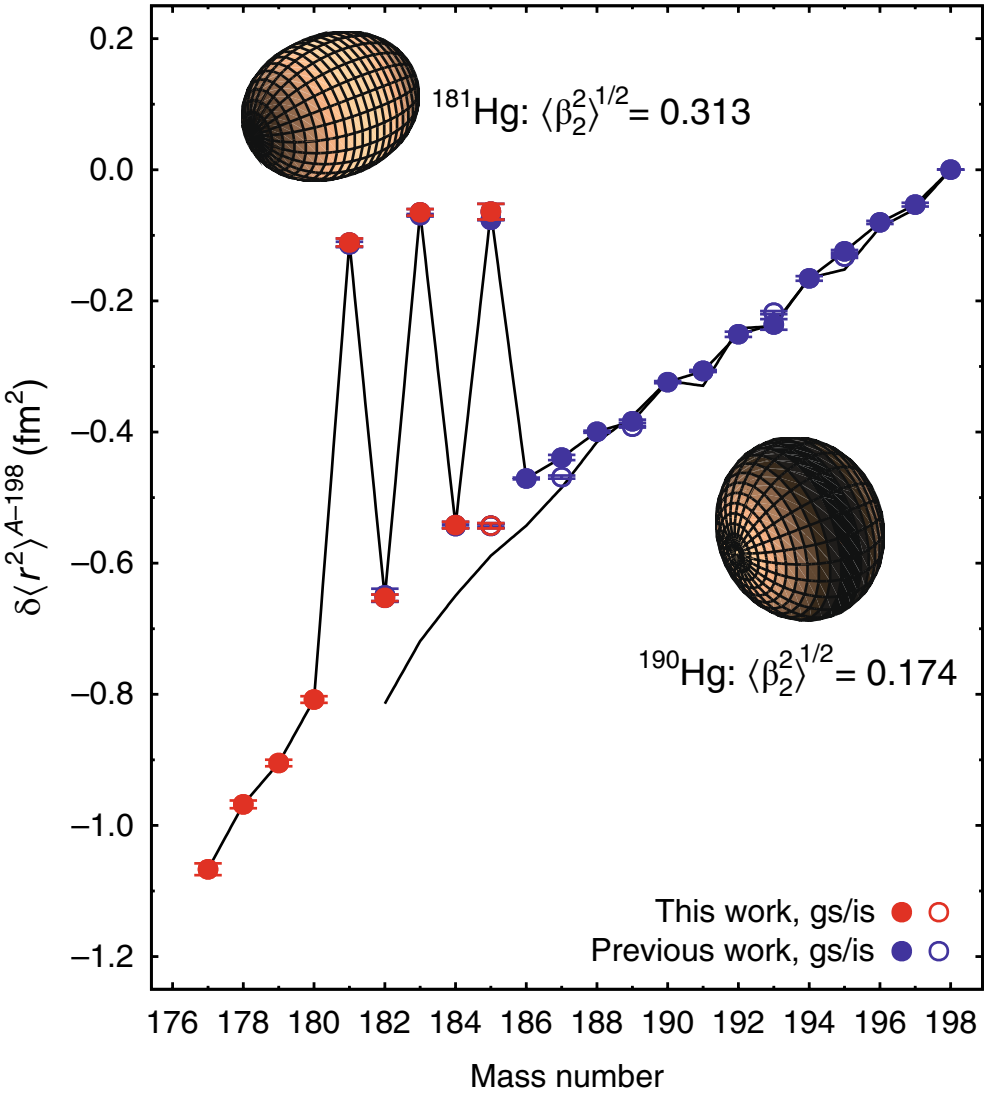

Fig. 2.7 Change in mean-square charge radius, $\delta\langle r^2\rangle$, for the Hg isotope chain $^{177-196}$Hg, relative to ^{198}Hg. The solid black line indicates the trend followed by spherical Pb isotopes. Figure taken from [15].

Shape coexistence was first observed in ^{16}O in which the first two 0^+ states have different configurations and shapes [9], but since then shape coexistence has been found in many

regions of the nuclear chart as covered in a recent review by Heyde and Wood[11].

The concept of *"intruder states"*, in which a single-particle state from the next major shell intrudes below the lower shell due to the deformation of the nucleus, is one interpretation of shape coexistence. Energies of intruder states are lower than is predicted by the spherical shell model ($\varepsilon_{j\pi} - \varepsilon_{j'\pi}$) due to three effects. The energy of the intruder state is calculated as,

$$E_{intruder} = 2(\varepsilon_{j\pi} - \varepsilon_{j'\pi}) - \Delta E^{\pi\pi}_{pair} + \Delta E^{\pi\nu}_{M} + \Delta E^{\pi\nu}_{Q}, \tag{2.27}$$

The three effects described are first, $\Delta E^{\pi\pi}_{pair}$, the pairing correction where an increase in the binding energy of the nucleus is caused by the pairing of two protons ($\pi\pi$). Second, $\Delta E^{\pi\nu}_{M}$, describes the monopole correction in which the single particle energy of a proton can be changed by the neutron number, where the proton-neutron can be attractive or repulsive. The final term, $\Delta E^{\pi\nu}_{Q}$ describes the proton-neutron quadrupole binding energy. In the framework of the Nilsson model intruder states naturally occur as a result of a deformed mean-field potential [11].

Chapter 3

Radioactive Decay

Radioactive decays provide an excellent probe in the study of the atomic nucleus. Here the α, β and electromagnetic decay will be introduced with some theoretical background.

3.1 Alpha Decay

Alpha decay is the process by which an atomic nucleus emits a helium-4 nucleus ($^4_2\mathrm{He}^{2+}$) as a result of the repulsive Coulomb force. The strength of the Coulomb force is proportional to $Z_1 Z_2$ meaning it can quickly compete with nuclear force in heavy elements. The alpha particle is an ideal emission particle as it is the lightest doubly magic nucleus, having a large binding energy. The process for alpha-decay of a nucleus X decaying to a daughter Y is written as,

$$^A_Z X_N \longrightarrow ^{A-4}_{Z-2} Y_{N-2} + \alpha, \tag{3.1}$$

where A and Z are the mass and proton numbers respectively. The total energy released in this process (Q_α), is equal to the change in binding energy between the parent nucleus and the alpha particle, daughter pair,

$$Q_\alpha = (m_X - m_Y - m_\alpha)c^2 \tag{3.2}$$

The energy released in the decay is in the form of kinetic energy. This is distributed to both the α particle (T_α) and the daughter nucleus, ($\mathrm{T}_{\mathrm{recoil}}$) such that $\mathrm{Q}_\alpha = \mathrm{T}_\alpha + \mathrm{T}_{\mathrm{recoil}}$. The α particle emitted during a decay has a sufficiently low velocity that classical mechanics gives a good approximation of the Q-value relation.

$$Q_\alpha = T_\alpha \left[1 + \frac{m_\alpha}{m_Y}\right]. \tag{3.3}$$

As well as the classically derived energy of the α particle, angular momenta and parity selection rules are also obeyed. The angular momenta of an α-particle (I_α) from an initial and final state momentum I_i and I_f respectively will be in the range $|I_i - I_f| \leq I_\alpha \leq I_i + I_f$. The change in parity of such decays is $(-1)^{L_\alpha}$. These selection rules result in several "allowed" combinations of spin-parity decays resulting in an α-decay fine-structure in which each decay populating a different state in the daughter nucleus.

The quantum mechanical model of alpha decay was developed simultaneously in 2 publications by Gamow [38] and by Gurney and Condon [39] and is illustrated in Fig. 3.1. The model assumes a preformed alpha particle confined inside the Coulomb barrier of spherical nucleus. The potential barrier in such a system is typically greater than the Q_α so classically the particle cannot be emitted. However in quantum mechanics, tunneling can occur meaning there is a non-zero probability for alpha particle to penetrate the potential barrier and be emitted from the nucleus.

The potential (Coulomb) barrier on the alpha particle is defined as:

$$V(r) = \frac{1}{4\pi\varepsilon_0}\frac{2Z^{'}e^2}{r} \tag{3.4}$$

Where $Z^{'}$ is the daughter proton number. The point where the alpha particle leaves the nucleus is defined as when $Q_\alpha = V(r)$ and is given by:

$$\mathrm{b} = \frac{1}{4\pi\varepsilon_0}\frac{2Z^{'}e^2}{Q_\alpha}. \tag{3.5}$$

Solving the Schödinger equation gives the probability of tunneling:

$$P \approx e^{-2k_2\cdot(1/2)(b-r)}, \tag{3.6}$$

where k_2 is the wavenumber. This model of α-decay does however assume that the probability a preformed α-particle exists inside the nucleus is 100%. In reality this probability, known as the preformation factor (f), is also implemented to give a more accurate probability of alpha emission,

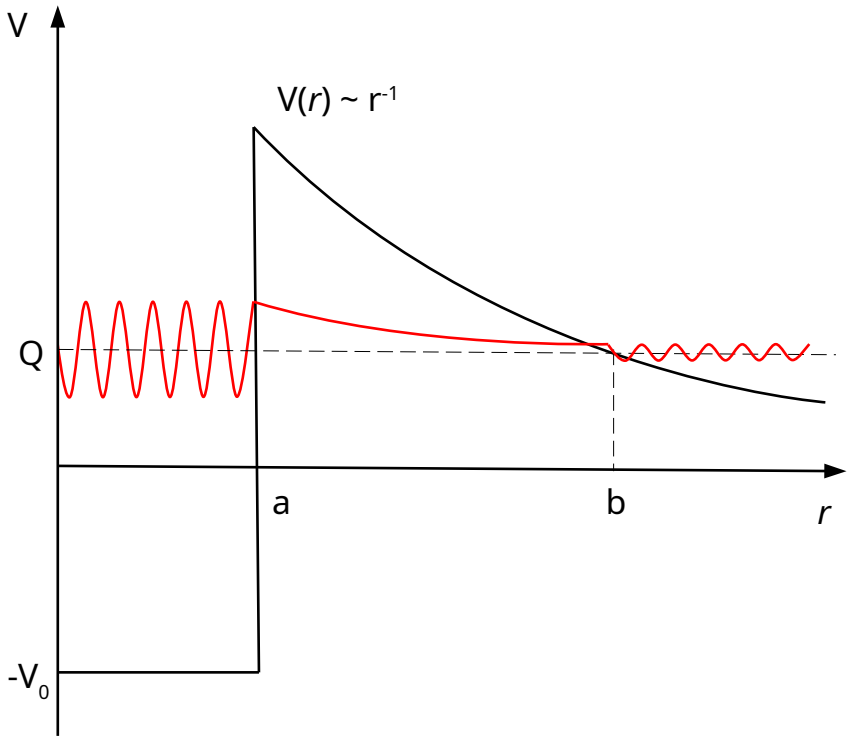

Fig. 3.1 A schematic of an α-particle in a one-dimensional square well potential. The α-particle tunnels through the potential barrier (a-b) which consists of a Coulomb and centrifugal component. Figure recreated from [40].

$$\lambda = f \cdot P \tag{3.7}$$

The preformation factor is highly dependent on the structure of both the initial and final nucleus. Whilst the prediction of the preformation factor can be theoretically extremely complex, it can be derived experimentally as the ratio between the measured and calculated half-life of an alpha-decay [41].

3.2 Electron capture and beta decay

There are three types of decay commonly referred to as beta-decay, these being beta-minus (β^-), beta-plus (β^+), and electron capture (EC). Beta decay involves the emission of β-particle with an electron (e^-) in β^- or its antiparticle the positron (e^+) in the case of β^+ decay. The decay mechanisms are as listed,

$$\begin{aligned} \beta^-&: {}^A_Z X_N \longrightarrow {}^A_{Z+1} Y_{N-1} + e^- + \bar{\nu}_e \\ \beta^+&: {}^A_Z X_N \longrightarrow {}^A_{Z-1} Y_{N+1} + e^+ + \nu_e \\ \mathrm{EC}&: {}^A_Z X_N + e^- \longrightarrow {}^A_{Z+1} Y_{N+1} + \nu_e \end{aligned} \tag{3.8}$$

Each of these processes results in a proton changing to a neutron or vice versa via the weak interaction. As with other decays the total energy of the system must be conserved, however in the case of both *beta*-decays the energy of the final system is shared amongst the three final particles, the daughter nucleus (Y), the beta particle (e^- or e^+) and the electron-neutrino (ν_e or $\bar{\nu}_e$). Therefore, unlike the alpha decay, the energies of each particle are not quantised, instead having some statistical distribution where $0 < T_\beta < Q_\beta$. The total energy of the decay Q_β, is equal to the total energy difference of the initial and final particles:

$$\begin{aligned} Q_{\beta^-} &= M({}^A_Z X_N)c^2 - M({}^A_{Z+1} Y_{N-1})c^2 \\ Q_{\beta^+} &= M({}^A_Z X_N)c^2 - M({}^A_{Z-1} Y_{N+1})c^2 - 2m_e c^2 \\ Q_{EC} &= M({}^A_Z X_N)c^2 - M({}^A_{Z-1} Y_{N+1})c^2 - E_b(e^-) \end{aligned} \tag{3.9}$$

where M is the atomic mass of the mother and daughter nuclei and m_e is the electron rest mass. The electron capture process (ε or EC) is the competing process to β^+ decay in neutron-deficient nuclei. In this decay the wavefunction of a deeply bound electron overlaps with the mother nucleus resulting in the electron being captured by the nucleus and an emission of an electron neutrino. After the electron capture process a characteristic X-ray is emitted from the atom which results from the de-excitation of a valence electron to the vacancy left by the captured electron.

3.3 Electromagnetic Emission

In nuclear reactions or after radioactive decays, highly excited states can be populated with large angular momenta. These can be de-excited by two electromagnetic processes being,

γ-ray emission and internal conversion. Both processes provide an essential probe into nuclear structure.

3.3.1 γ-ray Emission

An excited nucleus with angular momentum I and parity π can transition from some initial state I_i^π to a lower energy state I_f^π by emission of a photon known as a γ-ray. As the mass of a nucleus is far greater than the energy of a γ-ray (few keV to MeV), the recoil energy of the nucleus can be considered to be negligible. The γ-ray energy (E_γ) is therefore said to be equal to the energy difference between the two nuclear states

$$E_\gamma = E_i - E_f, \tag{3.10}$$

where E_i is the energy of the initial state and E_f is the energy of the final state. Additionally, the total angular momentum of the γ-ray (L_γ) is restricted between two values,

$$|I_f - I_i| \leq L_\gamma \leq I_i + I_f. \tag{3.11}$$

There are two classes of γ decay, electric (E) and magnetic (M) each with a multipole order of 2^L. The parity selection rules of electric and magnetic γ decays are:

$$\pi(EL) = (-1)^{L_\gamma}, \pi(ML) = (-1)^{L_\gamma+1} \tag{3.12}$$

Where L is the angular momentum carried by the γ-ray from the nucleus. The γ-ray transition strength probability (λ) from an initial to final state is

$$\lambda(\sigma L_\gamma; I_i \to I_f) = \frac{8\pi(L_\gamma+1)}{\hbar L_\gamma[(2L_\gamma+1)!!]} \left(\frac{E_\gamma}{\hbar c}\right)^{2L_\gamma+1} B(\sigma L_\gamma; I_i \to I_f), \tag{3.13}$$

Here $B(\sigma L_\gamma; I_i \to I_f)$ is the *reduced transition probability* and contains information about the initial and final states of the transition. The reduced transition probability is classified for both electric and magnetic transitions by,

$$B(\sigma L_\gamma; I_i \to I_f) = (2I_i+1)^{-1} |\langle f||M[\sigma L_\gamma]||i\rangle|^2 \tag{3.14}$$

where σ is the electric or electric or magnetic multipole moment.

A theoretical estimate of the lifetime of γ-decaying states can be derived with the *Weisskopf* or *single particle estimates* [42], which assumes the de-excitation of a single nucleon is responsible for the transition. Whilst these estimates are crude, they can be used

L	$t_{1/2}^{el}$(s)	$t_{1/2}^{magn}$(s)
1	$6.76\times10^{-6}/E_\gamma^3A^{2/3}$	$2.20\times10^{-5}/E_\gamma^3$
2	$9.52\times10^{6}/E_\gamma^5A^{4/3}$	$3.10\times10^{7}/E_\gamma^5A^{2/3}$
3	$2.04\times10^{19}/E_\gamma^7A^{2}$	$6.66\times10^{19}/E_\gamma^7A^{4/3}$
4	$6.50\times10^{31}/E_\gamma^9A^{8/3}$	$2.12\times10^{32}/E_\gamma^9A^{2}$

Table 3.1 Half-lives ($t_{1/2}^{el,magn}$) based on the Weisskopf estimates of the first four orders of multipolarity (L) for both electric and magnetic transitions [6]. A is the nuclear mass number and E_γ is the γ-ray energy in keV.

to assess the single-particle nature or constrain the multipolarities of γ-ray transitions. The estimated half-lives ($t_{1/2}$, shown in Table3.1), the strength of a transition is expressed in terms of Weisskopf units (W.u),

$$\text{W.u} = t_{1/2}^{Weisskopf}/t_{1/2}^{experimental}. \tag{3.15}$$

Experimental transition strengths are typically $\sim 10^{-2}$ W.u for $E1$ multipolarity, and $\sim 10^{-1}$ W.u ~ 100 W.u for $M1$ and $E2$ transitions respectively. For this reason transition strengths can be used to determine the multipolarity of transitions when the initial and/or final angular momentum are not known. Transition strengths are also significantly reduced for isomeric transitions, which are not well described by a single-particle de-excitation.

3.3.2 Internal Conversion

Directly competing with γ-ray emission is the electromagnetic process of internal conversion. This is where an atomic nucleus can dexcite via the emission of an atomic electron from some shell Λ with energy,

$$T_e(\Lambda) = E_\gamma - E_b(\Lambda) \tag{3.16}$$

Where E_γ is the energy of the transition (and competing γ-ray), and $E_b(\Lambda)$ is the binding energy of the Λ shell electron, where $\Lambda = K, L$ and M. Therefore internal conversion can only occur for transitions where $E_\gamma \geq E_b(\Lambda)$

For any transition, assuming the nucleus is not fully stripped, the internal conversion has a non-zero probability, however this probability is related to the energy and multipolarity of the transition as well as the charge of the atomic nucleus. The highest probabilities of

internal conversion occur for low energy and high multipolarity transitions in high Z nuclei. The ratio of internal conversion to γ-ray emission is represented by the internal conversion coefficient and can be calculated for a specific electron shell,

$$\alpha_{\Lambda} = \frac{I_{ce}(\Lambda)}{I_{\gamma}} \tag{3.17}$$

where $I_{ce}(\Lambda)$ is the intensity of internal conversion and I_{γ} is the intensity of γ-rays. $I_{ce}(\Lambda)$ is measured by detection of either conversion electrons or characteristic x-rays following conversion. The total conversion coefficient for a transition is defined as the sum of conversion from all atomic electron shells,

$$\alpha_{tot} = \alpha(K) + \alpha(L) + \alpha(M) + ... \tag{3.18}$$

This value can be more easily calculated by measuring difference in the number of γ-ray transitions and decays which feed to the same initial state. Additionally this quantity can be used to aid in determining the multipolarity of a transition by comparing theoretical and experimental results.

Chapter 4

Experimental Setup and Analysis Techniques

4.1 Fusion Evaporation Reactions

Since nuclei of interest are often unstable, short lived, and not naturally abundant, they are usually produced artificially in the laboratory. The method used in this work, fusion-evaporation reactions, is currently the most efficient in-beam method to produce neutron-deficient nuclei. These reactions are performed by impinging a beam of accelerated ions onto a stable, or long-lived, target. If the kinetic energy of the projectiles is sufficient to overcome the Coulomb barrier, then it is possible for it to strike a target nucleus. In this scenario the two nuclei may merge via a fusion reaction into a highly excited compound nucleus. The beam energy needed to overcome the Coulomb barrier in the center-of-mass frame can be approximated by [43]:

$$E_C = \frac{1.44 Z_1 Z_2}{1.16(A_1^{1/3} + A_2^{1/3}) + 2} [\text{MeV}], \tag{4.1}$$

where Z_1, A_1, Z_2 and A_2 are the charge and mass numbers of the beam and target nuclei, respectively. Incident beam energies used are typically in the range of 3-8 MeV/nucleon, such that the energy is enough to overcome the Coulomb barrier whilst restricting the total angular momentum transferred to the nucleus. If the angular momentum transferred to the compound nucleus is too large then the rapid rotation could cause the repulsive centrifugal force to become larger than the short-range strong nuclear force leading to nuclear fission. The excitation energy (E^*) of the compound nucleus is defined as

$$E^* = E_{CM} + Q, \tag{4.2}$$

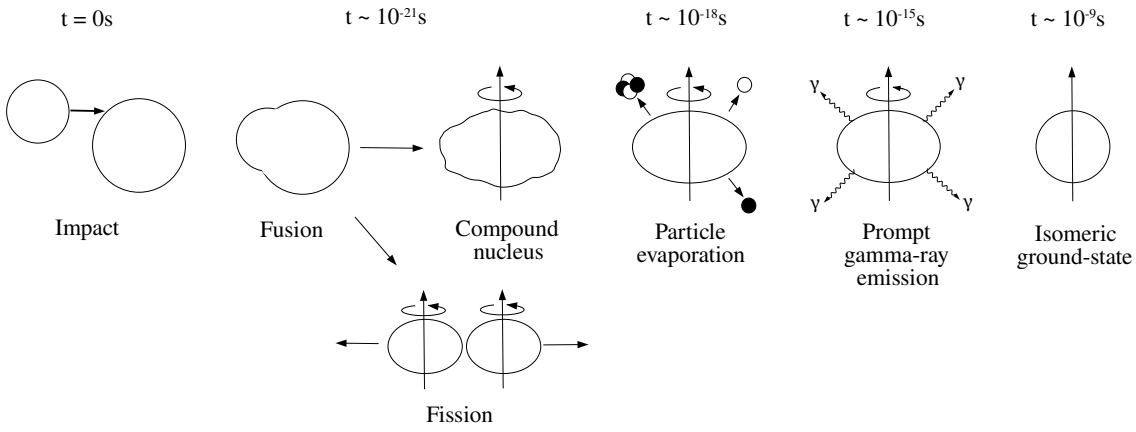

Fig. 4.1 A schematic illustration of the fusion-evaporation reaction over time. Approximate formation and emission times are indicated for each stage including the fission channel. The residue nucleus travels $\sim$1 cm/ns at $\beta = 4\%$. Figure is adapted from [44].

where E_{CM} is the centre of mass energy and Q is the difference in binding energy caused by the fusion reaction.

The high excitation energy of the compound nucleus results in a competition of nuclear fission and particle evaporation. Particle evaporation consist of the emission some combination of protons, neutrons, and alpha particles from the compound nucleus and is followed by a subsequent rapid de-excitation by γ-ray emission. Fig. 4.1 illustrates both the production and decay processes of the fusion evaporation reaction with the time frames involved. Due to the short timescales in which fusion and particle evaporation occurs, gamma-ray emission takes place whilst the recoiling nucleus is still inside the target. Experimentally a sufficiently thin target is used, allowing the compound nucleus to travel outside of the target material and towards a separator. Fig. 4.2 shows the fusion evaporation cross-sections for the reaction used in this work calculated using the HIVAP code [45].

The experiment outlined in this work was performed at the K-130 cyclotron [46] at the Accelerator Laboratory of the University of Jyväskylä (JYFL). The nucleus of interest, ^{178}Au, was produced by impinging a 381 MeV beam of ^{88}Sr on to a 600 $\mu g/cm^2$ thick isotopically enriched (98%) ^{92}Mo target. This reaction produces a fusion compound nucleus of ^{180}Hg and ^{178}Au via the pn evaporation channel [^{92}Mo(^{88}Sr, pn)]. An average beam current of 6 pnA was delivered over 6 days.

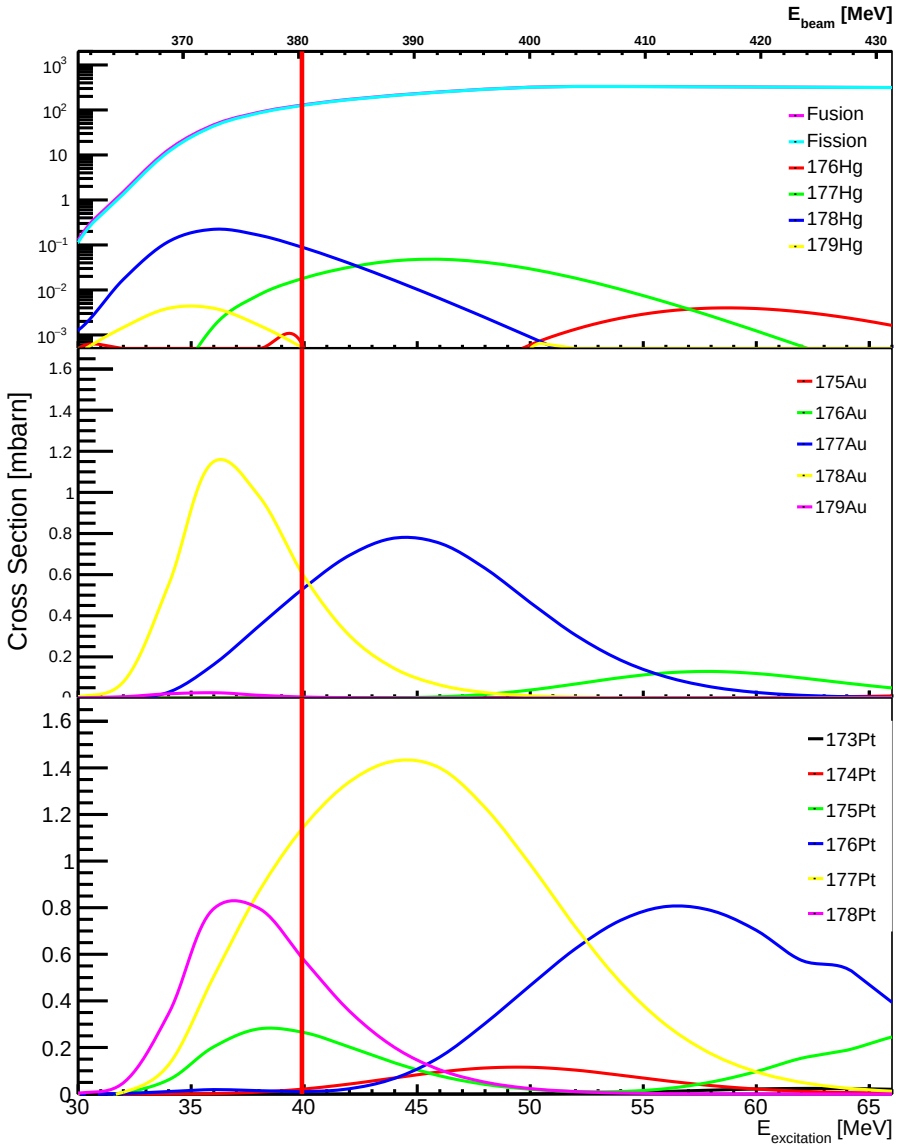

Fig. 4.2 Production cross-sections of the ^{88}Sr + ^{92}Mo $\rightarrow$ ^{180}Hg* fusion evaporation reaction calculated using the HIVAP code [45]. The centre of mass and final excitation energies are marked along with the fission cross section and all evaporation channels up to (2p,5n). The vertical red line denotes the 381MeV beam energy used in this work.

4.2 Experimental Setup

4.2.1 JUROGAM II, γ-ray Spectrometer Array

Detection of prompt γ-rays emitted in the fusion-evaporation reaction was performed using the JUROGAM II γ-ray spectrometer shown in Fig. 4.3. This detector array consists of twenty four EUROGAM clover detectors [47] and fifteen EUROGAM phase one [48] germanium detectors arranged in four rings positioned around the target chamber. Additionally each germanium detector in the array was surrounded by a bismuth germanate (BGO) shield, acting as detectors to veto Compton scattered γ rays and improve the peak to background ratio. Each clover detector is comprised of four individual crystals with position defined by two angles θ and ϕ outlined in Tab. A.1.

4.2.2 Recoil Ion Transport Unit (RITU)

After evaporation residues (ER's) and the unreacted beam leave the target position, the ER's were separated and transported to the focal plane by the Recoil Ion Transport Unit (RITU) [49] shown in Fig. 4.4. This gas-filled separator consists of three quadrupole magnets and a single dipole magnet in the configuration $Q_V \rightarrow D \rightarrow Q_H \rightarrow Q_V$. The first quadrupole is used to focus ER's to the dipole magnet D where they are separated from unreacted beam and fission products, based on the mass to charge ratio. Then the final two quadrupole magnets are used to vertically and horizontally focus the separated ER's onto the focal plane detectors.

The separator was filled with helium gas to a pressure of $\sim (0.5-1)$ mbar. This causes collisions between the ER's and helium atoms to occur in RITU resulting in the varying of charge states of the ER's due to electron captures and knockouts. Whilst a gas-filled separator sacrifices mass-resolving power when compared to a vacuum separator it has the advantage that the transmission efficiency is far greater. This is because the ER's follow a trajectory determined by their average charge state independent of the original charge state as they left the target. The relationship between the magnetic rigidity $B\rho$ and the average charge state q_{av} of an ion is given by

$$B\rho = \frac{mv}{eq_{av}} = \frac{mv}{(ev/v_0)Z^{1/3}}. \tag{4.3}$$

Where B is the magnetic field strength, ρ is the radius of the ion path, mv is the momentum of the recoiling nucleus and v_0 is the Bohr velocity = 2.19×10^6 m/s. The magnetic field is adjusted to best select the nucleus of interest, with RITU having a maximum magnetic rigidity of 2.2 Tm.

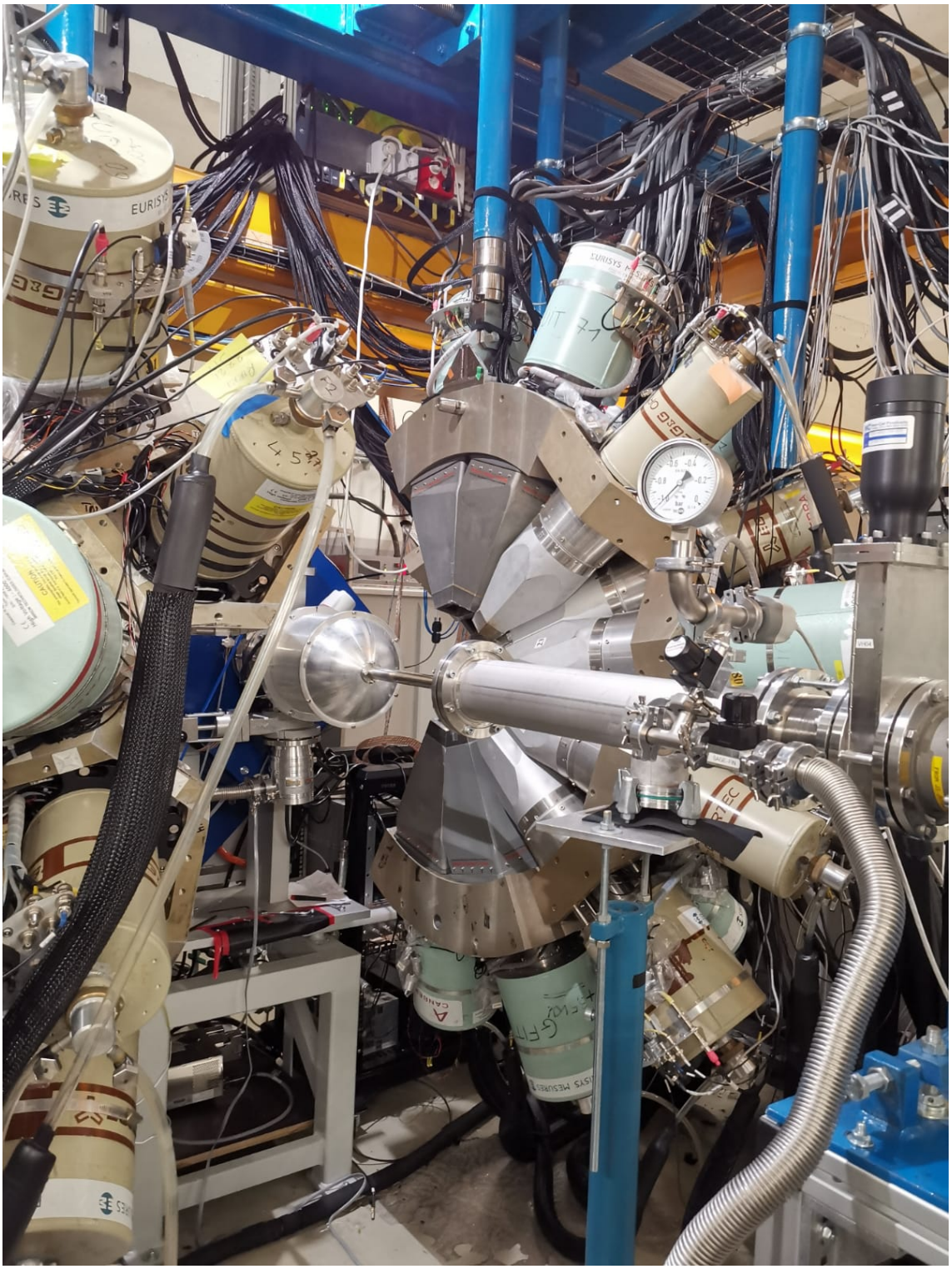

Fig. 4.3 Photograph of the JUROGAM γ-ray spectrometer in an open position, around the cylindrical target chamber shown.

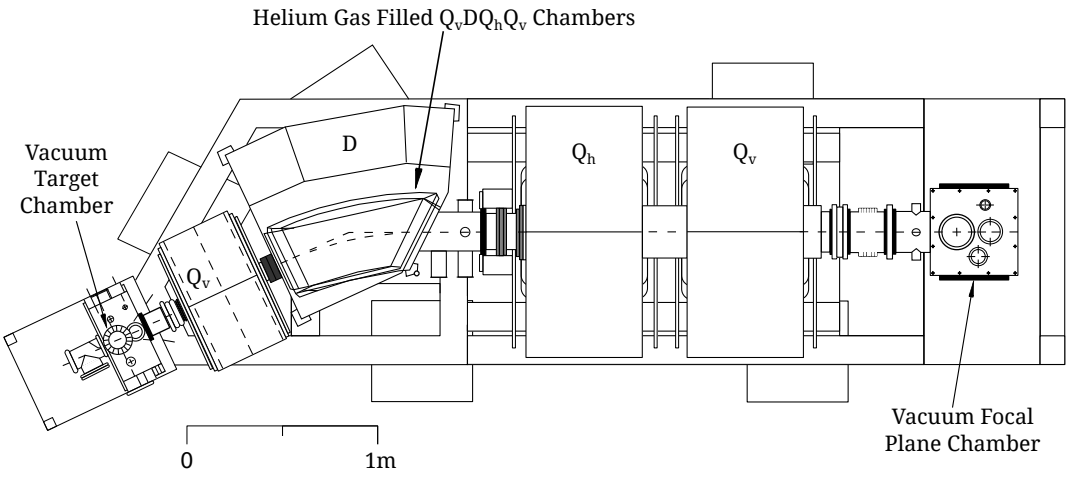

Fig. 4.4 Schematic of the RITU gas-filled separator with configuration of Quadrupole (Q) and dipole (D) magnets used. Figure taken from [43]

4.2.3 The GREAT focal-plane Spectrometer

The **G**amma **R**ecoil **E**lectron **A**lpha **T**agging (**GREAT**) spectrometer [50], was positioned downstream of RITU at its focal plane and used to detect recoils by means of implantation, and measure subsequent decays. The spectrometer consisted of several elements that together measured ER's, subsequent isomeric decays as well as α and β-decays. A schematic drawing of the each detection element can be seen in Fig.4.5, and is described in the following sections.

Multiwire proportional counter

A transmission multiwire proportional counter (MWPC) is positioned at the entrance of GREAT to detect ER's transported by RITU. The MWPC comprises of four cathode wires planes combined with an anode wire plane and is contained within two Mylar windows. The entrance window has dimensions 131 mm $\times$ 50 mm and separates the isobutane gas in the MWPC from the He gas in RITU. After the 1 mm thickness of the MWPC, an exit window with equal dimensions to the entrance separates the isobutane from the GREAT vacuum.

The MWPC provides energy loss and timing signals with its function to aid in distinguishing between recoiling reaction products and radioactive decays which are seen in the implantation detector (next section) but not in the MWPC.

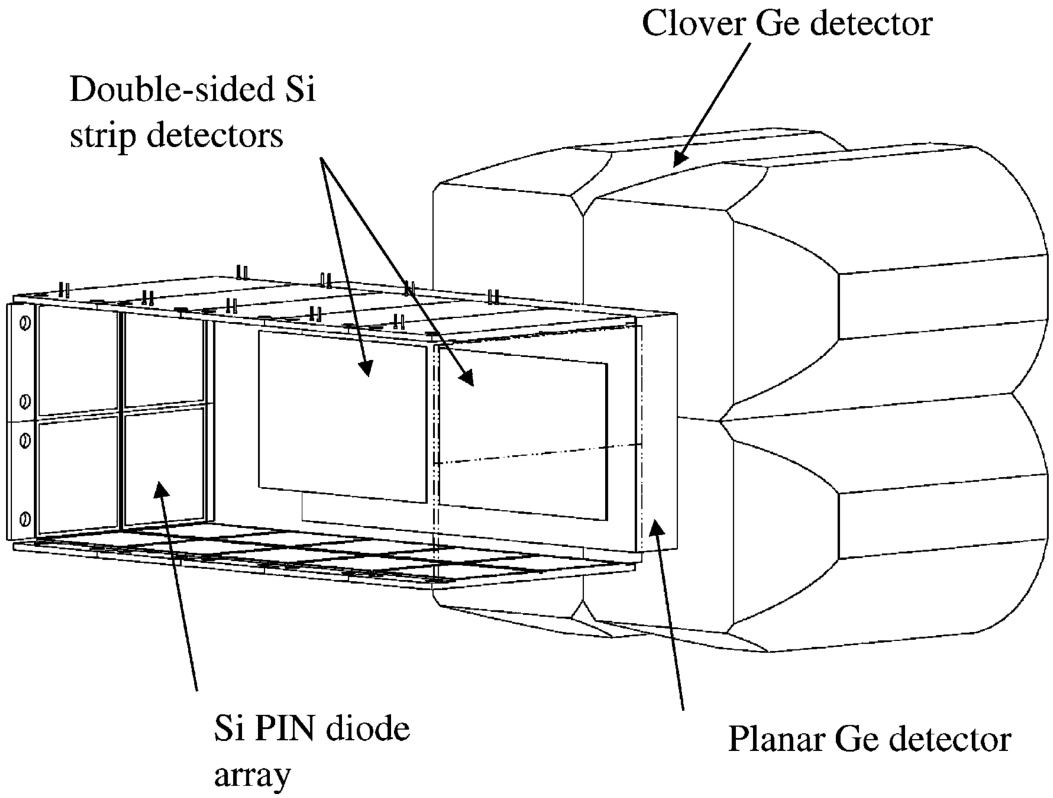

Fig. 4.5 Schematic drawing of the GREAT spectrometer [50]

Implantation detector

Transmitted recoils are implanted into one of two Double-sided Si strip Detectors (DSSD) mounted side by side at the focal plane. Each DSSD has an active area of 50 mm $\times$ 40 mm and thickness of 300 μm. They consist of 60 $\times$ 1 mm vertical strips on the front side and 40 $\times$ 1 mm horizontal strips on the rear side giving each detector an effective 2400 pixels of area 1 mm $\times$ 1 mm each. As well as using the DSSD's to measure implanted ER's they can be used to perform α-decay spectroscopy. Often this involves using the condition that a ER is implanted in the same pixel as its subsequent α-decay with this method used in recoil-decay-tagging and discussed later. The small pixel size of the DSSD's allows for much higher rates to be used in recoil-decay-tagging than non-segmented detectors.

PIN-diode array

Upstream of the DSSD's a box of 28 PIN diodes, each with an active volume of 28 mm $\times$ 28 mm $\times$ 500 μm (thickness) was mounted. The PIN diode array was designed to detect

conversion electrons and α-decays that escape the DSSD due to low implantation depth. This detector element was not used in any analysis presented in this work and as such will not be discussed.

Planar Ge detector

Downstream of the DSSD's, a planar double-sided Germanium strip Detector (PGD) was mounted to detect low-energy γ rays from isomeric transitions as well as X-rays and high-energy β particles. The rectangular crystal has an active area of 120 mm $\times$ 60 mm and a thickness of 15 mm. Each strip has an active width of 5 mm, giving 24 $\times$ 12 for a total of 288 effective pixels. Due to the small thickness of the PGD it cannot efficiently measure high-energy γ rays, therefore in some experiments using the GREAT spectrometer, additional clover Ge detectors are placed surrounding the focal plane.

4.3 Calibrations

4.3.1 Energy calibrations

All germanium detectors were calibrated using sealed ^{152}Eu and ^{133}Ba sources. The DSSD detector in the GREAT spectrometer was calibrated using a mixed triple α source of ^{239}Pu, ^{241}Am and ^{244}Cm. However, the DSSD has a dead-layer which reduces the energy deposited from an external α source, but does not impact the energy deposition of α particles emitted from implanted ions. Therefore the known α-decay energies from implanted ^{176,177,174}Pt and ^{178}Hg nuclei were subsequently used to calibrate the DSSD. As the output signal voltage of a detector is proportional to the deposited energy, a quadratic function was fitted to convert between ADC channels and the deposited energy for each detector.

4.3.2 Efficiency calibration

An efficiency curve for JUROGAM II was produced with measurements from the same radioactive sources as the energy calibration. As the efficiency curve was only necessary for the relative intensities of γ-ray transitions and angular correlations (see 4.6.3), only the relative efficiencies were considered for each ring of JUROGAM II.

The curve fitted to the efficiency data of JUROGAM-II has the form [43],

$$log(\varepsilon) = [(A+Bx)^{-G} + (D+Ey+Fy^2)^{-G}]^{-1/G}, \tag{4.4}$$

where ε is the efficiency, $x = log(E_\gamma/100)$, $y = log(E_\gamma/1000)$ and E_γ is the energy of the detected γ ray in keV. An efficiency calibration was then calculated for each ring of JUROGAM II with the resulting parameters listed in Table 4.1.

Ring	A	B	D	E	F	G
Total	6.20	1.79	5.49	-0.64	-0.032	20
1	3.27	2.20	3.27	-0.55	-0.002	9
2	4.78	2.30	3.96	-0.61	0.034	8
3	5.47	1.95	4.75	-0.56	0.039	9
4	5.06	1.87	4.69	-0.56	-0.019	15

Table 4.1 Values of the parameters used for the curves fitted to the JUROGAM-II detector using Equation. 4.4

.

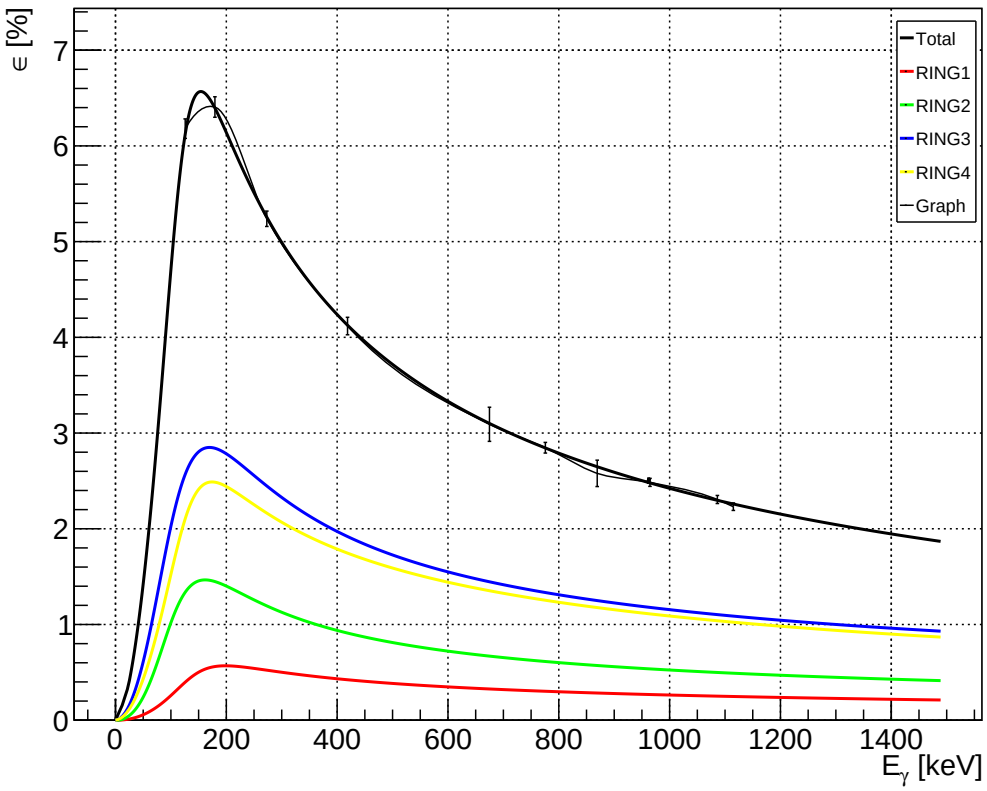

Fig. 4.6 Relative efficiency curve of each ring in the JUROGAM II Ge array used for this work. Curves were fitted using the equation 4.4, and parameters are listed in Table. 4.1.

Efficiency curves for the detectors in the GREAT spectrometer were produced by Andreyev et al via GEANT3 simulations [51].

4.4 Doppler Correction

The JUROGAM II array was calibrated with a static sealed source at the target position, however ER's travel through the target position as they emit γ rays. Therefore the detected energies of the γ rays are Doppler shifted depending on their emission angle relative to the velocity of the ER. This shifted energy E', is related to the energy in the nucleus frame and the angle θ between the emitted γ ray and the beam,

$$E'_\gamma = E_\gamma(1+\beta cos\theta), \tag{4.5}$$

where $v =$ recoil speed, $c =$ speed of light, $\beta = \frac{v}{c}$ and θ is the angle between the γ ray and the direction of the recoil velocity. Experimentally β was calculated by plotting $cos\theta$ against $(E'_\gamma - E_\gamma)/E_\gamma$ for the known yrast band of ^{178}Pt. The gradient of this plot gave $\beta = 0.0425$[3]. Each clover detector was then Doppler corrected depending on its angular position outlined in Table. A.1. This correction is not necessary for the Planar Ge detector in GREAT due to ER's being completely stopped in the DSSD's.

4.5 Total data readout

In a standard data acquisition systems (DAQ's), an event is created following a hardware trigger. This results in detector systems being collected in some time gate and produces some dead-time in the process. This method works well when the triggering rate is low, however for higher rates or for a high background to signal ratio this can lead to large dead-time causing the DAQ to miss useful events.

The **T**otal **D**ata **R**eadout (**TDR**) [52] overcomes such a limitation by reading all the data with no triggering condition. Each hit is then timestamped (10ns precision) and collected, eliminating common dead-time. Events are then constructed by correlating hits using a software trigger. As such the TDR does not rely on a fixed hardware trigger. This is useful as it allows for observations of events before a trigger and correlations with extremely long gates; useful for tagging on long half-life decays. As storing all data over an experiment would result in impractically large file sizes with largely the largely fission events, a pre-filter is used to determine which data to write to disk. In the case of this work all correlations rely on recoil tagging with the pre-filter only storing data which could be correlated with a hit in the DSSD. Therefore all data analysed in this work had a correlation with the DSSD either by means of a recoil implantation or a decay.

4.6 Analysis techniques

4.6.1 γ-ray correlations

Detection of γ-rays emitted from an atomic nucleus can provide a tool to retrieve information about it's structure. In order to first construct level-schemes of excited states in nuclei successive γ-ray transitions must first be correlated experimentally. The 10-ns timing resolution of the digital DAQ used along with the slow response time of semiconductor detectors compared to the half-life of prompt γ-ray transitions means that successive γ-ray transitions are unable to be timestamped sufficiently accurately as to order their occurrence. For this reason, neither lifetime determination methods nor comprehensive ordering for prompt transitions can be established, however by simple γ-ray coincidences a level-scheme can be still constructed such that it reflects the changing structure of the nucleus during de-excitation.

In the work presented, transitions detected in the JUROGAM II array were considered coincident if they occur within 10 timestamps of each other (corresponding to 100ns). This time-window accounts for variance in the timestamp caused by both the charge collection in JGII and subsequent signal processing. Correlation of γ-rays in this way gives events containing the detection of several transitions within the time window usually from the same individual nucleus. In γ-ray coincidences, we describe the value of the "multiplicity" (or fold), being equal to the number of transitions detected per event. Events with high-multiplicity (high-fold) are desirable as they can give strict constraints which can be used to identify the de-excitation path of the nucleus.

As well as uncorrelated γ-rays (singles), multiplicity two events can be used to construct γ-γ correlations. These γ-rays are stored into a symmetrical matrix for analysis and additional multiplicity > 2 events are unfolded into pairs to increase statistics further. From γ-γ matrices, coincident transitions can be identified by projecting the matrix gated on a γ-ray of interest. These projections are used to attempt to find a discrete decay path and produce a decay scheme for the nucleus. The efficiency of γ-γ detection is significantly lower than uncorrelated as it a product of the detection efficiencies of each individual γ-ray.

To further constrain the possible decay paths of the nucleus, triple γ-ray coincidences can be used. This utilises events with multiplicity ≥ 3, constructed into a symmetrical cube with each axis representing an individual γ-ray energy and each entry representing a triple coincidence. Coincidences are then analysed by selecting two γ-ray transitions and

simultaneously projecting with an AND gate resulting with the third coincident γ-ray.

4.6.2 Recoil tagging

As discussed in section 4.1, the fusion evaporation reaction used is dominated by fission inside the target. These fission events will each result in two highly excited, γ-ray emitting nuclei and will comprise the majority γ-rays detected in JUROGAM II. To avoid fission events and isolate excited states from ER's recoil tagging is utilised.

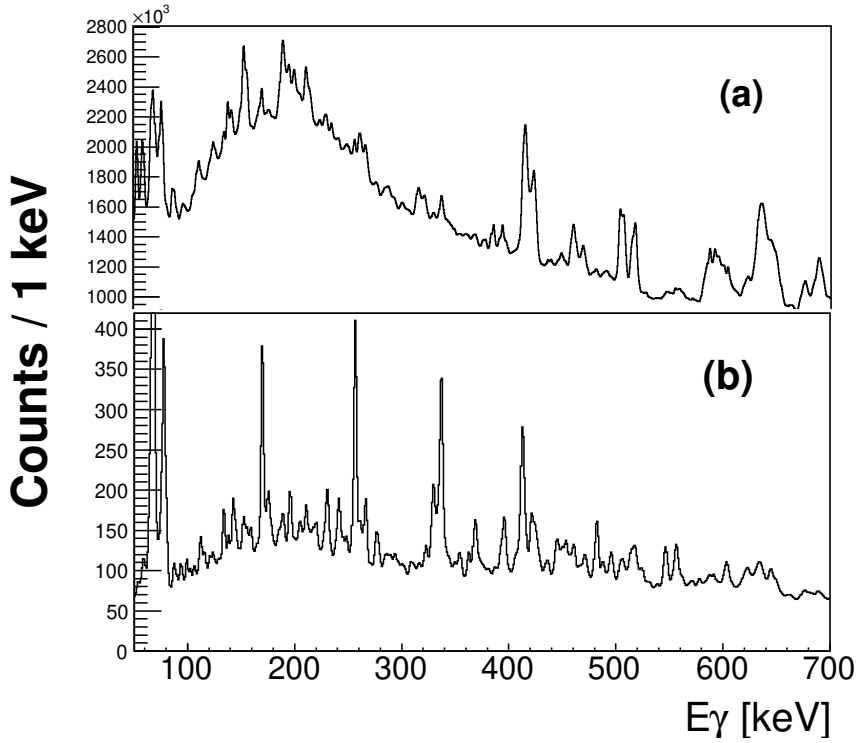

Fig. 4.7 (a) JGII γ-ray singles spectrum (JGII$_\gamma$), (b) recoil-gated JGII γ-ray singles spectrum (ER-JGII$_\gamma$) in which the yrast band of the strongly-produced ^{178}Pt is seen.

Recoils are identified by their separation in RITU, and implantation into the DSSD at GREAT, with two conditions placed to correctly identify ER's over other background. Firstly, coincidence must exist between the DSSD and MWPC upstream. This helps to ensure a decay of implanted nucleus is not misidentified. Secondly the energy measured in the DSSD must be sufficiently high that only an implanting nuclei could provide sufficient energy losses. The effectiveness of this technique can be seen in Fig. 4.7 where without recoil-tagging,

γ-rays from fission products are dominant. Using recoil-tagging the yrast band of the fusion-evaporation product ^{178}Pt becomes dominant and the contribution from fission products is removed. As ^{178}Pt had one the largest cross-sections in the fusion evaporation reaction, its yrast band was often seen in subsequent recoil-gated JGII analysis.

4.6.3 Angular correlations

Angular correlations were performed by the method of the directional correlations of de-exciting oriented states (DCO) [53] using the same method described in [54]. Two $\gamma\gamma$ matrices are produced by sorting recoil-gated prompt coincidences from JUROGAM II crystals located at (all angles) vs (157.6°) and (all angles) vs (75.5°). By producing projections gated on the same energy gate on (all angles) in both matrices, the intensities of coincidence γ rays are extracted and normalised by the detection efficiency. The DCO ratio is then calculated with the formula,

$$R_{\mathrm{DCO}} = \frac{I_\gamma(157.6^\circ)}{I_\gamma(75.5^\circ)} \tag{4.6}$$

where $I_\gamma(157.6)$ and $I_\gamma(75.5)$ are the intensities of coincident transitions produced. This results in typical values of $R_{\mathrm{DCO}} \sim 0.8$ for stretched dipole transitions and ~ 1.3 for stretched quadrupole transitions. R_{DCO} was first measured on the yrast band of ^{178}Pt to ensure the values were reliable for γ ray transitions up to 700 keV.

4.6.4 Recoil-decay-tagging technique

The **R**ecoil **D**ecay **T**agging technique (**RDT**) [55], is a method in which prompt γ-rays are correlated to the observation of a recoil together with a subsequent decay. In this case RDT typically utilises the α-decay tagging, in which an implantation in the DSSD is correlated with a subsequent α decay in the same pixel as the previous implantation of the recoil. As well as allowing for the specific recoils to be selected for γ ray spectroscopy it also permits a half-life measurement of the α decay by analysing the time difference between the α and recoil implantation. An ideal illustration of a recoil decay correlation can be seen in Fig. 4.8, where t-subscript denotes the timestamp of the event in the DSSD. ER_1 is a recoil implantation and α_1 is the decay of this implantation.

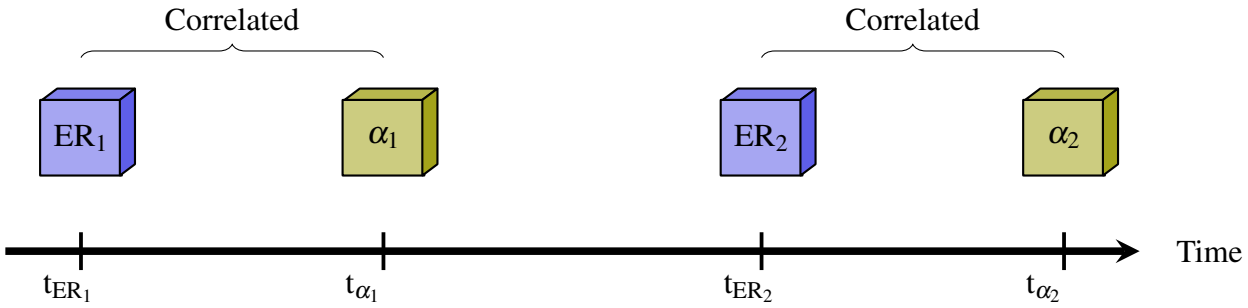

Fig. 4.8 Illustration for correlation definition in the recoil-decay tagging technique. ER and α are the evaporation residue and subsequent α decay. In this scenario each α-decay is correctly assigned to its ER.

In this case α decays are correctly correlated to recoils, however in the case of some combination of high implantation rate or long α-decay time (illustrated in Fig. 4.9) it is possible that multiple recoils could implant in the same pixel before the α decay occurs and is correlated.

In this scenario, the second recoil is incorrectly correlated with α_1 resulting in several consequences for the RDT technique. Firstly the measured decay time is reduced from its true value $t_{\alpha 1} - t_{ER_1}$, to $t_{\alpha 1} - t_{ER_2}$, where $0 \leq t_{ER_1} \leq t_{ER_2} \leq t_{\alpha 1}$. Additionally the alpha decay will be correlated to the interrupting recoil implantation, resulting in an incorrect recoil identification and preventing correct γ-ray correlation.

4.6.5 Isomer-decay-tagging technique

RDT produces many challenges for the case of ^{178}Au, primarily caused by the long half-life, low branching ratio and not helped by the high implantation rates used in this work. These

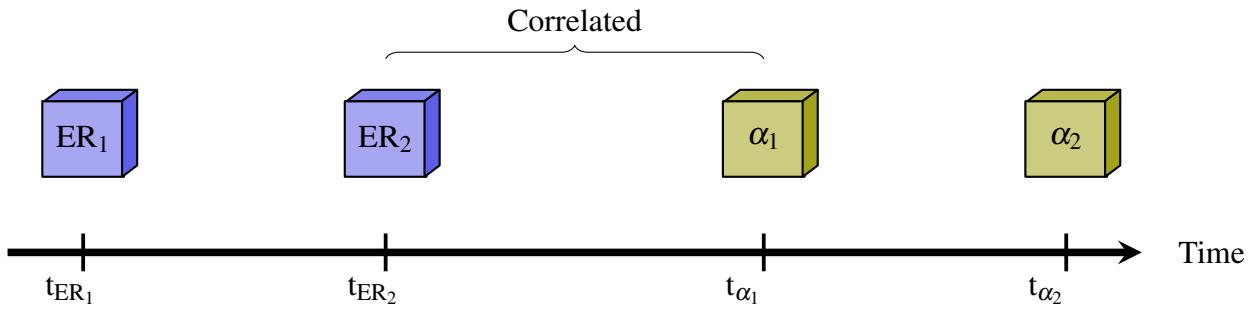

Fig. 4.9 Illustration for recoil-decay tagging with incorrect correlation when interrupted by a second recoil. In this scenario the α-decay is miss-correlated to a different ER.

issues can be bypassed by utilising the isomer-decay-tagging technique (IDT) [56].

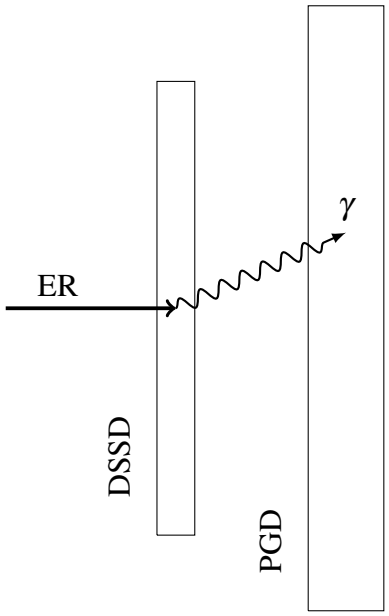

Fig. 4.10 Illustration of the isomer decay tagging technique in the GREAT spectrometer. ER and γ are the evaporation residue and subsequent isomeric decay respectively.

This technique works in a similar way to RDT, however instead the detection of an isomeric transition from the nucleus of interest is used as a tag. This method was applied in this work by utilising the DSSD and PGD and illustrated in Fig. 4.10. Recoil-tagging is performed with the additional requirement that the γ-ray from an isomeric transition is detected in the PGD and correlated with the recoil implantation. Due to the short, sub-μs, half-lives of the isomeric states of ^{178}Au, this method was far less impacted by the high implantation rates. Additionally the method also allows for structures above specific isomeric states to be individually studied. The main drawback of this technique is that it can be

far less efficient than RDT, with this due to the low efficiency of the PGD as well as the detection efficiency and the potentially high-conversion of low energy isomeric γ-rays. IDT was utilised to identify prompt γ-ray transitions above isomeric states of ^{178}Au as is discussed in the next chapter.

Chapter 5

Excited states of ^{178}Au

In this chapter analysis of excited states in the odd-odd nucleus ^{178}Au (Z=79, N=99) is presented along with derived decay schemes. The structure of this chapter is as follows: the discussion of the production of ^{178}Au and other nuclei by a fusion evaporation reaction in Sec. 5.1 is followed by analysis of sub-microsecond isomeric states above the α-decaying states ^{178}Au^{g,m} in Sec. 5.2. Finally knowledge of isomeric states allowed for isomer decay tagged and recoil gated prompt γ-ray spectroscopy to be utilised establishing a decay scheme for excited states of ^{178}Au in Sec. 5.3.

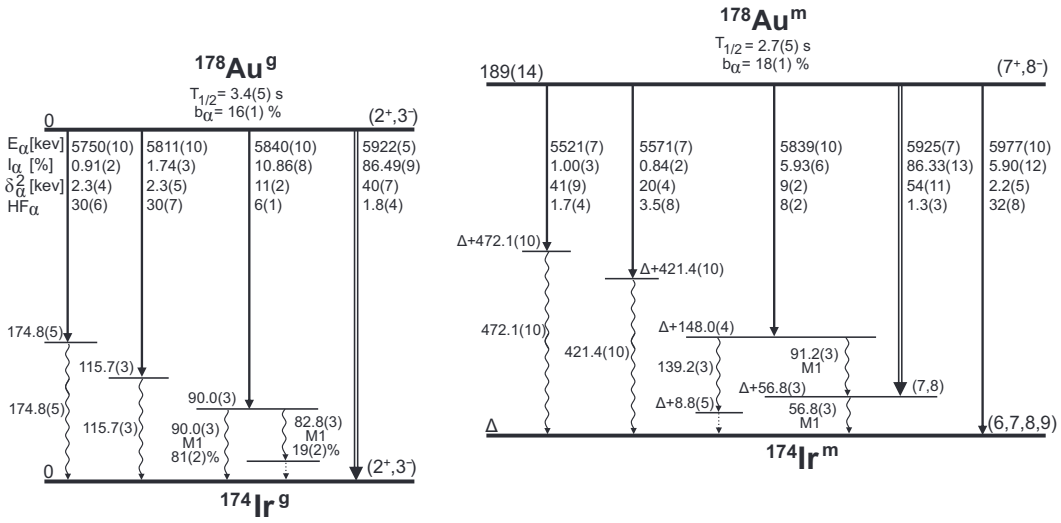

Fig. 5.1 Decay schemes for ^{178}Au^{g,m} produced in [16].

A significant part of this work is based on previous knowledge of two alpha-decaying isomers of ^{178}Au identified in a previous ISOLDE-CERN study by Cubiss *et. al.* [16]. This utilised the Isotope Separation On-Line (ISOL) method with an in-source resonant

laser ionisation technique to produce isomerically pure beams. Two α-decaying states were identified in the ISOLDE study, a low-spin $(2^+, 3^-)$ ground-state (^{178}Au^{g}) and a high-spin $(7^+, 8^-)$ isomeric state (^{178}Au^{m}). The α-decay scheme shown in Fig. 5.1 was crucial to the placement of sub-microsecond isomers presented later in this chapter.

5.1 Production of ^{178}Au

The experiment discussed in this work was performed on 5th-15th June 2015 at the Accelerator Laboratory of the University of Jyväskylä. The K-130 cyclotron delivered a 381 MeV beam of ^{88}Sr ions with an average current of 6 pnA over 6 days. This beam was impinged on a 600 μg/cm^2 thick, isotopically enriched (98%) ^{92}Mo target positioned at the centre of the JUROGAM II spectrometer, resulting in the fusion reaction ^{88}Sr + ^{92}Mo $\rightarrow$ ^{180}Hg* where ^{178}Au was produced in the p,n evaporation channel.

Firstly the recoils (or ER's), separated by RITU were implanted into the DSSD's allowing for identification by means of α-decay-spectroscopy. Figure 5.2(a) shows a part of the α-decay energy spectrum measured by the DSSD within 7 s of a recoil implantation. A 7 s correlation time was chosen to include approximately 3 half-lives of ^{178}Au. The DSSDs were calibrated using the known energy peaks from ^{174}Pt-6039(3) keV, ^{177}Pt-5517(4) keV, ^{176}Pt-5446(3) keV, and ^{178}Hg-6430(6) keV [10]. It can be seen that the recoils include $_{80}$Hg, $_{79}$Au, and $_{78}$Pt isotopes close to A=180, as is expected from the fusion evaporation reaction used (See Fig .4.2). ^{178}Au is predicted to have a cross section of ≈ 0.5 mbarn, comparable with ^{177}Au and ^{177,178}Pt . The relative production of ^{178}Au is significantly higher than is seen in the α-decay spectrum due to the low α-decay branching ratio of both states $b_\alpha(^{178}\text{Au}^{g}) = 16(1)\%$ and $b_\alpha(^{178}\text{Au}^{m}) = 18(1)\%$ [16]. The α-decay energies of ^{178}Au shown in Fig. 5.2, differ slightly from the literate values given in [16] with this due to a small difference in the calibrations used at ISOLDE and GREAT. For this reason the values deduced at ISOLDE were used in all constructed level-schemes shown in this thesis.

5.2 Identification of sub-microsecond isomers

This section discusses sub-microsecond isomers in ^{178}Au published by S. A. Gillespie, A. Stott *et. al.* [1], where a substantial amount of the analysis was contributed and discussed by the author of this thesis. If the half-life of an isomer is sufficiently long compared to the

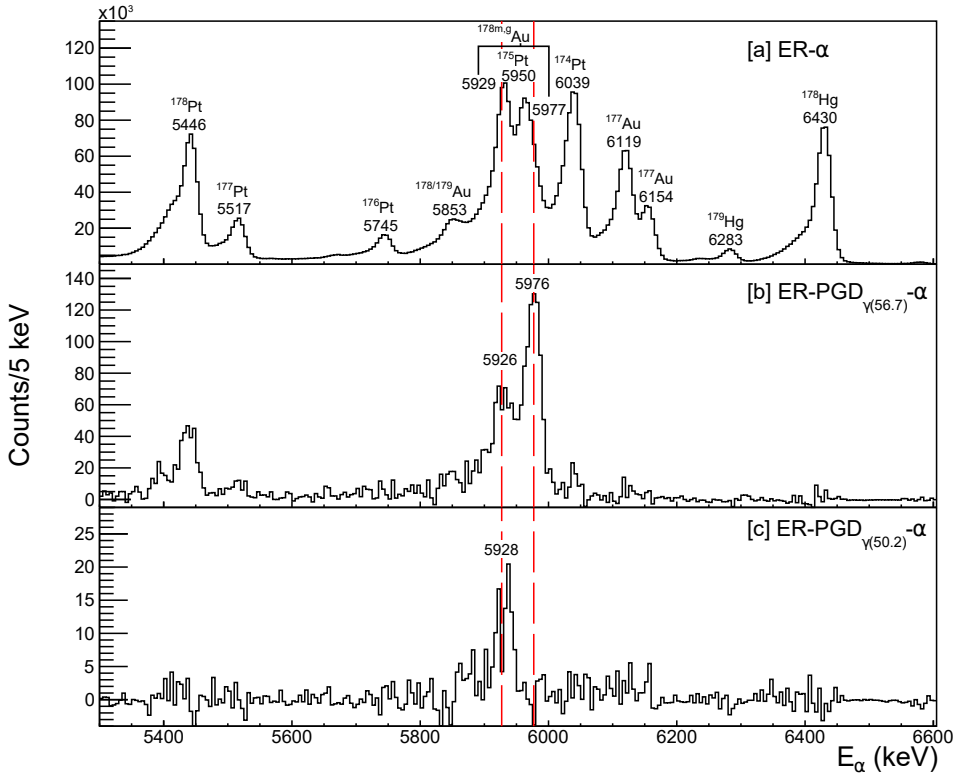

Fig. 5.2 (a) Energy spectrum observed in the DSSD's within 7 s of an ER's impantation. (b) Same as (a) except a gate on the 56.7 $\pm$1 keV γ ray detection in the PGD within ΔT(PGD-ER) = (0 – 1) μs of the recoil is applied. (c) Same as (b), but with PGD energy gate 50.2 $\pm$1 keV. Taken from [1].

time-of-flight of an ER through RITU (ToF $\approx$ 400-ns) onto the focal plane, then an isomeric transition can be observed in the PGD. Figure 5.3 shows the γ-ray spectra detected in the PGD after a recoil implantation in the DSSD. The observed isomeric transitions are labelled with their energies and isotopic origin. For ^{178}Au, the 50.2(2)- and 56.7(2)-keV transitions were first identified by Al-Monthery [27] with an additional 3 transitions at 60.0(2), 63.4(2) and 113.4(4)-keV identified by Gillespie *et. al* [1].

The isomeric transitions of ^{178}Au were assigned to either the ground state or high-spin isomer based on correlations with the known α decays of ^{178}Au^{g,m} (previously established in [16]). This is shown in Figs 5.2(b) and (c) with the DSSD recoil-gated energy spectrum with gates on the 56.7-keV and 50.2-keV isomeric transitions respectively observed in the PGD [ER-PGD(γ)-DSSD(α) analysis]. As shown in Fig 5.2(b), isomer-decay-tagging (IDT) produces clean α-decay spectra for both ^{178}Au and it's β-decaying daughter ^{178}Pt, removing all other channels.

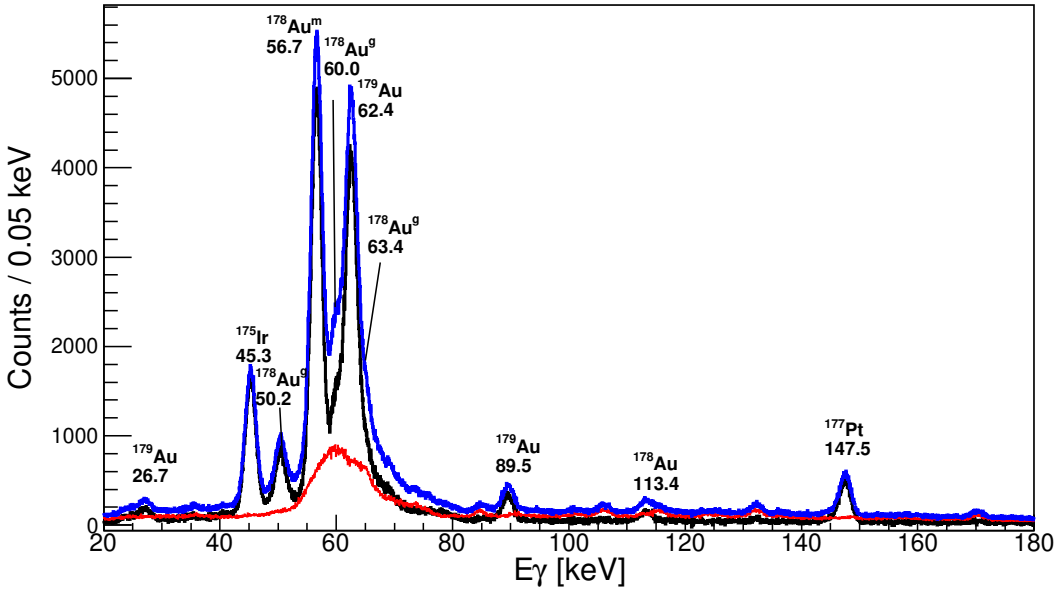

Fig. 5.3 In blue: Energy spectra in PGD observed within $\Delta T\,(\text{PGD-ER}) = (0-0.5)$ μs. In red: time-random background measured in the PGD within $\Delta T\,(\text{PGD-ER}) = (-0.5-0)$ μs. In black is the background subtracted spectrum. Peaks are labelled with energies in keV and isotopic origin. Isomeric transitions in ^{178}Au were identified in this work and in [27]. Known isomeric γ rays from other nuclei originated from ^{175}Ir [57], ^{179}Au [21] and ^{177}Pt [58].

It is seen that the 56.7-keV transition correlates with the two most intense α decays from the ^{178}Au$^{\text{m}}$ state (5925- and 5977-keV). Meanwhile the gate on the 50.2-keV isomeric transition shows correlation with only the 5925-keV α decay of the high-spin state. This places the 56.7-keV transition above the high-spin state (^{178}Au$^{\text{m}}$) and the 50.2-keV transition above the ground state ^{178}Au$^{\text{g}}$.

5.2.1 294-ns isomer

Whilst the 50.2-keV γ ray is correlated with the α-decaying state ^{178}Au$^{\text{g}}$, the 63.4-, 60.0-, and 113.4-keV transitions could not be intially placed above the ground state by the same method. This was due to high contamination preventing a clean gate for the 63.4-keV and 60.0-keV transitions, and a low intensity of the 113.4-keV transition. This contamination came from the strong 62.4-keV 327(2)-ns isomeric transition in ^{179}Au [21], overlapping with the PGD energy gates used.

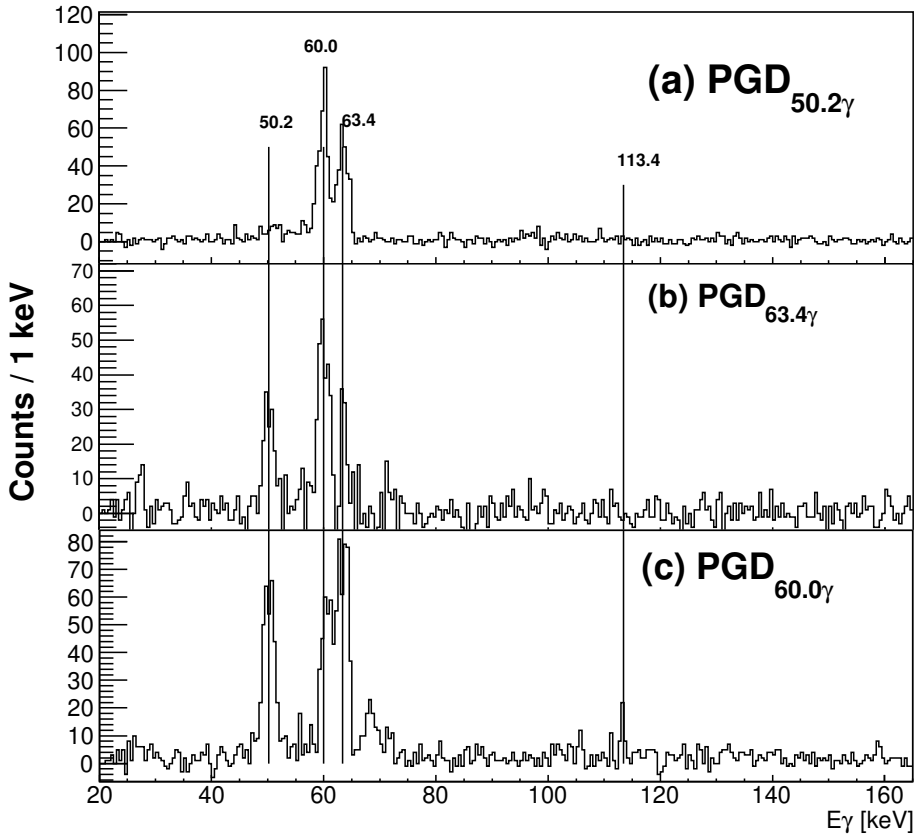

Fig. 5.4 Planar $\gamma\gamma$ projections gated on the (a) 50.2-keV, (b) the 63.4-keV and, (c) 60.0-keV isomeric transitions below the 294-ns isomer. $\Delta T(\gamma\gamma) \leq 70$ ns, energy gates $\pm$1-keV, background subtraction applied.

Therefore $\gamma\gamma$ coincidences in the planar detector were instead analysed, (see Fig. 5.4) with gates on the 60.0-keV and 63.4-keV transitions establishing a cascade of the 50.2-keV, 60.0-keV, and 63.4-keV γ rays. Additionally the 60.0-keV transition was seen to be coincident with the 113.4-keV transition, running parallel to the 50.2-keV and 63.4-keV transitions [50.2(2) + 63.4(2) = 113.4(4)]. This results in a total of four possible orderings of gamma rays above ^{178}Au^{g}, shown in Fig. 5.5. The multipolarities of the transitions will be deduced in Sec. 5.2.1 and discussed in Sec. 6.2.

The half-life of each isomeric transition was also measured to ensure additional consistency. This was completed by plotting the time difference ΔT(PGD-ER) between a recoil implantation and the subsequent isomeric transition detected in the PGD. This is then fitted to an exponential plus a constant background, with the form

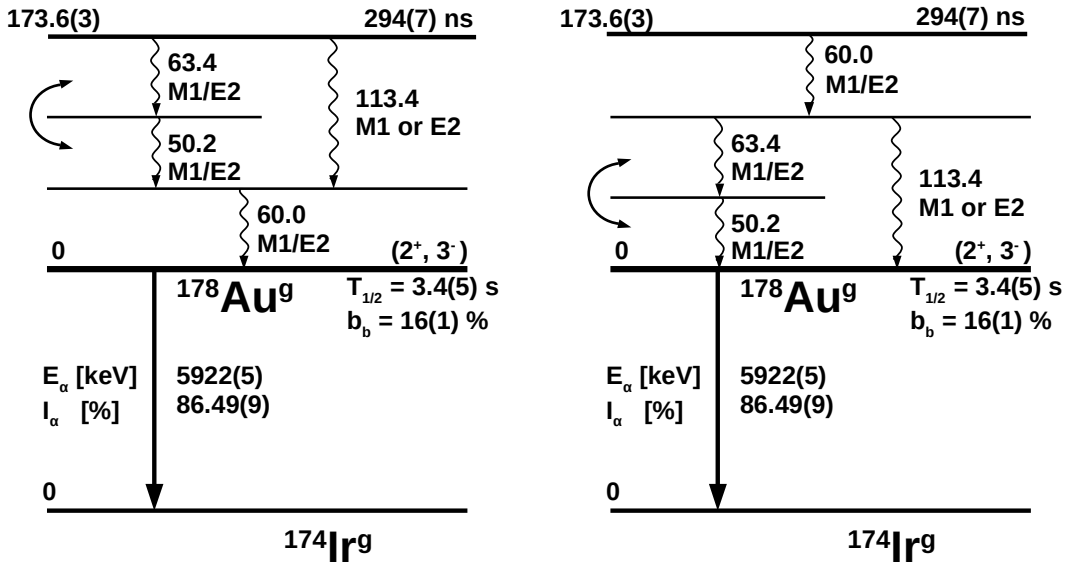

Fig. 5.5 Possible decay schemes for the 294-ns isomeric state above ^{178}Au^{g} identified in this work and in [27, 1]. α-decay half-lives, branching ratios and relative intensities are from [16]. Curved arrows denote that the 50.2-keV and 63.4-keV transitions can be swapped based on the current analysis with the final placement of transitions shown in Fig. 6.6.

$$N(t) = A_0 e^{\frac{-t\ln(2)}{t_{1/2}}} + C \tag{5.1}$$

to give a half-life $t_{1/2}$. The half-life measurements of the 50.2-keV, 60.0-keV, 63.4-keV and 113.4-keV transitions are shown in Fig. 5.6 giving an averaged $t_{1/2} = 294(7)$ ns assigned to the isomeric state. It should be noted that only some of these transitions are isomeric, which decays directly from the isomer whilst following decays will be prompt.

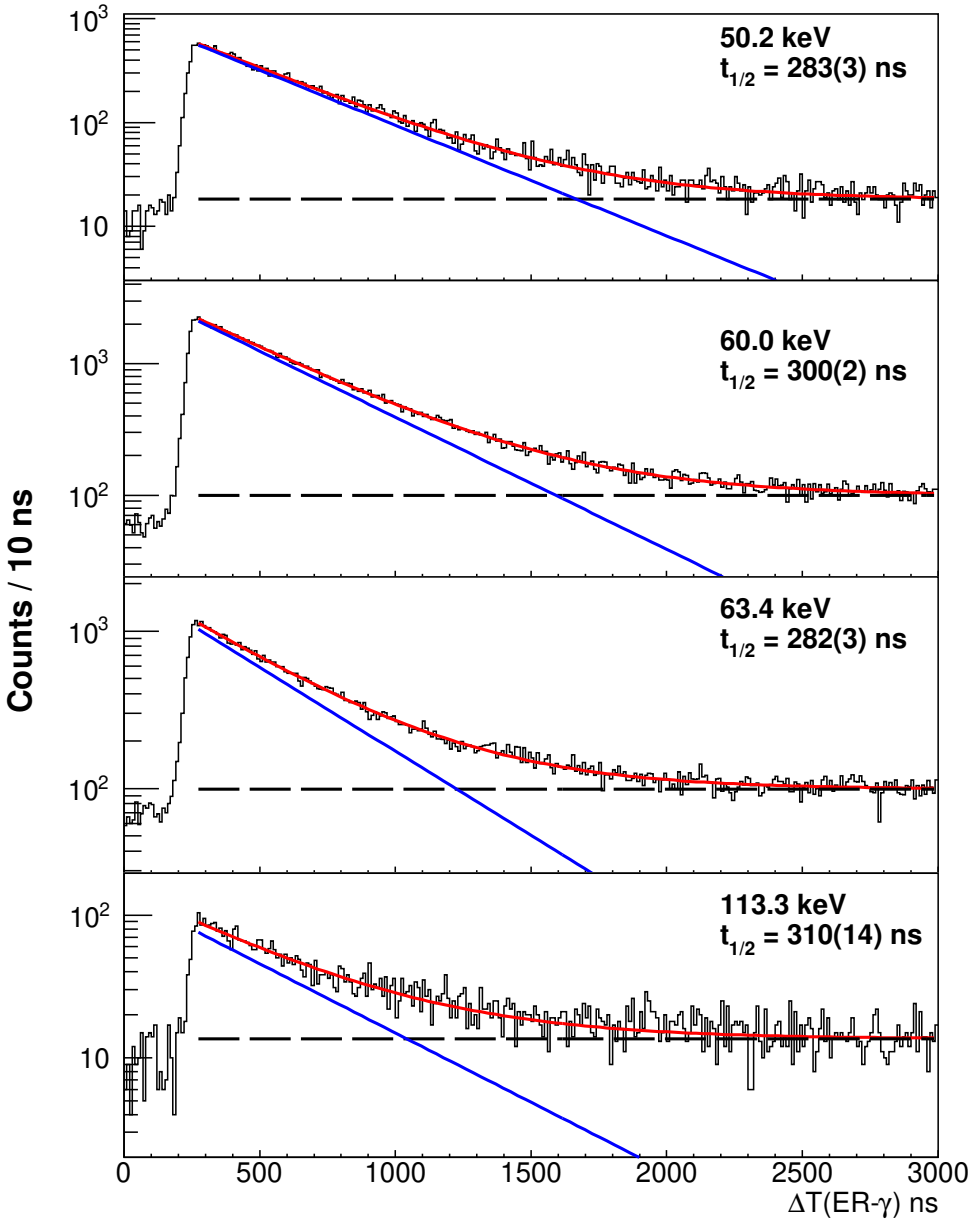

Fig. 5.6 The ER-PGD$_\gamma$ time difference for the γ-ray transitions assigned to the 294(7)-ns isomer in ^{178}Au, fitted with an exponential decay function plus constant background. Gates listed are $\pm$1 keV.

Multipolarity assignments

The multipolarities of the 60.0-, 50.2-, and 63.4-keV transitions were assigned based on their experimental total internal conversion coefficients $\alpha_{\text{tot,exp}}$. These were measured by comparing the number of events in the ER-PGD$_\gamma$ singles and the number of coincidence isomeric transitions in the ER-PGD$_{\gamma\gamma}$ matrix, where the difference is due to the internal conversion of the transition, after the correction for the γ-ray efficiency. Firstly the experimental total internal conversion coefficient ($\alpha_{\text{tot,exp}}$) for the 63.4-keV transition is calculated using the 50.2-63.4-keV cascade with,

$$\alpha_{\text{tot,exp}}(63.4) = \frac{\text{N}_\gamma(50.2) \times \varepsilon(63.4)}{\text{N}_{\gamma\gamma}(50.2-63.4)} - 1, \tag{5.2}$$

where $\varepsilon(63.4)$ is the detection efficiency of the PGD at 63.4-keV taken from simulations [51]. Similarly the ICC's of the 60.0-keV and 50.2-keV transitions was deduced using the 60.0-50.2-keV cascade with the equivalent method,

$$\alpha_{\text{tot,exp}}(60.0) = \frac{\text{N}_\gamma(50.2) \times \varepsilon(60.0)}{\text{N}_{\gamma\gamma}(50.2-60.0)} - 1, \tag{5.3}$$

and,

$$\alpha_{\text{tot,exp}}(50.2) = \frac{\text{N}_\gamma(60.0) \times \varepsilon(50.2)}{\text{N}_{\gamma\gamma}(50.2-60.0)} - 1, \tag{5.4}$$

The resulting $\alpha_{\text{tot,exp}}$ values are shown in Table 5.1 along with theoretical total internal conversion coefficients ($\alpha_{\text{tot, th}}$) values calculated using the BrIcc code [59], and deduced transition strengths calculated using a 294-ns half-life for all transitions.

Table 5.1 Total experimental and theoretical ICC for γ-ray transitions from the 294-ns isomer above ^{178}Au^g. Details in text. The relative intensity of each transition I_{rel}, is normalised to the 60.0-keV transition.

E_γ (keV)	I_{rel}	$\alpha_{\text{tot,exp}}$	$\alpha_{\text{tot,th}}$(M1)	$\alpha_{\text{tot,th}}$(E2)	δ^2(E2/M1)	B(M1) W.u	B(E2) W.u
50.2(2)	94(1)	19.3(25)	9.74(18)	123(3)	0.55(7)	$2.5(4) \times 10^{-5}$	0.39(6)
60.0(2)	100	10.4(12)	5.77(10)	51.8(12)	0.58(5)	$2.7(4) \times 10^{-5}$	0.37(6)
63.4(2)	94(1)	21.3(27)	4.91(18)	39.7(9)	0.97(15)	$6.5(10) \times 10^{-6}$	0.63(10)
113.4(4)	6(1)		5.06(9)	3.11(7)			0.025(4)

Additionally a second independent method was also used to calculate $\alpha_{\text{tot,exp}}(50.2)$, outlined in Sec. 5.5. This resulted in a value of $\alpha_{\text{tot, exp}}(50.2) = 19.7(53)$, fully consistent with the method outlined in this section.

It can be seen that the deduced values of $\alpha_{\text{tot,exp}}$ for the 50.2-, 60.0-, and 63.4-keV transitions are much lower than the theoretical values for $E2$ assignments. The 50.2-, 60.0- and 63.4-keV transitions were assigned a mixing ratio based on the experimental internal conversion coefficient and theoretical ICC for $E2$ and $M1$ transitions. The mixing ratio $\delta^2(E2/M1)$ is defined by,

$$\delta^2(E2/M1) = \frac{T(E2)}{T(M1)}, \tag{5.5}$$

where $T(E2)$ and $T(M1)$ are the probability of an $E2$ and $M1$ transition respectively. From this definition it can be shown that the mixing ratio can deduced from the experimental and theoretical values of the ICC using,

$$\delta^2(E2/M1) = \frac{\alpha_{\text{tot,exp}} - \alpha_{\text{tot,th}}(M1)}{\alpha_{\text{tot,th}}(E2) - \alpha_{\text{tot,th}}(M1)} \div \frac{\alpha_{\text{tot,exp}} - \alpha_{\text{tot,th}}(E2)}{\alpha_{\text{tot,th}}(M1) - \alpha_{\text{tot,th}}(E2)}. \tag{5.6}$$

The measured $\alpha_{\text{tot,exp}}$ values, suggest a mixed $M1/E2$ assignment for both the 60.0-keV transition [$\delta^2(E2/M1) = 0.55(20)$], and for the 50.2-keV transition [$\delta^2(E2/M1) = 0.58(4)$] whilst a strongly mixed $M1/E2$ nature [$\delta(E2/M1) = 0.97(37)$] is seen for the 63.4-keV transition. For the 113.4-keV transition the intensity was too low thus $\alpha_{\text{tot,exp}}(113.4)$ could not be calculated. As the 113.4-keV transition is known to decay parallel to the mixed $M1/E2$ 50.2-keV and 53.4-keV transitions, the decay must conserve parity. This means the 113.4-keV γ ray must also have multipolarity of either $M1$ or $E2$ or mixed.

5.2.2 373-ns isomer

The 56.7-keV isomeric transition seen in Fig. 5.3 had been previously placed above ^{178}Au$^{\text{m}}$ by Al-Monthery [27]. In this thesis PGD-$\gamma\gamma$ analysis was also performed for the 56.7-keV transition and in agreement with [27] no coincident transitions were found. A measurement of the half-life of the 56.7-keV transition was repeated using the same method described previously and shown in Fig. 5.7. The resulting half-life of 373(9)-ns was within error of the previously measured value 390(10)-ns. The ICC of the 56.7-keV transition could not be measured in the same way described for transitions from the 294-ns isomer, however an alternative derivation was performed by instead utilising a combination of prompt and isomeric

γ-ray spectroscopy outlined in Sec. 5.5. This resulted in value of $\alpha_{\mathrm{tot,exp}}(56.7) = 23(5)$ with the multipolarity assignment discussed in Sec. 5.5.

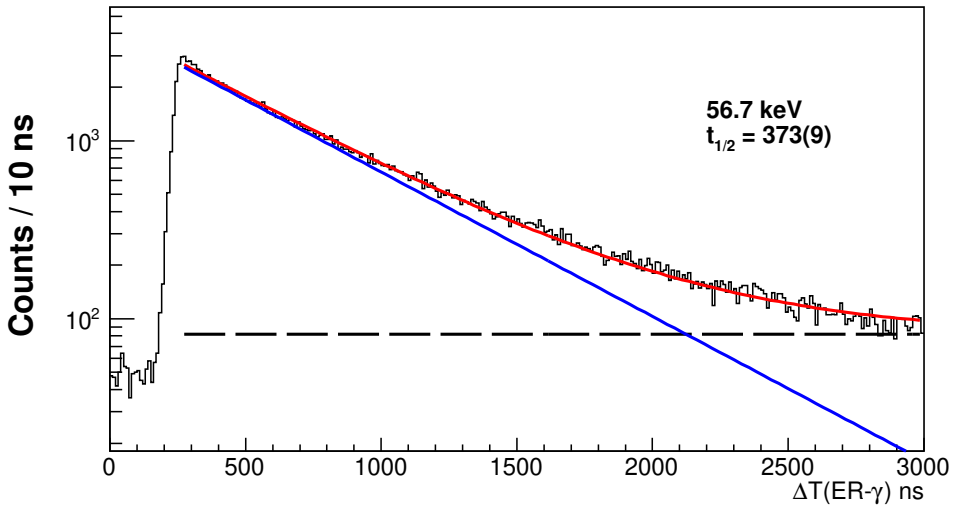

Fig. 5.7 The ER-PGD$_\gamma$ time difference for the 56.7-keV transition, fitted with an exponential decay function plus constant background.

5.3 Prompt γ-ray spectroscopy

This section discusses excited states identified above the 294-ns and 373-ns isomers. Due to the long half-life and small α-decay branching ratios of ^{178}Au$^{\mathrm{g,m}}$ combined with the high recoil implantation rate, the recoil decay tagging technique (see Sec. 4.6.4) could not be used to identify γ-ray transitions of ^{178}Au. This was because the respective analysis resulted in γ-ray spectra highly contaminated by γ rays from other ER's. Therefore, with knowledge of isomeric transitions established, the isomer decay tagging technique (described in Sec. 4.6.5) was used. Two rotational prompt band structures were identified above the 373-ns isomer and several prompt transitions were also seen above the 294-ns isomer using the JUROGAM-II spectrometer.

5.3.1 Structure above the 373-ns isomer

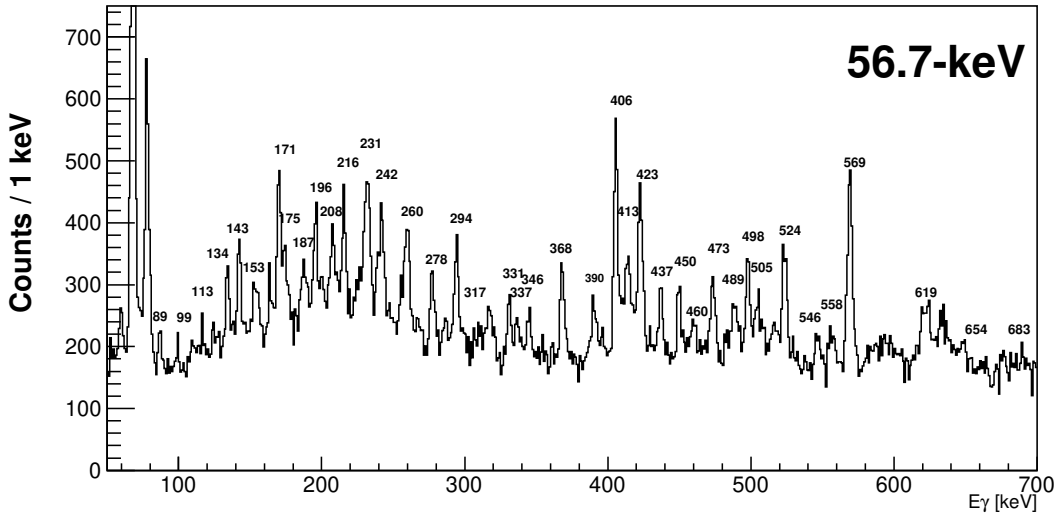

Fig. 5.8 JGII γ-ray spectrum gated by the 56.7-keV isomeric transition as seen in the PGD. An energy gate of $\pm$1-keV was applied with a time gate $0 \leq \Delta T$(ER-PGD) ≤ 1 μs. Time random background subtracted for -1 μs$\leq \Delta T$(ER-PGD) ≤ 0 μs.

To identify transitions above the 373-ns state IDT was used. Fig. 5.8 shows recoil-gated JUROGAM-II singles spectrum tagged on the 56.7-keV isomeric transition in the planar detector [ER-PGD(56.7)-JGII$_\gamma$] with the observed γ rays listed in Table 5.2. The 56.7-keV gate provided the cleanest and highest intensity γ-ray spectrum for transitions above the 373-ns isomer. To deduce the level scheme, $\gamma\gamma$ coincidences were also needed, therefore the ER-PGD(56.7)-JGII$_{\gamma\gamma}$ matrix was also produced. This matrix was constructed in the same way as the IDT-JGII$_\gamma$ singles but with an additional condition that JGII events must be fold-2 or greater and ΔT(JGII$_\gamma -$ JGII$_\gamma$) ≤ 100 ns. The IDT$_{\gamma\gamma}$ matrix however, had insufficient intensity as to be used alone to identify some structures in ^{178}Au, therefore to increase statistics the recoil-tagged JGII$_{\gamma\gamma}$ matrix was analysed along with the IDT$_{\gamma\gamma}$ matrix to construct the level scheme.

Two rotational structures, band-1 and band-2, were identified above the 373-ns isomer, shown in Fig. 5.9 and discussed in detail below.

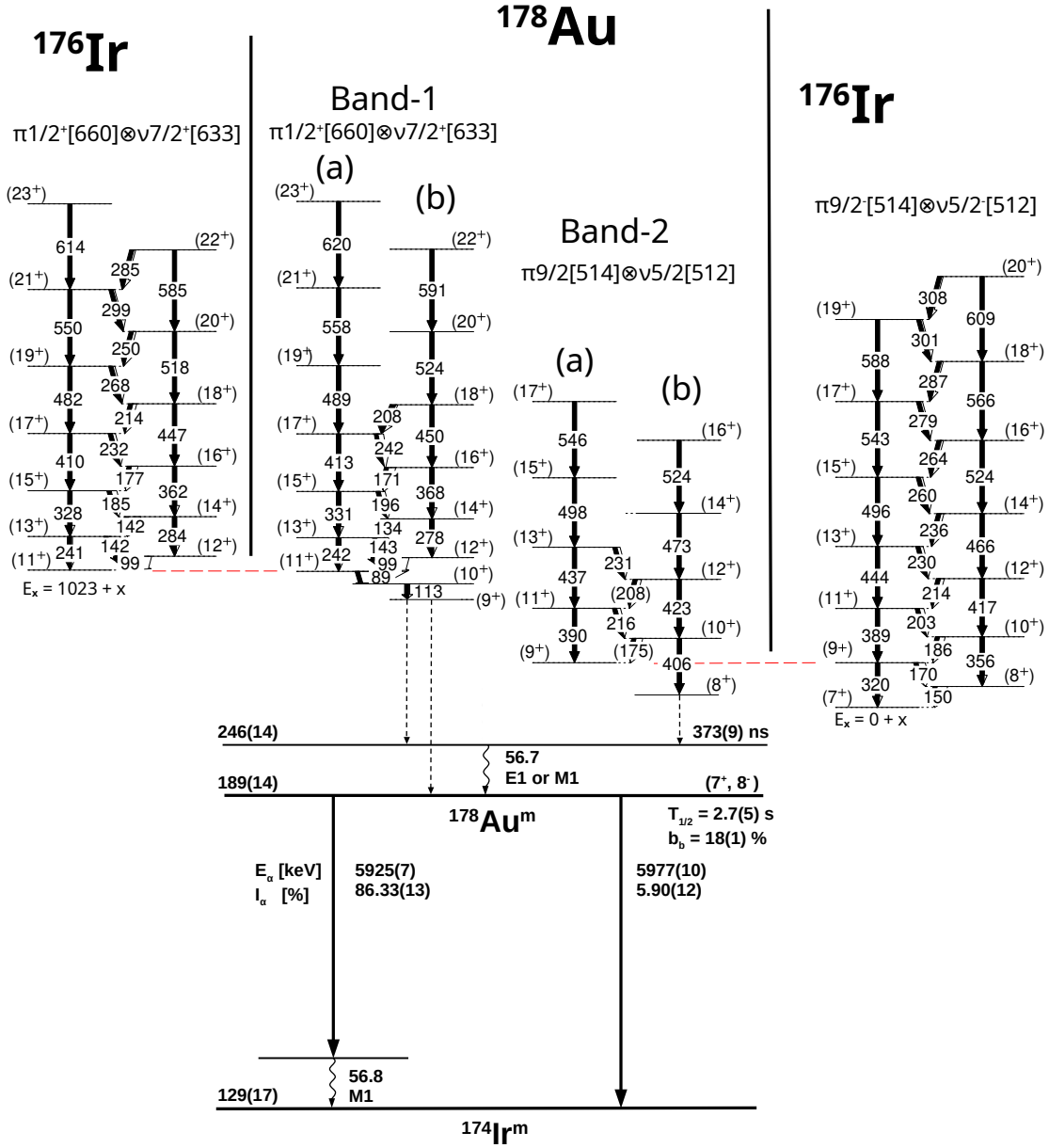

Fig. 5.9 Proposed level schemes for bands 1 and 2 in ^{178}Au. Transitions marked with brackets are observed in Fig. 5.8 however could not be directly placed using $\gamma\gamma$ coincidences. The known floating $\pi 1/2^+[660] \otimes \nu 7/2^+[633]$ and $\pi 9/2^-[514] \otimes \nu 5/2^-[512]$ bands in the isotonic ^{176}Ir [2] are shown for comparison with the excitation energies normalised to the (11^+) and (9^+) states of ^{176}Ir as is indicated by the dashed red lines. All spin-parity assignments are tentative and therefore shown in brackets.

Band-1

Figure 5.10 shows the recoil-gated JUROGAM-II $\gamma\gamma$ projections with gates on the 89-, 99- and 113-keV transitions identified using IDT. In all JGII$_{\gamma\gamma}$ projections shown, a background subtraction was performed by subtracting a second projection adjacent to the gated γ-ray peak and of equal width. The 89-, 99-, and 113-keV transitions were firmly placed at the bottom of band-1 and are seen in coincidence with all transitions in band-1(a) and band-1(b).

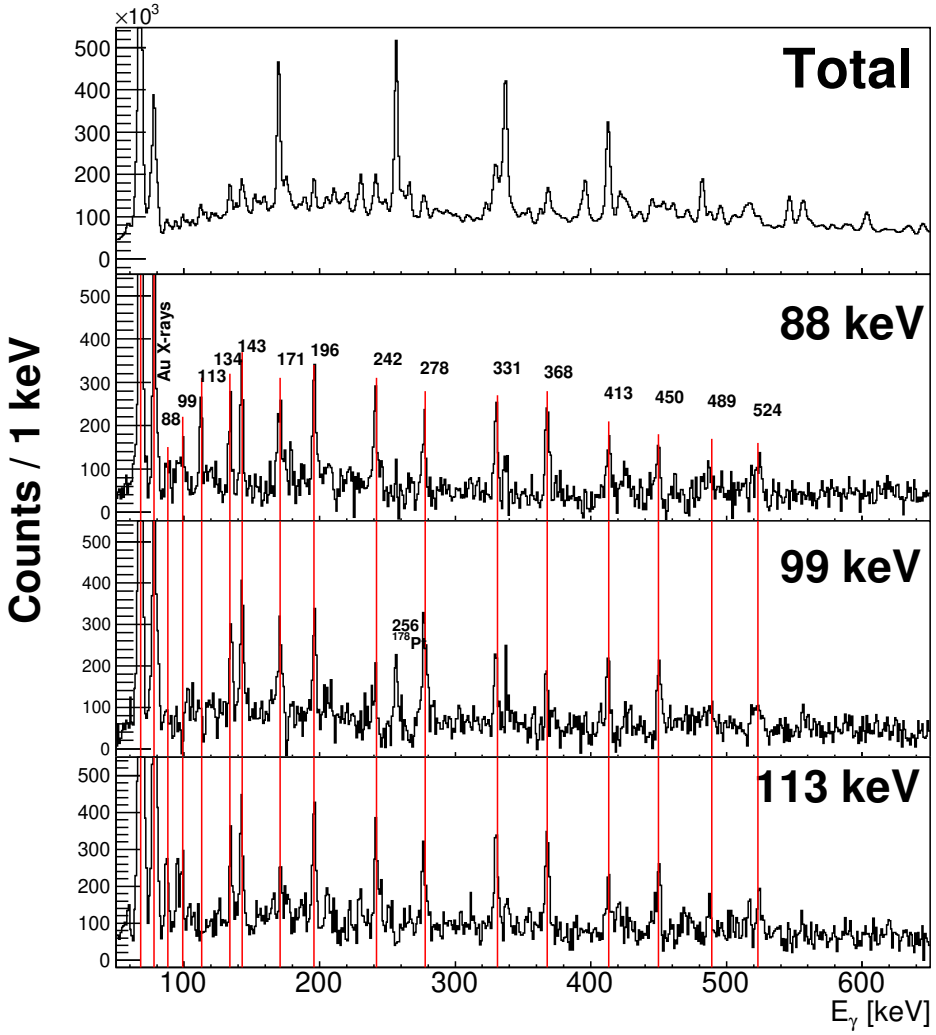

Fig. 5.10 ER-JGII$_{\gamma\gamma}$ γ-ray spectra of the total projection, and in coincidence with the 89-, 99- and 113-keV transitions $\pm$1-keV. The 99-keV gate shows some weak contamination from ^{178}Pt, with the yrast $4^+ \rightarrow 2^+$ 256-keV transition labelled.

In all three projections the two rotational structures of band-1(a) and band-1(b) are visible with all coincident transitions previously seen in the IDT JGII singles in Fig. 5.8. Characteristic Au K x-rays ($K_{\alpha_1} = 68.8$, $K_{\alpha_2} = 67.0$, and $K_{\beta_1} = 78.0$ keV) are also observed, while the known bands in neighbouring ^{177,179}Au are not visible [60, 20]. Contamination from the strongly-produced yrast band of ^{178}Pt [61] (see Fig. 4.7) is seen in the 99-keV projection.

Figure 5.11 shows the γ-ray spectra with gates on the 134-, 278- and 450-keV transitions. These spectra establish the 591-keV→524-keV→450-keV→368-keV→278-keV cascade of band-1(b).

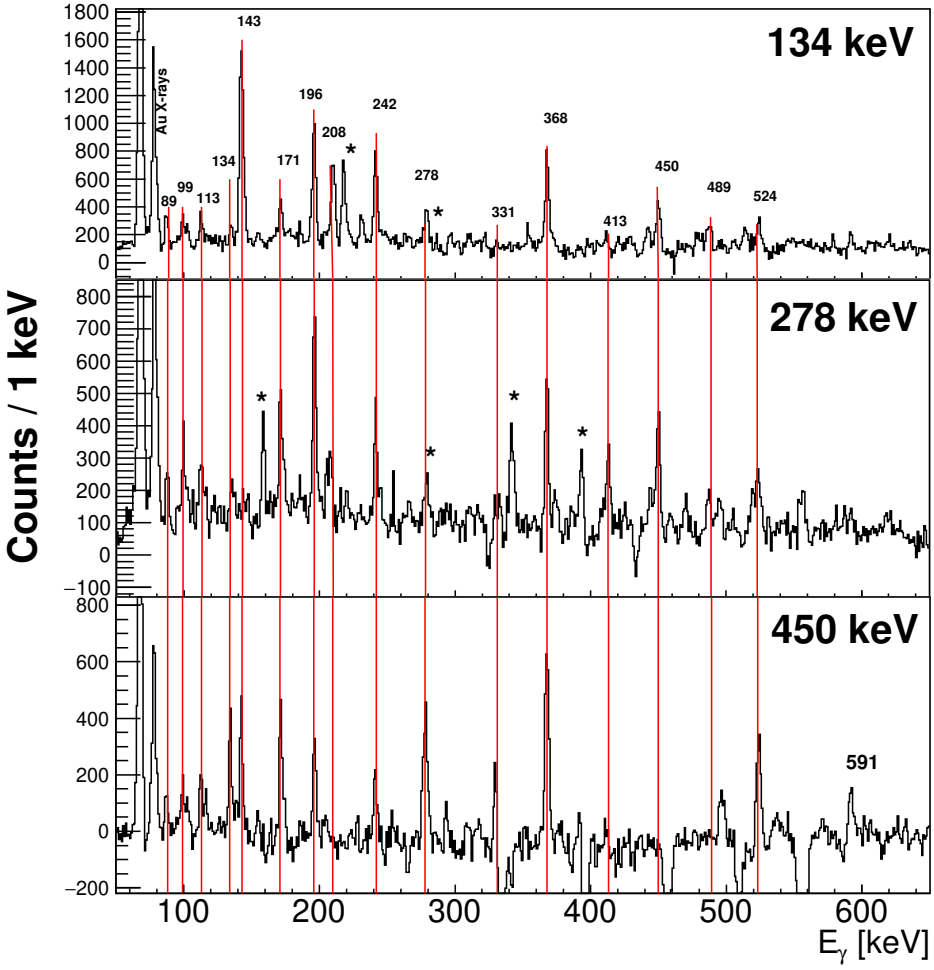

Fig. 5.11 ER-JGII$_{\gamma\gamma}$ γ-ray spectra in coincidence with the 134-keV, 278-keV and 450-keV transitions $\pm$1-keV. Contaminating transitions from ^{179}Hg are marked by a *.

The construction of band-1(a) is demonstrated in Fig. 5.12 with the 620→558→489→413→331→242-keV cascade visible in the 489-keV and 620-keV gates.

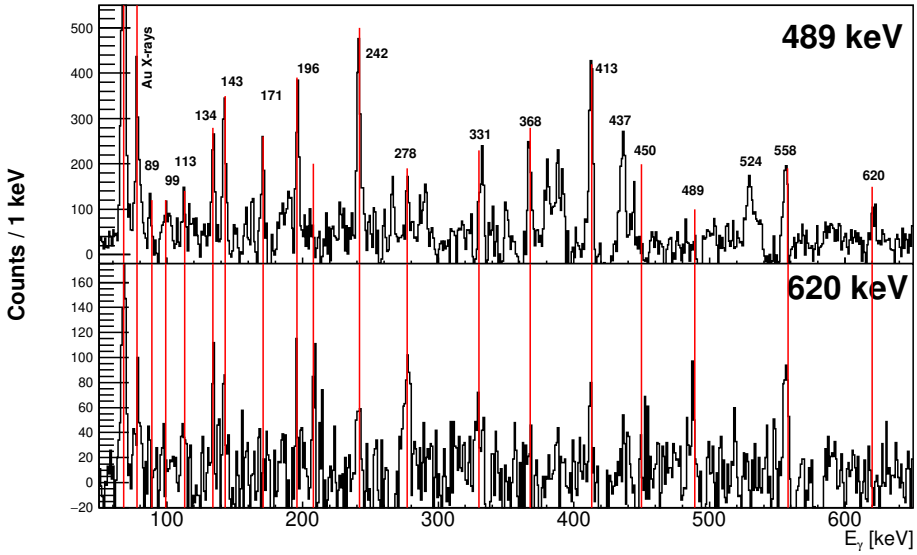

Fig. 5.12 ER-JGII$_{\gamma\gamma}$ γ-ray spectra in coincidence with the 489-keV and 620-keV transitions $\pm$1-keV.

Projections using the 331-, 413- and 558-keV transitions in band-1(a) could not be cleanly produced due to high γ-ray contribution from other isotopes. A weak 620-keV was seen above the 558-keV γ ray, however no higher-spin states could be identified.

Lower energy transitions that link band-1(a) and band-1(b) are seen in Figs. 5.10-5.12. One example of this are the strong 134-keV and 143-keV transitions, who's energies sum to 278-keV and which are not seen in coincidence with the 278-keV transition of band-1(b). The same 134-keV γ ray and the 196-keV γ ray sum to the 331-keV transition and are placed parallel to the 331-keV transition of band-1(a). This orders the placement 143-, 134-, 196-, 278-, and 331-keV transitions as well as establishing the relative excitation energies between states in band-1(a) and (b).

Another example of an inter-band transition in band-1 is shown in Fig. 5.13. The 208-keV transition is seen in coincidence with all γ rays in band-1 except for the 450- and 489-keV transitions. The 208- and 242-keV sum to the 450-keV transition ordering the placement of the 208- and a second 242-keV. This means that the 242-keV transition observed in Fig. 5.8 is a doublet of two separate transitions both in band-1, with one placed at the bottom of

band-1(a) and the second being a inter-band transition between band-1(a) and (b). This is confirmed by projections shown in Fig. 5.13 in which the 242-keV γ ray is seen in coincidence with a second 242-keV transition, and is consistent with the 171- and 242-keV γ rays summing to the 413-keV transition.

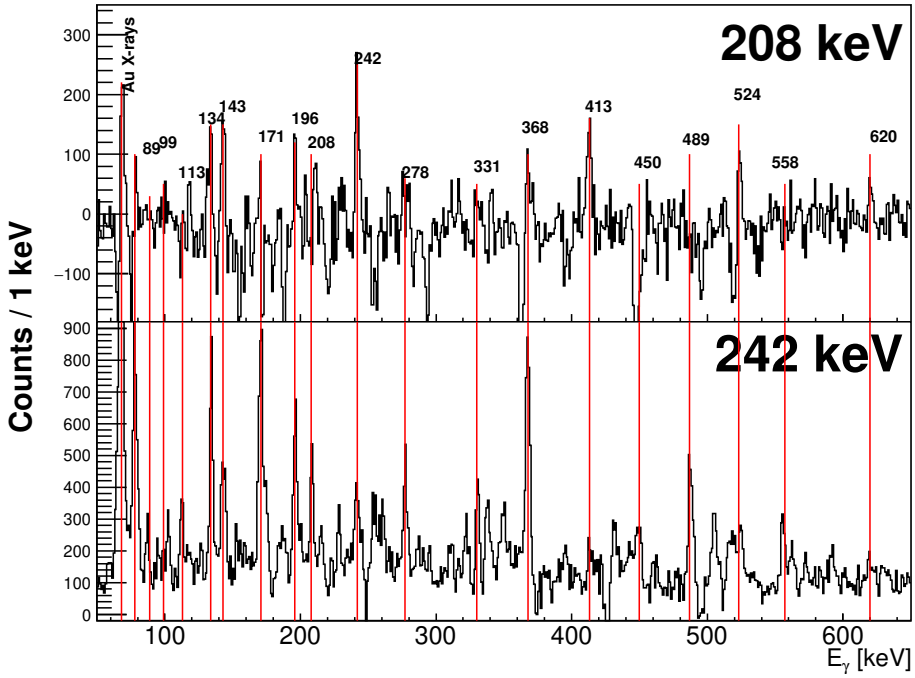

Fig. 5.13 ER-JGII$_{\gamma\gamma}$ γ-ray spectra in coincidence with the 208-keV and 242-keV transitions $\pm$1-keV.

As will be discussed in Chap.6, band-1 is tentatively assigned as the $\pi 1/2^+[660] \otimes \nu 7/2^+[633]$ band based on analogy with similar structures seen in neighbouring odd-odd nuclei, in particular with the isotonic ^{176}Ir as shown in Fig. 5.9, with related spin-parities assigned and listed in Table. 5.2. The 89-keV and 113-keV transitions are both seen in coincidence with all transitions in band-1, and therefore are placed below the bandhead, but cannot be ordered. These transitions were assigned multipolarity $M1$, as an $E1$ multipolarity was clearly ruled out by the low intensity seen in Fig. 5.8. Band-1 could not be directly connected to the 373-ns isomer and as such is illustrated as a floating band in Fig. 5.9.

The $\gamma\gamma$ projections with gates on several transitions in band-1 allowed for the production of spectra with sufficiently high statistics and low contamination to perform DCO analysis (see Sect. 4.6.3). For these transitions R_{DCO} values were consistent with the assigned multi-

polarities and are listed in Table 5.2.

Band-2

Most remaining γ rays in Fig. 5.8, which were not assigned to band-1, were attributed to band-2 as discussed in this section. Band-2 was identified purely using the constructed ER-PGD(56.7)-JGII$_{\gamma\gamma}$ matrix because of the difficulty in obtaining clean recoil-gated JGII$_{\gamma\gamma}$ projections as was done for band-1 in Figs. 5.10-5.13. For example, the 423-, 473-, and 498-keV γ rays overlapped with transitions in the $K = 5/2^-$ band of ^{177}Pt, meaning that clean recoil-gated JGII$_{\gamma\gamma}$ spectra could not be produced by gating on these transitions. As a result, the intensity of $\gamma\gamma$ coincidences analysed was much lower than compared to band-1 making the establishment of band-2 more difficult.

Projections with gates on the 406-, 423-, and 473-keV γ rays are shown in Fig. 5.14 where the 406-, 423-, 473- and 524-keV transitions are all seen in mutual coincidence. This established the 524→473→423→406-keV cascade of band-2(b) seen in Fig. 5.9. It will be shown below the 406-keV transition is also in coincidence with transitions of band-2(b) and as such is placed at the bottom of band-2(a) as shown in Fig. 5.9. This also explains the strong intensity of the 406-keV γ ray seen in Fig. 5.8, as band-2 would preferentially de-excite to the 373-ns isomer via this transition.

Fig. 5.15 shows the projections gated on the 437, 498, and 545-keV γ rays with all three transitions in mutual coincidence with each other. Additionally a 390-keV transition is also seen in coincidence with all three transitions establishing the 545→498→437→390-keV cascade of band-2(a).

Several transitions from band-2(b) are also seen in coincidence to these decays indicating band-2(a) and (b) are parallel and linked. The 216- and 231-keV γ rays are seen in both Fig. 5.14 and 5.15 and are placed as inter-band transitions based on $\gamma\gamma$ coincidences. For example the 216-keV transition is seen in coincidence with all transitions in band-2 except for 423-keV. This places the 216-keV γ rays parallel to the 390-keV and 423-keV transitions. Additionally the weak 175-keV transition seen in Fig. 5.8 is not observed in coincidence with band-2, however may link band-2(a) and (b) as indicated in Fig. 5.9. Band-2 is assigned as the $\pi 9/2^-[514] \otimes \nu 5/2^-[512]$ based on analogy with a similar band in ^{176}Ir as discussed in Chapter 6, resulting in tentative spin-parity assignments and a $K = (7^+)$ bandhead.

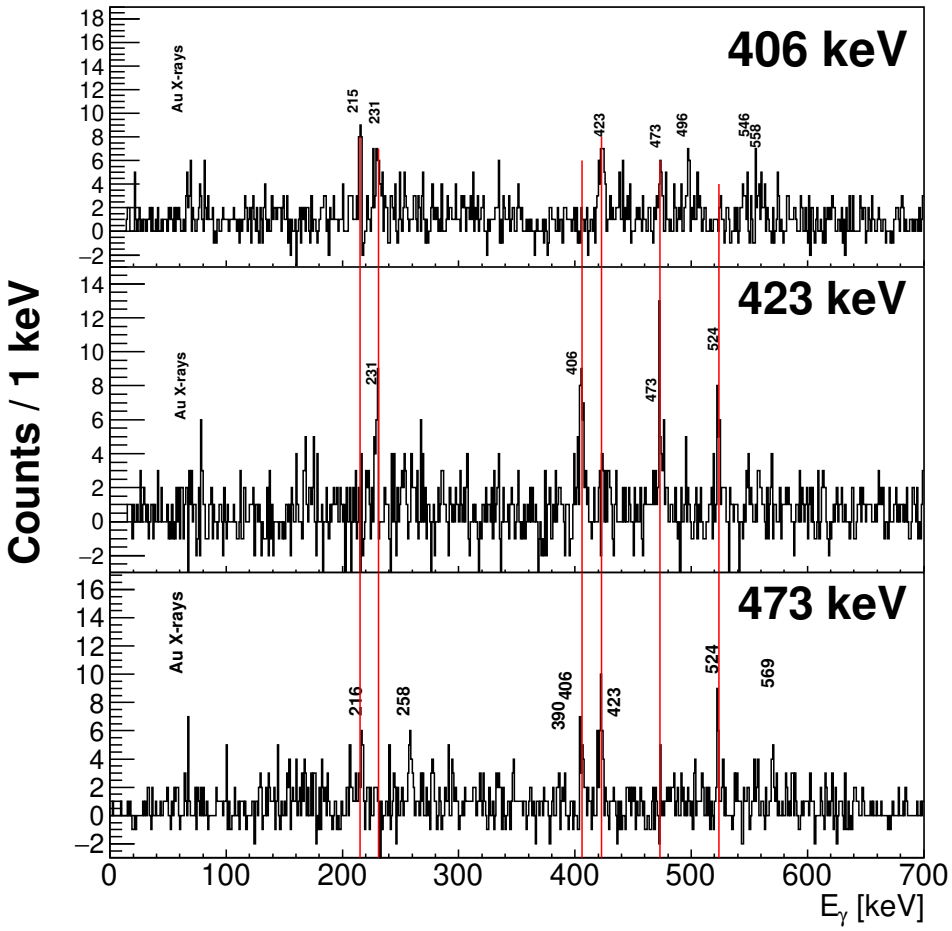

Fig. 5.14 ER-PGD(56.7)-JGII$_{\gamma\gamma}$ γ-ray spectra in coincidence with the 406-, 423- and 473-keV transitions $\pm$2-keV.

As clean recoil-gated $\gamma\gamma$ projections could not be made, DCO analysis was not performed on transitions in band-2 and multipolarities could not be confirmed using angular correlations. No transitions were seen decaying from the (9^+) state of band-2 meaning that transitions to $K = (7^+)$ bandhead could not be established. Furthermore no transitions linking the bandhead to the 373-ns isomer can be made.

Relative intensities of band-1 and band-2 in IDT JGII$_\gamma$ data

It can be seen by comparison of the $(18^+) \rightarrow (16^+)$ 450-keV transition from band-1(a) and the $(13^+) \rightarrow (11^+)$ 437-keV transition from band-2(a) in Fig. 5.8 that bands 1 and 2 have

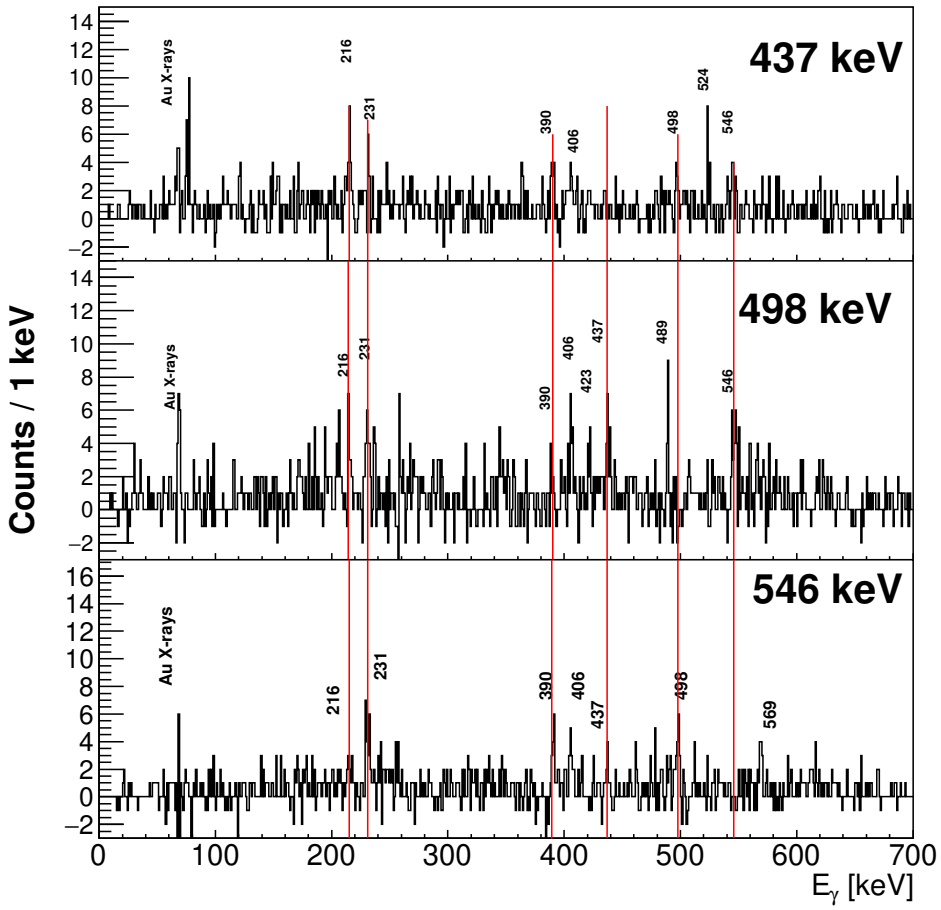

Fig. 5.15 ER-PGD(56.7)-JGII$_{\gamma\gamma}$ γ-ray spectra in coincidence with the 437-, 498- and 545-keV transitions $\pm$2-keV.

similar intensities in the IDT JGII γ-ray spectrum. This important fact will be used in Sec.5.5 to estimate the possible de-excitation from band-1 directly to the $(7^+, 8^-)$ α-decaying state bypassing the 373-ns isomer.

Unplaced transitions

Despite being the strongest transition seen in Fig 5.8, the 569-keV transition could not be placed in the decay scheme. Figure 5.16 shows the projection of the ER-PGD(56.7)-JGII$_{\gamma\gamma}$ matrix gated on the 569-keV transitions in which the 489-keV and 473-keV transitions are seen in coincidence which could be from decays in band-1 and band-2 respectively. No other transitions from band-1 or band-2 are seen in coincidence however.

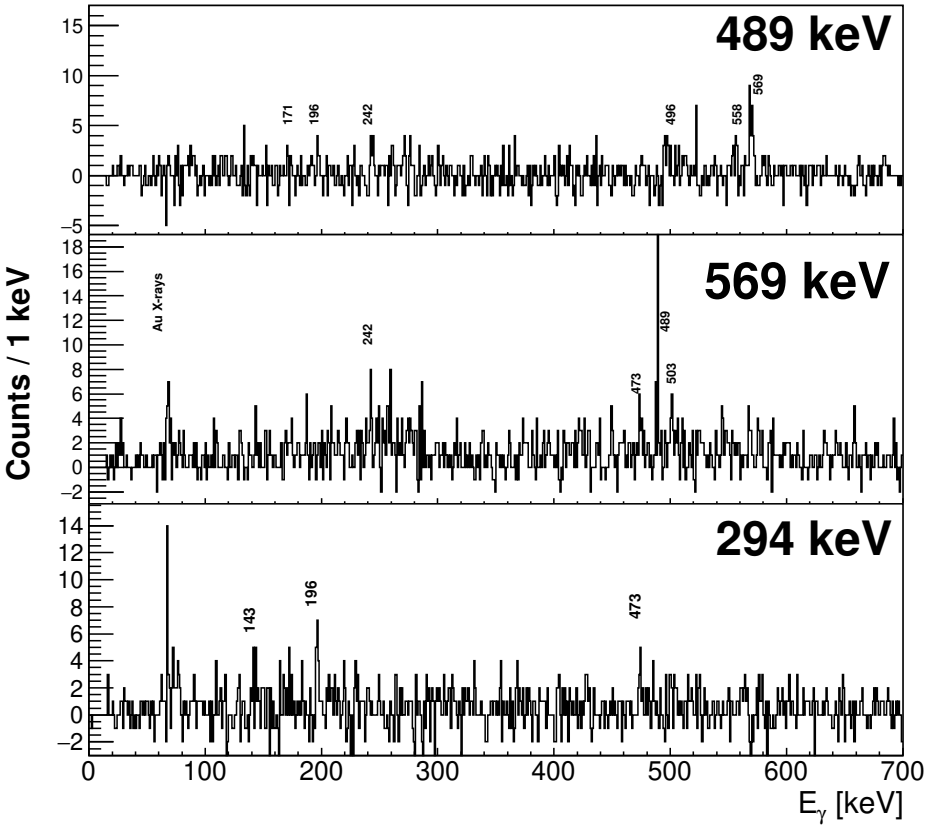

Fig. 5.16 ER-PGD(56.7)-JGII$_{\gamma\gamma}$ γ-ray spectra in coincidence with the 489-keV, 569-keV and 294-keV transitions $\pm$2-keV.

The 569-keV had insufficient intensity in the recoil-gated JGII$_{\gamma\gamma}$ matrix to establish any additional coincidences. The high intensity of the 569-keV transition as seen in Fig. 5.8 would be explained however if states in band-1 or band-2 de-excited to the 373-ns isomer via the 569-keV transition, but no confirmation of this was found.

The high intensity 294-keV γ ray seen in Fig. 5.8 is also unplaced, with coincident transitions shown in the bottom panel of Fig. 5.16 in which only the 143-, 196- and 473-keV γ rays are seen in coincidence. The 143- and 196-keV transitions may be members of band-1 and the 473-keV transition may be from band-2, however this cannot be confirmed without additional coincidences from these bands.

Several other transitions identified in Fig. 5.8 were not placed due to insufficient statistics in IDT JGII$_{\gamma\gamma}$ analysis and are listed in Table 5.2.

Table 5.2 Energies E_γ, excitation energies E_i, initial and final spins I_i^π and I_f^π, respectively, and relative intensities $I_\gamma(\%)$ obtained from JUROGAM II data for γ-ray transitions identified above the 373-ns isomer in Fig. 5.8. The angular distribution ratios R_{DCO} (see section 4.6.3) are listed with resulting multipolarities listed in bold. For transitions where DCO analysis was not possible multipolarities were established by analogy to ^{176}Ir and listed in normal font. Intensities are normalised against the 368 keV ($16^+ \rightarrow 14^+$) transition. Excitation energies are relative to the (11^+) state in band-1 (x), and the (8^+) state in band-2 (y).

E_γ (keV)	E_i(keV)	I_i^π	I_f^π	$I_\gamma(\%)$	R_{DCO}	Multipolarity
Band-1						
88.6(6)		$(10^+,11^+)$	$(9^+,10^+)$	29(6)		$(M1)$
98.9(2)	98.9+x	(12^+)	(11^+)	36(5)		$(M1)$
113.0(7)		$(10^+,11^+)$	$(9^+,10^+)$	23(8)		$(M1)$
134.3(1)	376.3+x	(14^+)	(13^+)	62(7)	0.73(11)	(**M1**)
142.6(1)	242.4+x	(13^+)	(12^+)	105(9)	0.45(8)	(**M1**)
170.5(1)	743.7+x	(16^+)	(15^+)	164(10)	0.59(10)	(**M1**)
196.0(1)	572.3+x	(15^+)	(14^+)	100(10)	0.82(12)	(**M1**)
207.5(2)	1717.4+x	(18^+)	(17^+)	69(11)		$(M1)$
241.5(6)	242.4+x	(13^+)	(11^+)			$(E2)$
242.4(6)	1473.4+x	(17^+)	(16^+)			$(M1)$
277.5(2)	376.3+x	(14^+)	(12^+)	98(10)	1.63(27)	(**E2**)
330.8(2)	572.3+x	(15^+)	(13^+)	73(8)	1.31(20)	(**E2**)
367.9(9)	743.7+x	(16^+)	(14^+)	$\equiv 100$	1.07(16)	(**E2**)
412.8(2)	984.6+x	(17^+)	(15^+)	63(6)		$(E2)$
450.0(1)	1193.7+x	(18^+)	(16^+)	71(6)	1.16(17)	(**E2**)
488.8(2)	1473.4+x	(19^+)	(17^+)	69(8)		$(E2)$
523.8(1)	1717.4+x	(20^+)	(18^+)	153(8)		$(E2)$
557.6(1)	2031.0+x	(21^+)	(19^+)	52(6)		$(E2)$
591.1(4)	2308.6+x	(22^+)	(20^+)	10(4)		$(E2)$
619.7(5)	2650.6+x	(23^+)	(21^+)	29(9)		$(E2)$

Table 5.2 *(Continued.)*

E_γ (keV)	E_i(keV)	I_i^π	I_f^π	I_γ(%)	R_{DCO}	Multipolarity
Band-2						
175.0(2)	405.5+y	(10^+)	(9^+)	69(8)		$(M1)$
215.5(1)	620.8+y	(11^+)	(10^+)	98(11)		$(M1)$
231.3(1)	828.1+y	(13^+)	(12^+)	171(11)		$(M1)$
390.3(2)	230.5+y	(11^+)	(9^+)	50(6)		$(E2)$
405.5(1)	405.5+y	(10^+)	(8^+)	181(8)		$(E2)$
422.6(1)	828.1+y	(12^+)	(10^+)	136(7)		$(E2)$
437.1(1)	1301.4+y	(13^+)	(11^+)	77(6)		$(E2)$
473.3(1)	1301.4+y	(14^+)	(12^+)	98(7)		$(E2)$
498.0(2)	1555.9+y	(15^+)	(13^+)	65(7)		$(E2)$
523.8(1)	1825.2+y	(16^+)	(14^+)	143(8)		$(E2)$
546.4(2)	2102.3+y	(17^+)	(15^+)	56(6)		$(E2)$
Not Placed						
117.2(3)				26(6)		
154.0(7)				28(11)		
260.0(1)				134(9)		
294.2(1)				98(10)		
316.6(5)				41(11)		
337.4(3)				40(6)		
344.5(3)				50(7)		
458.9(5)				21(5)		
505.0(3)				3(6)		
569.1(1)				195(9)		
683.3(4)				15(6)		

5.3.2 Structure above the 294-ns isomer

Band-3, was constructed above the 294-ns isomer and is shown in Fig. 5.17. This band was established by means of analysis of IDT-JGII$_{\gamma\gamma}$ and ER-JGII$_{\gamma\gamma}$ matrices as well as a ER-JGII$_{\gamma\gamma\gamma}$ cube as discussed below.

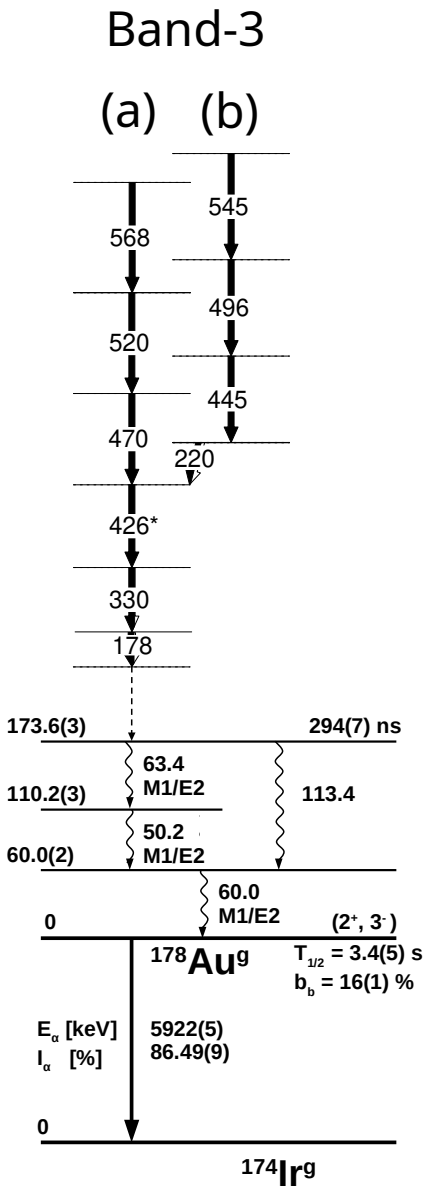

Fig. 5.17 Proposed level scheme for band-3, above the 294-ns isomer of ^{178}Au. The 426* denotes the 424-426-keV doublet, and the dashed line indicates that band-3 feeds to the 294-ns isomer in some way.

First JGII$_\gamma$ spectra gated by the 50.2-, 60.0-, 63.4- and 113.3-keV isomeric transitions were produced to identify prompt γ-ray transitions above the 294-ns isomer, they are shown in Fig. 5.18.

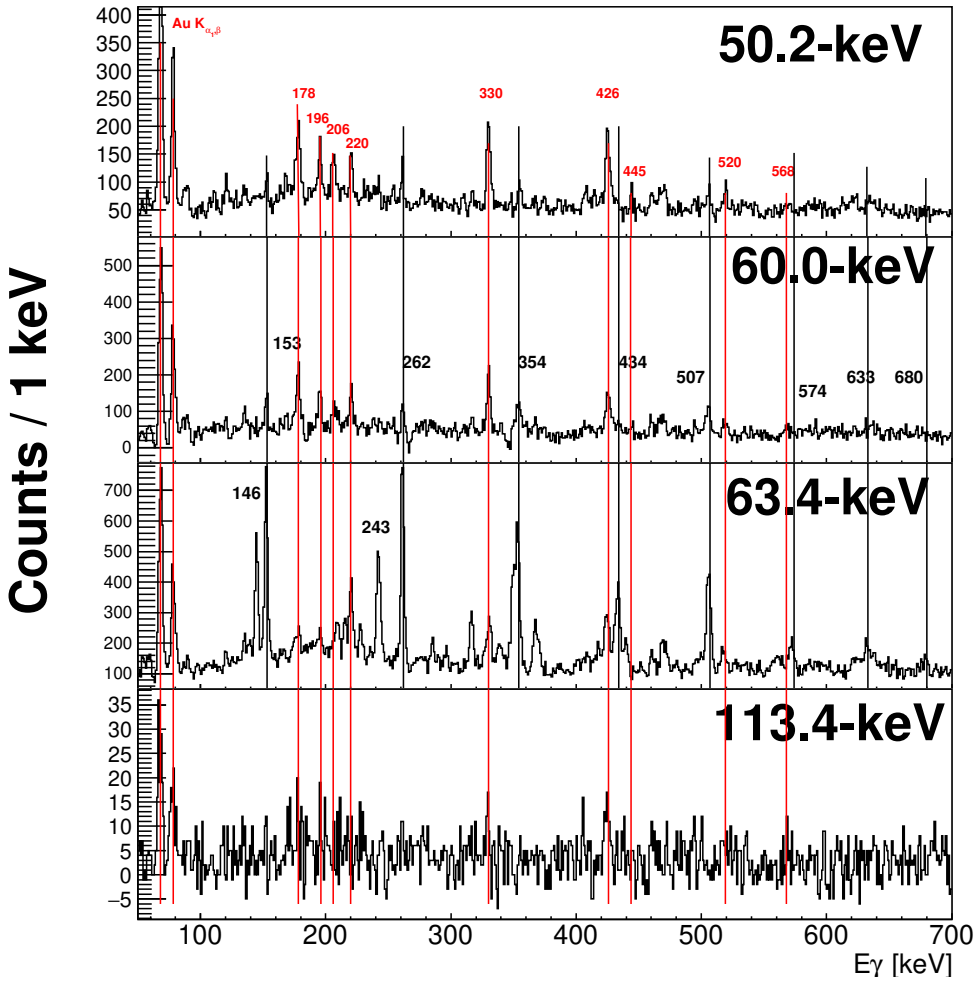

Fig. 5.18 ER-JGII$_\gamma$ γ-ray spectra gated by the 50.2-, 60.0-, 63.4-, and 113.4-keV transitions as seen in the PGD. An energy gate of $\pm$1-keV was applied with a time gate $0 \leq \Delta T\,(\text{ER-PGD}) \leq 1$ μs. Time random background subtracted for $-1 \leq \Delta T\,(\text{ER-PGD}) \leq 0$ μs. Peaks marked in red and black originate from ^{178}Au and ^{179}Au respectively.

In all spectra the characteristic Au x-rays ($K_{\alpha_1} = 68.8$, $K_{\alpha_2} = 67.0$, and $K_{\beta_1} = 78.0$ keV) are observed. In the spectra produced using the 60.0-keV and 63.4-keV gates the $K = 9/2^+$ rotational band of ^{179}Au can be seen and is dominant, with this contaminant caused by a strong 62.4-keV 328(2)-ns isomeric transition from ^{179}Au [21] partially overlapping with the PGD energy gates used. This contamination ruled out both the 60.0-keV and 63.4-keV gates to be used to identify transitions in ^{178}Au.

The JGII$_\gamma$ spectrum gated on the 50.2-keV transition produced the highest intensity γ-ray spectrum that was also free from contamination, therefore this was used to identify prompt transitions above

the 294-ns isomer and listed in Tab. 5.3. The 178-, 220-, 330-, and 426-keV transitions are seen strongly in the 50.2-keV gate but also in the other gates shown. It will be demonstrated below that all transitions shown in red belong to band-3.

To establish the placement of these transitions, the ER-PGD(50.2)-JGII$_{\gamma\gamma}$ matrix was constructed so that $\gamma\gamma$ coincidences above the 294-ns isomer could be analysed. Figure 5.19(a) shows the total projection of the PGD(50.2)-JGII$_{\gamma\gamma}$ matrix. The total projection confirmed all γ-ray transitions observed in Fig. 5.18 as well as the 470- and 496-keV transitions. The statistics in the PGD(50.2)-JGII$_{\gamma\gamma}$ matrix allowed for projections gated on the 178-, 220- and 330-keV transitions to be produced, shown in Fig 5.19(b-d).

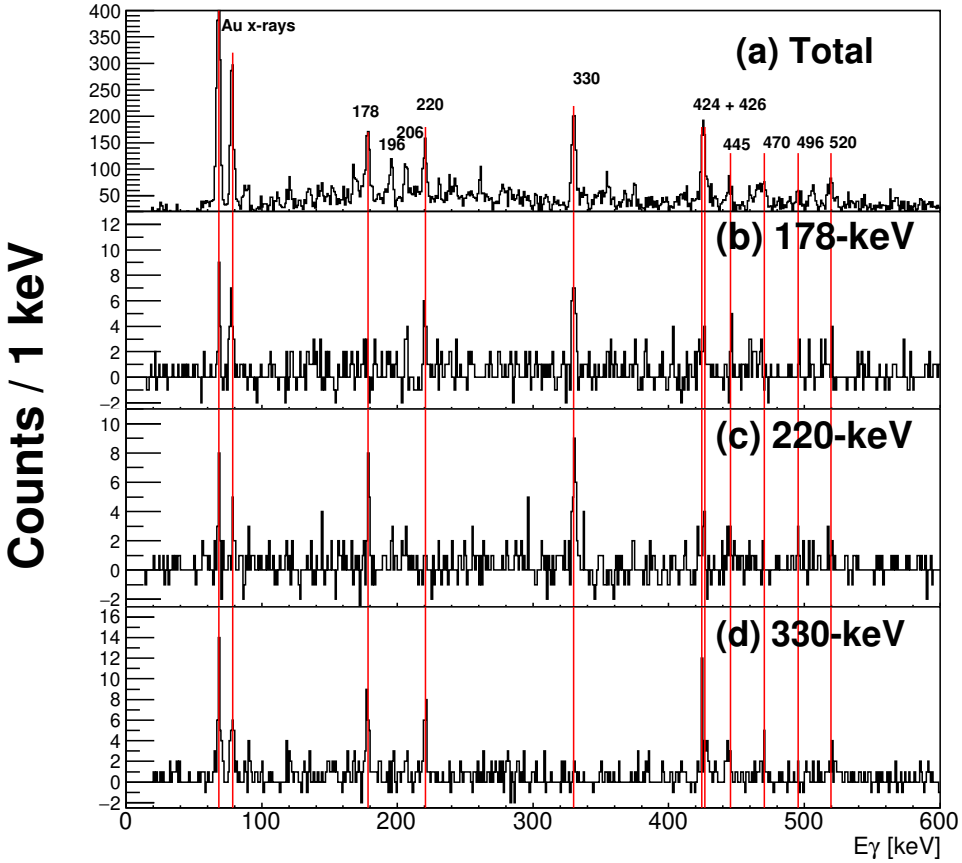

Fig. 5.19 ER-PGD(50.2)-JGII$_{\gamma\gamma}$, (a) total $\gamma\gamma$ projection, (b-d) in coincidence with the 178-, 220- and 330-keV transitions $\pm$2-keV respectively.

The 178-, 220-, 330- and 426-keV γ rays are all seen in mutual coincidence which suggested a possible rotational band including the 426$\rightarrow$330$\rightarrow$220$\rightarrow$178-keV transitions. Several higher energy transitions are observed at 445-, 470-, 496-, and 520-keV with these transitions placed above the

426-keV transition in band-3. The coincidences shown in Fig. 5.19 are weak however they will confirmed below by OR gates and recoil-gated JGII$_{\gamma\gamma}$ coincidences.

Projections gated on the 426-, 445, and 470-keV transitions are shown in Fig. 5.20, in which coincidences with the 178-, 330-, and 426-keV transitions are seen in all three projections. Of note is that the 426-keV transition is seen in apparent self coincidence. As will be shown below, most likely there are two closely spaced coincident transitions with one at 426-keV and the second at 424-keV. Therefore gating on the 426-keV transition includes some part of the 424-keV γ ray producing the apparent self coincidence and vice versa.

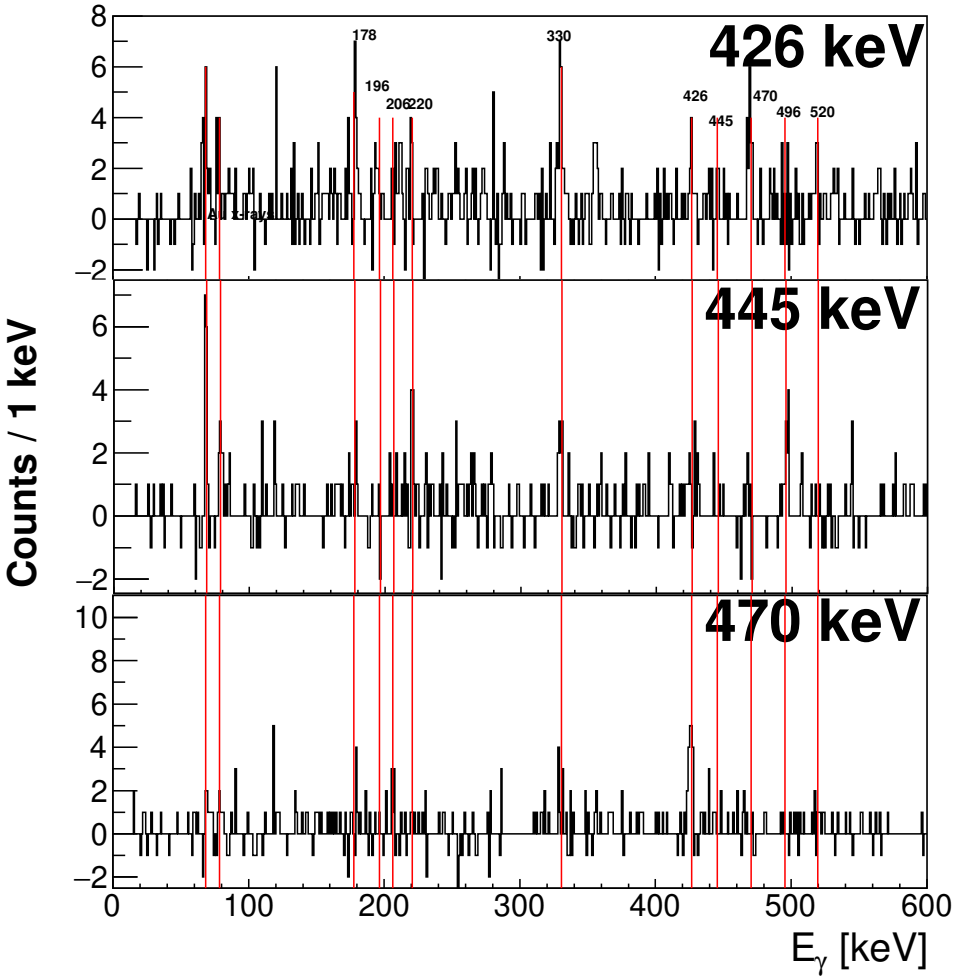

Fig. 5.20 ER-PGD(50.2)-JGII$_{\gamma\gamma}$ γ-ray spectra in coincidence with the 426-, 445- and 470-keV transitions $\pm$2-keV respectively.

In the projection gated on the 445-keV transition the 426 → 330 → 178-keV cascade of band-3(a) is weakly seen, and coincidences with the 496-keV transition and the 220-keV transition which joins band-3(b) to (a) are also observed. The projection gated on the 470-keV transition shows that the 220-keV and 470-keV transitions are not coincident, helping to establish the placement of the 220-keV transition parallel to the 470-keV, and below the 445-keV transition.

As the next step, projections on several transitions using an OR gate were used to better resolve and confirm coincident transitions using the low intensity ER-PGD(50.2-keV)-JGII$_{\gamma\gamma}$ matrix. Fig. 5.21(a) shows the projection gated on an OR of the 178-, 220-, 330-, and 426-keV transitions. The 426 → 330 → 178-keV cascade of band-3(a) is confirmed with several higher energy transitions from band-3(a) and (b) also seen at 445-, 470- and 520-keV.

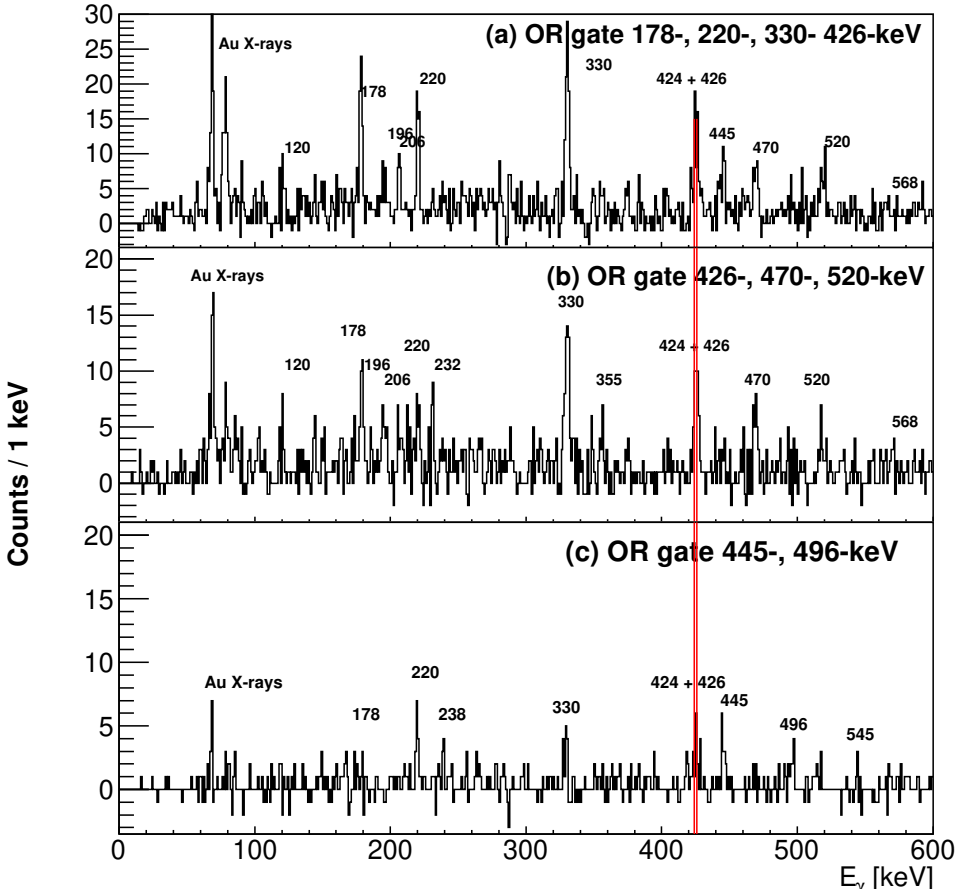

Fig. 5.21 ER-PGD(50.2)-JGII$_{\gamma\gamma}$ γ-ray spectra in coincidence with the (a) OR of 178-, 220-, 330-, 426-keV, (b) OR of 426-, 470-, 520-keV and (c) OR of 445-, 498-keV transitions $\pm$2 keV.

Figure 5.21(b) shows the γ rays coincident with the OR of 426-, 470-, 520-keV transitions, in which 568→520→470→426→330→178-keV cascade of band-3(a) is established. Band-3(b) further confirmed in Fig. 5.21(c) in which the 545→ 496 → 445-keV transitions are seen as well as the 220- and 426-keV transitions joining band-3(b) to (a).

To increase the intensity of $\gamma\gamma$ coincidences analysed, the recoil-gated JGII$_{\gamma\gamma}$ matrix was also used. This was possible as the known coincidences above the 294-ns isomer established in ER-PGD(50.2)-JGII$_{\gamma\gamma}$ analysis allowed for γ ray transitions from ^{178}Au to be more easily identified in the ER-JGII$_{\gamma\gamma}$ matrix. The total projection of the ER-JGII$_{\gamma\gamma}$ matrix and projections gated on the 178-keV, 220-keV and 330-keV γ rays are shown in Fig. 5.22. These projections are consistent with those produced using the IDT matrix previously shown in Fig. 5.19. Projections gated on the 178- and 330-keV transitions clearly establish the 520→ 470 → 426 → 330 → 178-keV cascade of band-3(a).

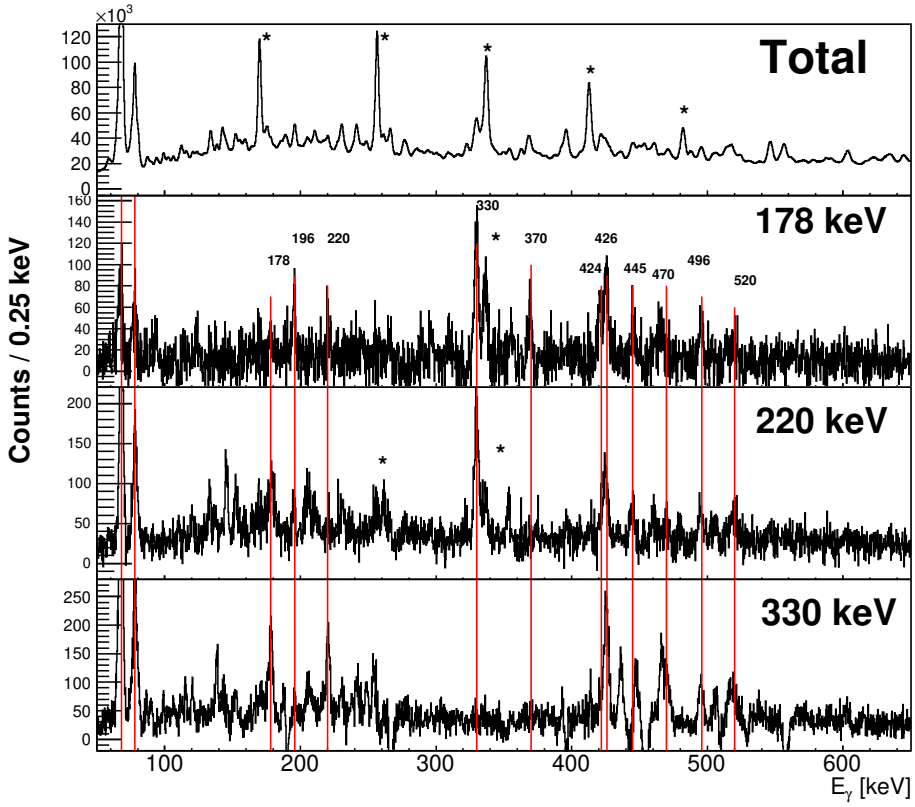

Fig. 5.22 ER-JGII$_{\gamma\gamma}$ γ-ray spectra, total projection and gated on the 178-, 220- and 330-keV γ rays $\pm$1-keV. Transitions marked with a * originate from ^{178}Pt.

The top panel of Fig 5.23 shows the projection of the ER-JGII$_{\gamma\gamma}$ matrix gated on the 426-keV transition. This shows the 426-keV transition is in coincidence with a 424- γ-ray. Initially this coinci-

dence was believed to be a contamination from some other nuclei, however this same coincidence was seen in the ER-PGD(50.2)-JGII$_{\gamma\gamma}$ matrix (see Fig. 5.20). Based on the data it seems that the 424-426-keV γ-rays are in coincidence, however these transitions cannot be well separated with our gates as the γ-ray energies are too close to each other. Therefore similarly to as was mentioned earlier (see discussion of Fig. 5.20), this might create an appearance of 426-426-keV pair in self coincidence. Throughout this text '426-keV' will be used to denote the 424-426-keV pair.

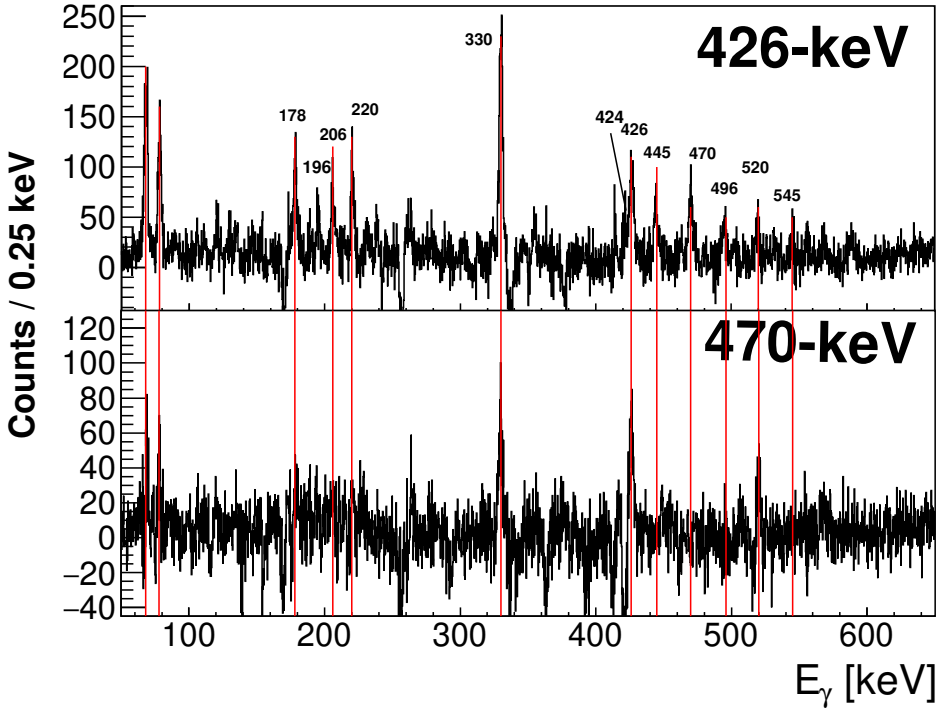

Fig. 5.23 ER-JGII$_{\gamma\gamma}$ γ-ray spectra gated on the 426- and 470-keV transitions $\pm$1-keV.

The bottom panel of Fig. 5.23 shows the projection of the ER-JGII$_{\gamma\gamma}$ matrix gated on the 470-keV transition in which strong coincidence is clearly seen with the 520-, 426- and 330-keV transitions establishing band3-(a).

The intensity of the 330-, and 426-keV transitions was sufficiently high that recoil-gated $\gamma\gamma\gamma$ coincidences could be analysed for several transitions in band-3. Figure 5.24 shows the background subtracted projection of the ER-JGII$_{\gamma\gamma\gamma}$ cube gated on (a) the 220- AND 426-, (b) the 220- AND 330- and (c) the 330- AND 426-keV transitions.

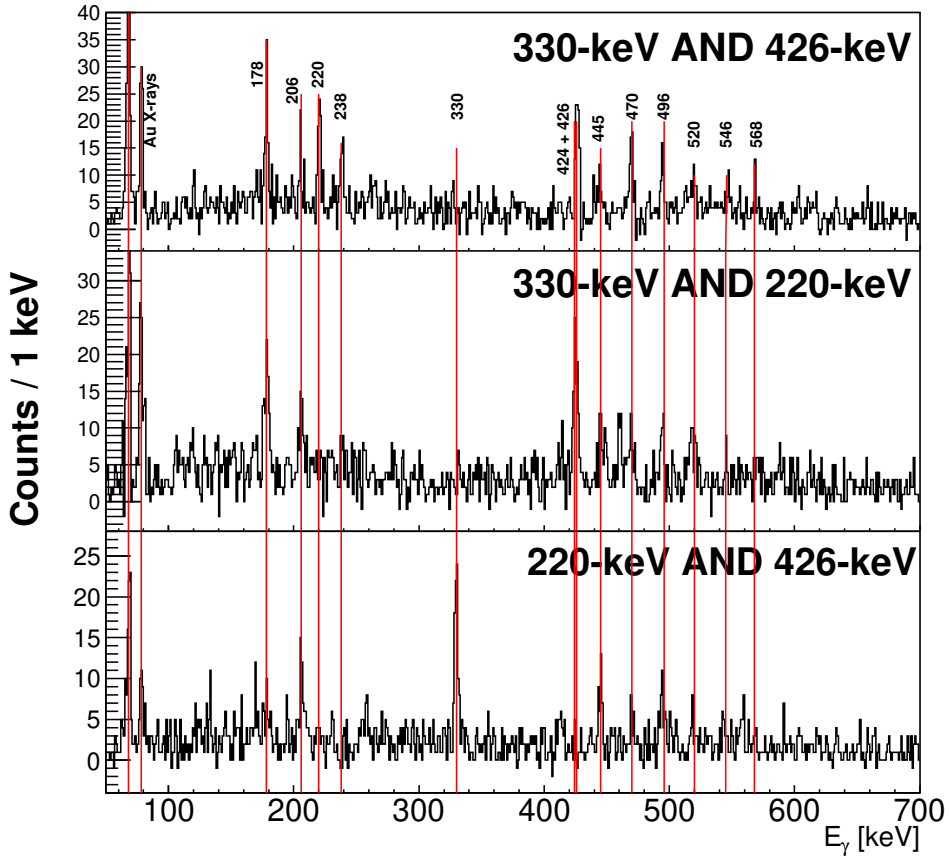

Fig. 5.24 ER-JGII$_{\gamma\gamma\gamma}$ spectrum in coincidence with (a) the 330- AND 426-, (b) the 330- AND 220- and (c) the 220- AND 426-keV transitions.

In the projection gated on the 330- AND 426-keV transitions, the 424-426-keV doublet is again seen as well as some higher energy transitions in band-3(a) and (b) with the 545-, and 568-keV transitions being coincident. The 206- and 238-keV transitions are also observed in all three panels, with these seemingly being inter-band transitions joining band-3(a) and (b). The 206- and 238-keV transitions could not be placed however, as clean ER-JGII$_{\gamma\gamma}$ projections gated on these transitions could not be made. Both the projection gated on the 330- AND 220-keV transitions, and the 220- AND 426-keV transitions clearly show band-3(a) and (b) as well as strong coincidence again seen with the 206-keV transition.

DCO analysis was performed on the 178-, 220-, 330- and 445-keV transitions with values listed in Table 5.3. Other γ rays either had too low intensity in the ER-JGII$_{\gamma\gamma}$ matrix or clean projections could not be produced to perform angular correlations. The DCO values suggest the 220-keV transition is $M1$ in nature and indicate an $E2$ nature for the 178-, 330-, and 445-keV transitions. These values

tentatively establish that the lowest transitions of band-3(a) and (b) are $E2$ with the 220-keV transition being an inter-band $M1$. This suggests that band-3 is also a strongly coupled rotational band similar to band-1 and band-2, however no solid conclusions can be made here due to the less established character of band-3.

Table 5.3 Energies E_γ and relative intensities obtained from JUROGAM II data for γ-ray transitions identified above the 294-ns isomer in Fig. 5.18. Excitation energies E_i are relative to state fed by the 178-keV transition. Angular distribution ratio R_{DCO} (see section 4.6.3), and estimated multipolarities are also listed. Intensities are efficiency corrected and normalised against the 330 keV transition.

E_γ (keV)	I_γ(%)	E_i(keV)	R_{DCO}	Multipolarity
Band-3				
178.1(1)	77(6)	178.1+x	1.48(25)	**(E2)**
220.4(1)	58(7)	1154+x	0.67(22)	**(M1)**
329.9(1)	$\equiv$ 100	508+x	1.53(19)	**(E2)**
425.6(1)	88(5)	933.6+x		
444.7(2)	20(4)	1598.7+x	1.80(22)	**(E2)**
469.6(3)	35(10)	1403.2+x		
495.6(4)	9(3)	2094.3+x		
519.5(3)	35(6)	1922.7+x		
545.1(10)	5(2)	2639.3+x		
567.7(2)	10(3)	2490+x		
Unplaced transitions				
120.7(2)	13(3)			
169.0(3)	31(5)			
195.4(2)	40(6)			
206.2(2)	29(5)			
230.9(3)	1(2)			
238.2(6)	6(4)			
261.2(1)	17(4)			
354.8(2)	22(4)			
505.9(3)	22(4)			
567.7(2)	10(3)			
617.7(11)	3(2)			

5.4 Confirmation of the multipolarity of the 50.2-keV transition

In Sec. 5.2.1 the 50.2-keV transition was assigned mixed $E2/M1$ multipolarity based on $\alpha_{\text{exp,tot}}(50.2) = 19.2(25)$ and on the comparison with theoretical conversion coefficients from BrIcc [59]. This experimental ICC was deduced using γ-ray coincidences between the 50.2-keV and 60.0-keV transitions in the PGD.

In this section the value of $\alpha_{\text{tot, exp}}(50.2)$ is confirmed by the comparison of the number of coincidences for a selected $\gamma\gamma$ pair in the ER-JGII$_{\gamma\gamma}$ matrix and in the same matrix gated by the 50.2-keV γ ray in the PGD. If the selected prompt $\gamma\gamma$ cascade feeds to the isomeric state with no bypassing, then $\alpha_{\text{tot,exp}}$ can be calculated using,

$$\alpha_{\text{tot,exp}}(50.2) = \frac{\text{N(ER-JGII}_{\gamma_1\gamma_2})}{\left(\frac{2^{\frac{\text{ToF}}{t_{1/2}}}}{\varepsilon_{\text{PGD}}(50.2)} \times \text{N(ER} - \text{PGD}_{50.2} - \text{JGII}_{\gamma_1\gamma_2})\right)} - 1, \tag{5.7}$$

where $2^{\frac{\text{ToF}}{t_{1/2}}}$ accounts for the decaying of the 50.2-keV transition, with half-life of 294-ns, during the time-of-flight (ToF) in RITU. A value of ToF=376.3-ns was calculated using the velocity of the recoils, $\beta = 0.0425$, and the RITU length of 4.8-m corresponding to a reduction factor of $2^{376.3/294} \approx 2.42$ for isomeric decays observed by the PGD. The PGD detection efficiency for the 50.2-keV transition ($\varepsilon_{\text{PGD}}(50.2) \approx 22\%$), is taken from GEANT3 simulations of the GREAT spectrometer [51].

As one example of the application of this method, Fig. 5.25 shows the spectra of γ rays in coincidence with the γ_1 = 220-keV transition from band-3 (See Fig. 5.17) in both the IDT and recoil-gated matrices. In both spectra the coincident 178-keV, 330-keV and 426-keV transitions from band-3 are labelled with the integral of these peaks used to deduce $\alpha_{\text{tot,exp}}(50.2)$ shown in Table 5.4. This resulted in an average deduced value of $\alpha_{\text{tot,exp}}(50.2) = 17(4)$, which is consistent to the earlier value of $\alpha_{\text{tot,exp}}(50.2) = 19.3(25)$. This also confirms the assumption made for the application of Eq. 5.7 that band-3 does not bypass the 294-ns isomer. Due to this a dashed line linking the bottom of band-3 to the 294-ns isomer was added in Fig. 5.17.

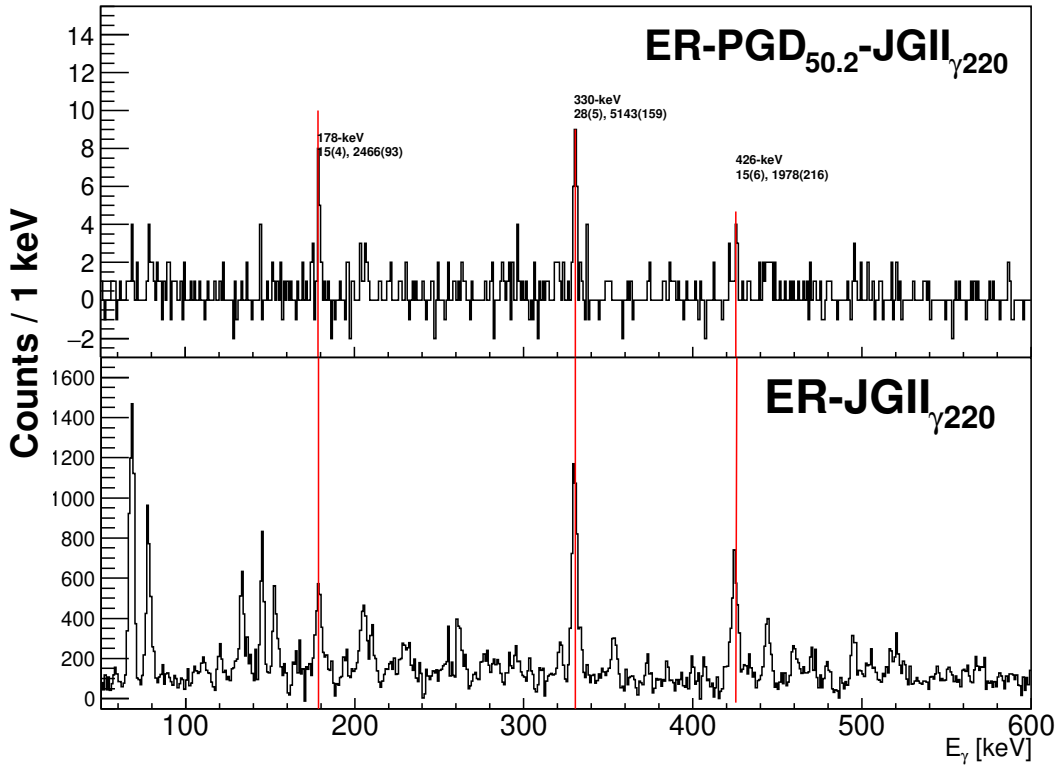

Fig. 5.25 (Bottom): ER-JGII$_{\gamma\gamma}$ matrix projection gated on the 220-keV ($\pm$1.5-keV) transition, (Top): same but additionally gated by the 50.2-keV isomeric decay in the PGD. The peaks are labelled with their energies and integrals from IDT and recoil-gated JGII spectrum respectively.

Table 5.4 $\alpha_{\mathrm{tot,exp}}(50.2)$ deduced using Eq. 5.7 for different $\gamma_1\gamma_2$ pairs. The 19.3(25)* references the value deduced in section 5.2.1 from coincidences observed in the PGD.

E_{γ_1}-E_{γ_2} (keV)	N(ER-JGII$_{\gamma_1\gamma_2}$)	N(ER-PGD(50.2)-JGII$_{\gamma_1\gamma_2}$)	$\alpha_{\mathrm{tot,\,exp}}$
			19.3(25)*
178 - 220	2466(93)	15(4)	16(4)
330 - 220	4502(159)	28(5)	16(3)
426 - 220	3077(216)	15(4)	20(5)
Sum	10045(468)	58(13)	17(4)

5.5 Multipolarity of the 56.7-keV isomeric transition, and proving the existence of bypass of the 373-ns isomer by band-1

Previously the 56.7-keV isomeric transition was tentatively assigned multipolarity $E2$, based on $\alpha_{\text{tot, exp}} = 40(12)$ [27] and from comparison to theoretical values of $\alpha_{\text{tot, th}}(E2) = 68.1$ and $\alpha_{\text{tot,th}}(M1) = 6.811$ [59]. In this work the same method as applied to the 50.2-keV γ ray was also used to deduce $\alpha_{\text{tot,exp}}(56.7)$ resulting in a multipolarity of either $E1$ or $M1$ depending on the amount of the de-excitation path bypassing the 373-ns isomer. This result was used to check the method used in [27] and to confirm that band-1 bypasses the 373-ns isomer.

Modifying Eq. 5.7 to be used for the 56.7-keV transition gives,

$$\alpha_{\text{tot,exp}}(56.7) = \frac{\text{N(ER-JGII}_{\gamma_1\gamma_2})}{\left(\frac{2^{\frac{\text{ToF}}{T_{1/2}}}}{\varepsilon_{\text{PGD}}(56.7)} \times \text{N(ER} - \text{PGD}_{56.7} - \text{JGII}_{\gamma_1\gamma_2})\right)} - 1, \tag{5.8}$$

where the ToF reduction factor is $2^{376.3/373} \approx 2$ for the 56.7-keV transition and the PGD efficiency is $\varepsilon_{\text{PGD}}(56.7) \approx 25\%$ [51]. It is important to stress that Eqn. 5.8 requires that the selected $\gamma_1\gamma_2$ cascade fully feeds to the tagged 56.7-keV isomeric transitions with no bypassing.

It should be noted however, that there is a large difference in the intensities of band-1 and band-2 in the recoil-gated and IDT JUROGAM-II spectra. Whilst the intensities of both bands are similar in the IDT spectra (See Fig. 5.8), band-1 is seen with much higher statistics in the recoil-gated spectra than band-2 (See Fig. 5.10). This suggests that band-1 is more strongly populated in the fusion evaporation reaction than band-2, but the reduction in relative intensity seen in the PGD-gated spectrum can be explained by **band-1 strongly bypassing the tagged 373-ns isomeric state**.

If the selected $\gamma_1\gamma_2$ coincidence has a strong decay path that bypasses the 373-ns isomeric state then this results in an apparent reduction in the intensity for transitions in the γ-ray spectra gated on the 56.7-keV transition. This means the deduced $\alpha_{\text{tot,exp}}$ value from Eq. 5.8 (with no bypass) will always be greater than the true internal conversion coefficient ($\alpha_{\text{tot, true}}$, which includes bypass) such that,

$$\alpha_{\text{tot,true}} = \alpha_{\text{tot,exp}} - \text{I}_{\text{bypass}}(1 + \alpha_{\text{tot,exp}}) \tag{5.9}$$

Here it can be seen that the case of no bypassing ($\text{I}_{\text{bypass}} = 0\%$) results in $\alpha_{\text{tot,true}} = \alpha_{\text{tot,exp}}$. For this reason when interpreting the $\alpha_{\text{tot,exp}}(56.7)$ value we should consider that there must be strong bypassing of the 56.7-keV isomeric state by band-1 which will result in an increase in the measured

value as will be discussed later.

First, starting with the direct application of Eqn. 5.8, the 143-keV, ($M1$) transition in band-1 (See Fig 5.9) was selected as γ_1. This transition provided clean projections for both the recoil-gated and IDT $\gamma\gamma$ matrices as shown in Fig. 5.26.

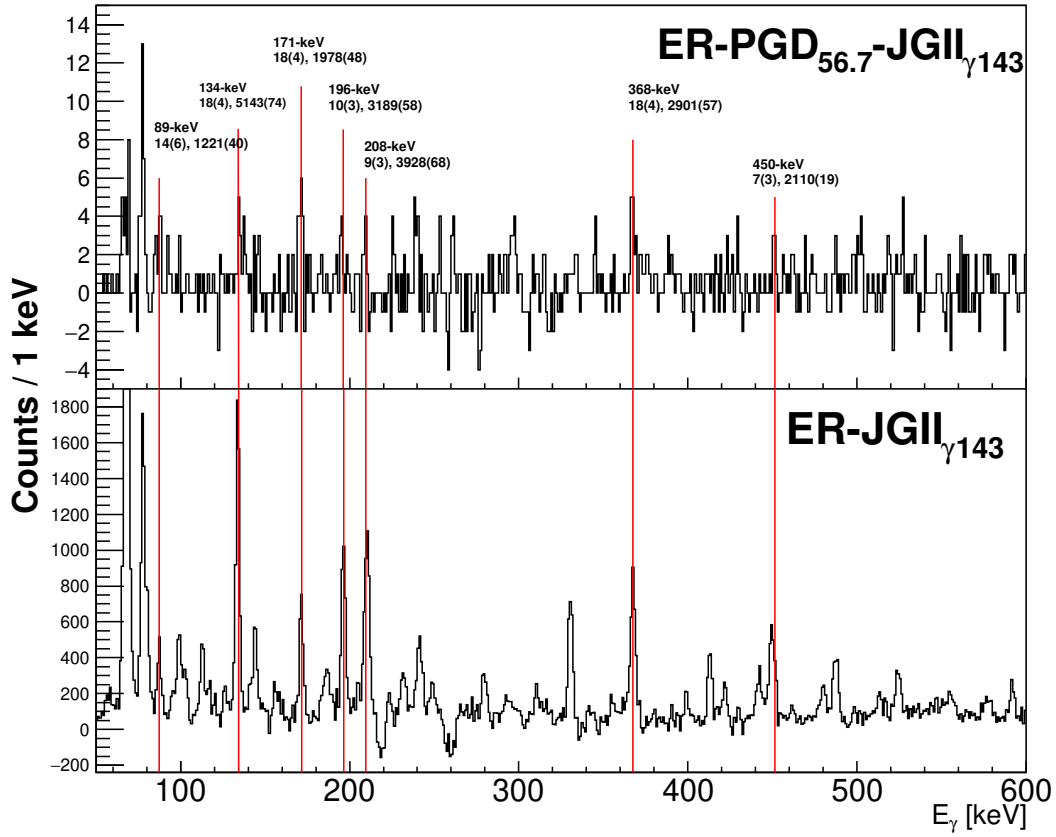

Fig. 5.26 (Bottom): ER-JGII$_{\gamma\gamma}$ matrix projection gated on the 143-keV ($\pm$1.5-keV) transition, (Top): same but additionally gated by the 56.7-keV isomeric decay in the PGD. The peaks are labelled with their energies and integrals from IDT and recoil-gated JGII spectrum respectively.

Several coincident transitions from band-1 such as the 134-, 171- and 196-keV transitions among others, were used to deduce $\alpha_{\text{tot,exp}}(56.7)$. This resulted in several values listed in Table 5.5 with an average value of $\alpha_{\text{tot,exp}}(56.7) = 24(6)$. This value gives an upper limit for the α_{tot} as bypassing is not yet considered. It should be noted that this value is within 2σ from the previously deduced value

of 40(2) [27], which confirms the previous result.

Table 5.5 $\alpha_{\text{tot,exp}}(56.7)$ deduced using Eq. 5.8 for different $\gamma_1\gamma_2$ pairs.

E_γ-E_γ (keV)	N(ER-JGII$_{\gamma\gamma}$)	N(ER-PGD$_\gamma$-JGII$_{\gamma\gamma}$)	$\alpha_{tot,exp}$
88 - 143	1221(40)	14(4)	10(3)
134 - 143	5143(74)	18(4)	35(8)
171 - 143	1978(48)	18(4)	14(4)
196 - 143	3189(58)	10(3)	39(12)
368 - 143	2901(57)	18(4)	19(5)
450 - 143	2110(49)	7(3)	36(14)
Sum	16524(326)	85(22)	24(6)

The theoretical ICC from BrIcc for the 56.7-keV are $\alpha_{\text{tot, th}}(E1) = 0.386$, $\alpha_{\text{tot,th}}(M1) = 6.811$ and $\alpha_{\text{tot, th}}(E2) = 68.1$. Comparing the measured and theoretical values rules out a pure $E2$ assignment and instead indicates a $E1$, $M1$ or mixed $E2/M1$ multipolarity.

As the next step, the possibility of the decay of band-1 bypassing the 373-ns isomer is considered. Eq. 5.9 was used substituting $\alpha_{\text{tot,th}}$ for $\alpha_{\text{tot,true}}$ to estimate the bypassing intensity. Table 5.6 shows the calculated bypass intensity assuming a pure $E1$, $M1$, or $E2$ multipolarity for the 56.7-keV transition. Firstly, an $E2$ multipolarity results in a negative bypassing intensity and thus $E2$ is ruled out in agreement with the inference previously made. A pure $M1$ or $E1$ multipolarity however result in bypassing intensities of 69% and 95% respectively.

Table 5.6 $\alpha_{\text{tot,th}}$ for the 56.7-keV transition [59]. I_{bypass} calculated with Eq. 5.9 for each multipolarity using the $\alpha_{\text{tot,exp}} = 24(6)$ and $\alpha_{\text{tot,true}} = \alpha_{\text{tot,th}}$. The transition strength is also calculated for each multipolarity.

Multipolarity	$\alpha_{\text{tot,th}}$	B(L) W.u	I_{bypass}
$E1$	0.386(7)	$2.27(4) \times 10^{-5}$	95%
$M1$	6.811(12)	$4.14(8) \times 10^{-5}$	69%
$E2$	68.1(16)	0.63(2)	-176%

As the method is highly dependent on the bypassing intensity above mentioned, the result of $\alpha_{\text{tot,exp}} = 24(6)$ should only be considered as an upper limit. Therefore a different method will be described below which further constricts the upper limit of $\alpha_{\text{tot,exp}}$.

Calculated by the relative number of 56-7-keV and 50.2-keV transitions.

A value of $\alpha_{\text{tot,exp}}(56.7) = 6(2)$ was deduced in [1], by a distinct method and was also repeated in this work. This value was calculated by comparison of the number of 56.7-keV transitions seen in the ER-PGD$_\gamma$ spectrum and the total number of ^{178}Au$^{\text{m}}$ nuclei produced.

The total amount of ^{178}Au$^{\text{m}}$ produced was estimated by complex analysis of the α-decay spectrum shown in Fig. 5.2(a). Firstly the number of 5950-keV ^{175}Pt α-decays contributing to the 5950-, 5977-keV peak was subtracted by means of α-gamma analysis using the $\alpha(5964) - \gamma(77)$ coincidence with $b_\alpha(^{175}\text{Pt}) = 55\%$ [58] to calculate the number of ^{177}Ir produced.

Secondly, a component of the 5925-keV α-decay of ^{178}Au$^{\text{m}}$ contributes to the 5977-keV peak. This is because the 5925-keV α decay feeds to the daughter ^{174}Ir$^{\text{m}}$ via a 56.8-keV transition as shown in Fig. 5.1. The 56.8-keV M1 decay in ^{174}Ir is strongly converted (α_{tot} = 6.8) resulting in L and M conversion electrons with energies 42.5- and 53.4-keV. The summing of energies in the DSSD results in an artificial peak at 5977-keV and an apparent reduction in the intensity for the 5925-keV α-decay.

The α + CE summing effect is dependent on the depth in the DSSD in which the recoiling nuclei are implanted, therefore GEANT4 simulations [62] were used to estimate the implantation depth in the DSSD from recoils and the respective $\alpha + e^-$ summing. The estimate of the implantation depth was used to estimate a production ratio of $\frac{^{178}\text{Au}^{\text{m}}}{^{178}\text{Au}^{\text{g}}} = 1.2(2)$.

The 50.2- and 56.7-keV isomeric decays of ^{178}Au observed in the ER-PGD$_\gamma$ spectrum (see Fig. 5.3, N(50.2) = 22742(151), and N(56.7) = 173801(417)) were then compared. These values were corrected for the loss of intensity during the ToF through RITU =$2^{\frac{\text{ToF}}{t_{1/2}}}$ and for the efficiency for the detection efficiency of the PGD (ε_γ(PGD) $\approx 25\%$). This gave a ratio of the decays N(56.7)/N(50.2) = 5.07(32). The difference in the intensity of the 50.2-keV and 56.7-keV γ rays is a result of the difference in production of ^{178}Au$^{\text{m}}/^{178}$Au$^{\text{g}}$ = 1.2(2), and difference in the internal conversions of both isomeric decays.

As $\alpha_{\text{tot, exp}}(50.2) = 19.4(2)$ is known from analysis in Sec. 5.2.1, and the production ratio of both α-decaying states is estimated (=1.2(2)), it can be shown that $\alpha_{\text{tot,exp}}(56.7) = \frac{19.4}{(5.07/1.2)} = 4.6(11)$. This value is within the uncertainty of the previous value, $\alpha_{\text{tot,exp}} = 6(2)$, clearly rules out an $E2$ assignment, but would be consistent with a pure $M1$ multipolarity ($\alpha_{\text{tot,th}} = 6.81$).

As we can not confirm that the α-decaying state ^{178}Au$^{\text{m}}$ is fully fed by the 373-ns isomer, the measured $\alpha_{\text{tot,exp}}(56.7)$ value gives an upper limit which substitutes for the calculated $\alpha_{\text{tot, exp}}(56.7) = 24(6)$. Therefore the measured $\alpha_{\text{tot, exp}}(56.7) = 4.6(11)$ does not rule out an $E1$ transition if excited states feed directly to the α-decaying state bypassing the 373-ns isomer. Therefore the possibility of both $E1$ or $M1$ multipolarity for the 56.7-keV transition will be discussed in Chapter 6.

Chapter 6

Discussion

6.1 373-ns isomer

The two rotational bands, band-1 and band-2, identified above the 373-ns isomer were tentatively assigned configurations based on analogy with neighbouring Ir isotopes (See Fig. 5.9). These bands also aided in the understanding of the 56.7-keV isomeric transition which was discussed in Sec. 5.5.

Band-1 - $\pi i_{13/2} \otimes \nu i_{13/2}$

Band-1 was assigned the $\pi 1/2^+[660] \otimes \nu 7/2^+[633]$ configuration based on analogy with neighbouring odd-odd isotopes ^{176,178,180}Ir and ^{182}Au, in particular with the isotonic ^{176}Ir in which several bands are known [2]. The specific Nilsson orbitals originate from the $\pi i_{13/2}$ and $\nu i_{13/2}$ spherical orbitals respectively. The comparison between band-1 and this band in ^{176}Ir is shown in Fig. 5.9 where the energies and positions of transitions in both bands match extremely closely. The strong population of band-1 when compared to other bands observed in ^{178}Au suggests that band-1 is yrast at high spins. Fig. 6.1(a) shows the total aligned angular momentum (I_x, see Eqn. 2.2.2) plotted against the rotational frequency ($\hbar\omega$, see Eqn. 2.22), for band-1 and the $\pi 1/2^+[660] \otimes \nu 7/2^+[633]$ bands in ^{176}Ir and ^{178}Ir in which extremely high consistency is seen between all 3 bands.

As with the same bands in ^{176,178}Ir, the $K = 4^+$ bandhead was not observed. In ^{176}Ir this was explained by the band's intensity being lost to several other positive parity bands below [2]. In the case of ^{178}Au, it may be also that the band loses intensity to some other unidentified bands, or that lower transitions sit below the 373-ns isomer and as such were not identified during the analysis.

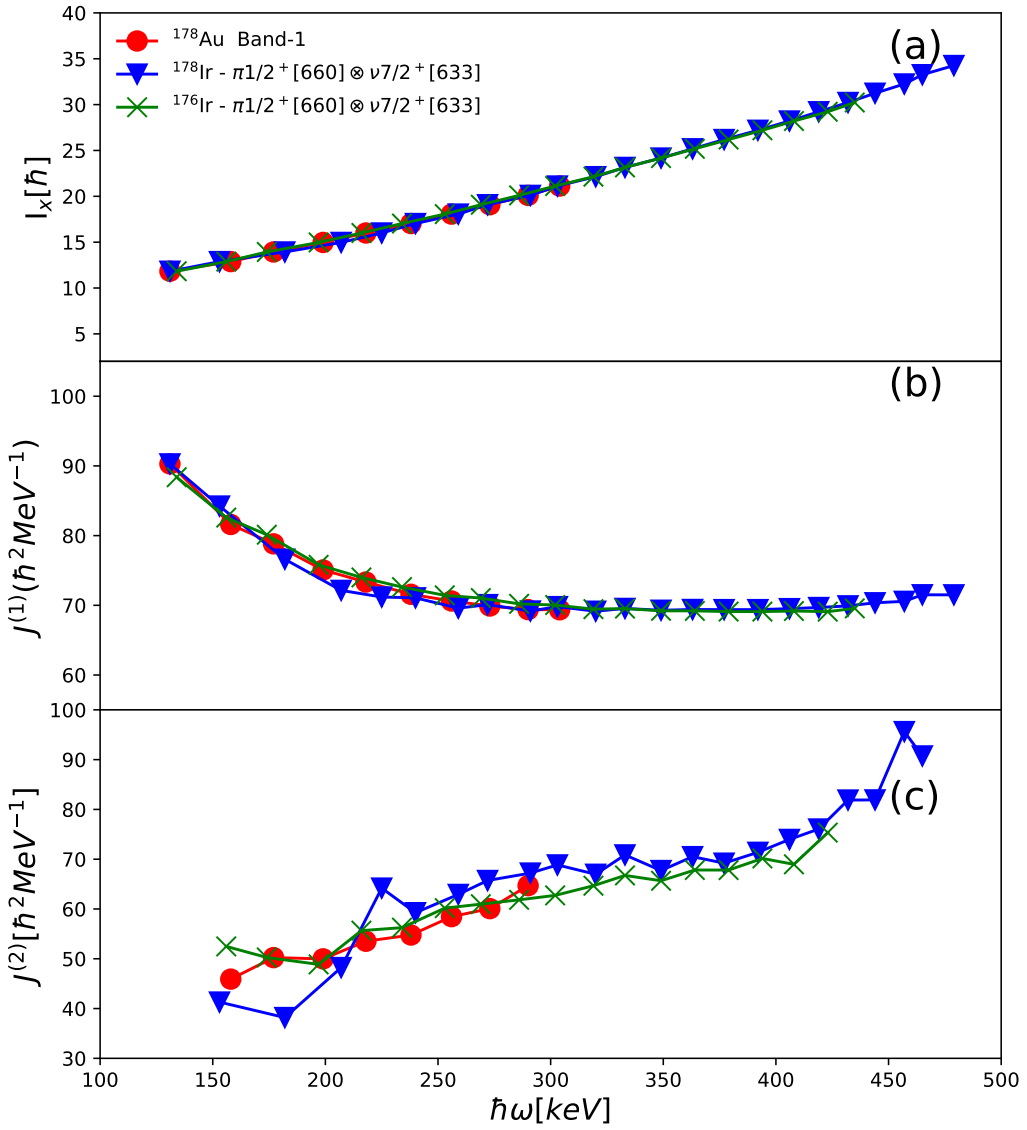

Fig. 6.1 (a) Total aligned angular momentum (I_x), (b) kinematic moment of inertia ($\Im^{(1)}$), and (c) dynamic moment of inertia ($\Im^{(2)}$) as a function of the rotational frequency ($\hbar\omega$), for band-1 in ^{178}Au and the $\pi i_{13/2} \otimes \nu i_{13/2}$ bands in ^{176,178}Ir.

The nuclear moments of inertia $\Im^{(1)}$ and $\Im^{(2)}$ for band-1 are shown Fig. 6.1(b) and (c) respectively, again with strong agreement with the $\pi i_{13/2} \otimes \nu i_{13/2}$ bands in neighbouring nuclei. A high kinematical moment of inertia $\Im^{(1)} \approx 70\ \hbar^2\text{MeV}^{-1}$ is seen at high rotational frequency ($\hbar\omega > 200$-keV) suggesting stronger deformation when compared to band-2 which is discussed later. As with neighbouring Ir isotopes, the strong Coriolis effect in the $\pi i_{13/2}$ and $\nu i_{13/2}$ orbitals causes a high compression in the lower energy states and therefore an increase in the $\Im^{(1)}$ values at low rotational frequencies [2]. The dynamic moment of inertia $\Im^{(2)}$ shows a slight increase in both Ir isotopes suggesting a slight increase in deformation with rotational frequency, however higher spin states of band-1 were not identified, meaning this trend can not be established for ^{178}Au.

The nature of band-1 is also confirmed by its staggering parameter S(I). As band-1 consists of an I=even and I=odd band, one signature will be favoured with this expressed by the staggering parameter,

$$S(I) = E(I+1) - [E(I+2) + E(I-2)]/2, \tag{6.1}$$

where E is the excitation energy of the state with angular momentum I. The staggering quantifies the energy difference between both signatures of the band and plotted against the angular momentum is shown in Fig. 6.2, along with the $\pi i_{13/2} \otimes \nu i_{13/2}$ bands in ^{176,178}Ir and ^{182}Au. Signature inversion is observed along the entire spin range of band-1 with a $\alpha = 0$ signature favoured. In ^{182}Au the inversion is seen to revert to a favoured $\alpha = 1$ signature at $I = 22$ [4], whilst for ^{178}Ir this reversal is seen at a higher angular momentum of $I = 25.5$. For band-1 of ^{178}Au, the highest observed state was $I = (23^+)$ meaning that whilst low spin signature inversion is observed, a favoured $\alpha = 1$ signature may occur at higher spins.

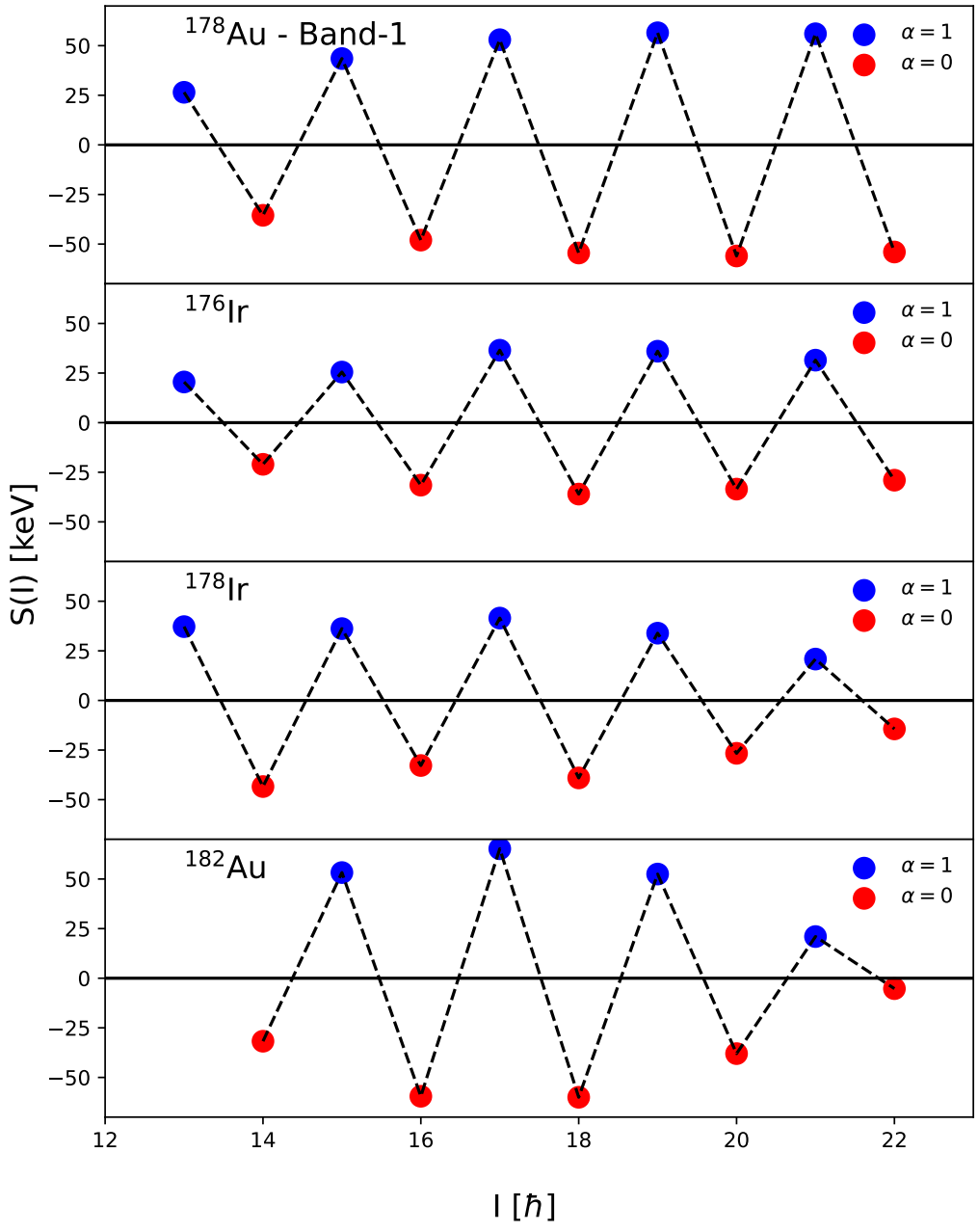

Fig. 6.2 Staggering parameter, S(I), for band-1 in ^{178}Au, and the $\pi i_{13/2} \otimes \nu i_{13/2}$ band in ^{176,178}Pt [2, 3] and ^{182}Au [4].

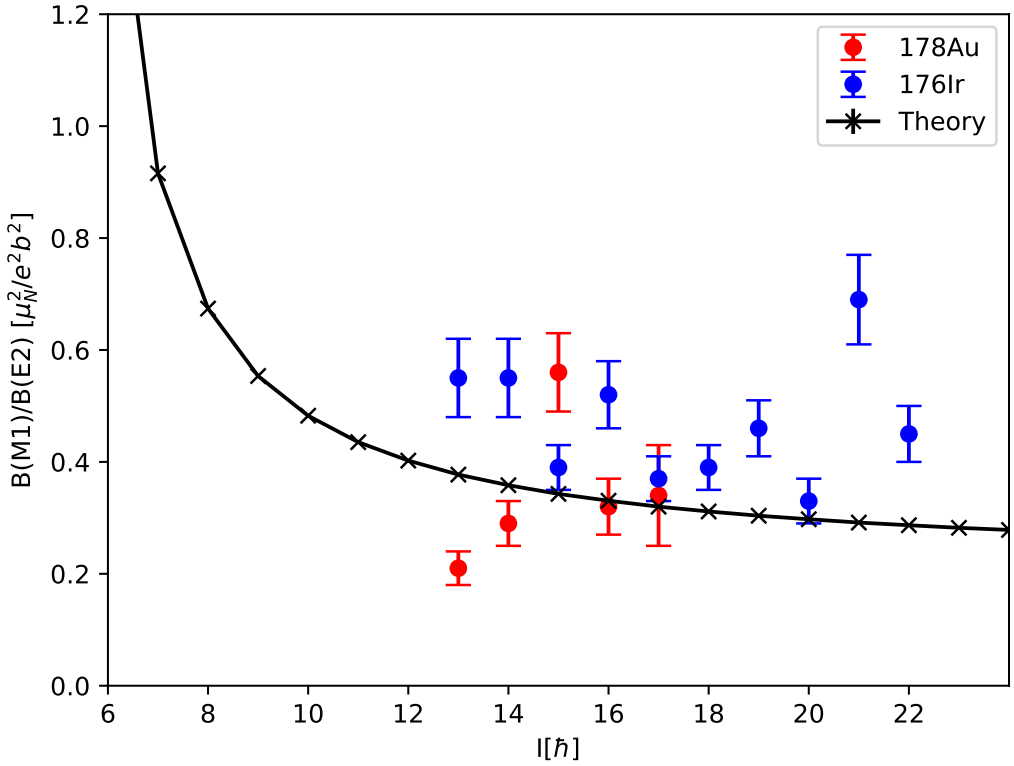

Fig. 6.3 Comparison of the B(M1)/B(E2) ratios for band-1 and the $\pi 1/2^+[660] \otimes \nu 7/2^+[633]$ band in ^{176}Ir. Theoretical values were calculated using the **bm1be2** code [5] using parameters, $\pi 1/2^+[660] - (i = 4.58, g_\Omega = 1.35) \otimes \nu 7/2^+[633] - (i = -3.45, g_\Omega = -0.26)$.

B(M1)/B(E2) ratios

Using the experimental data for band-1 it was possible to extract the ratio between the reduced probabilities of $M1$ and $E2$ transitions from the same state. This was done by using the energies ($E_\gamma(M1,E2)$) and intensities ($I_\gamma(M1,E2)$) of the $M1$ and $E2$ transitions from each state in band-1 given in Tab. 5.2. The ratio of reduced transition probabilities is expressed as,

$$\frac{B(M1;I \to I-1)}{B(E2;I \to I-2)} = 0.697 \frac{[E_\gamma(E2;I \to I-2)]^5}{[E_\gamma(M1;I \to I-1)]^3} \frac{I_\gamma(M1)}{I_\gamma(E2)} [(\mu_N/eb)^2] + \delta(E2/M1), \tag{6.2}$$

where I_γ is the intensity of each γ-ray transition with energy E_γ (in MeV) from the state with total angular momentum I and each transition is assumed to be a stretched transition such that $\delta(E2/M1) = 0$. Since the $B(M1)/B(E2)$ ratios are sensitive to the configuration of the band, this can be a helpful tool to identify the correct configuration for a given band.

Figure 6.3 shows the $B(M1)/B(E2)$ ratios for band-1 and the $\pi 1/2^+[660] \otimes \nu 7/2^+[633]$ band in ^{176}Ir with the ratios consistent between both nuclei. Detailed calculations of the $B(M1)/B(E2)$ ratio using the semi-classic formula of the cranking model developed by Dönau and Frauendorf [63], were previously compared to the experimental ratios in both ^{176}Ir and ^{178}Ir to establish the $\pi i_{13/2} \otimes \nu i_{13/2}$ bands [2, 64]. This calculation was recreated and shown in black using the the **bm1be2** FORTRAN code [5], utilising the same parameters adjusted for ^{178}Au, $\pi 1/2^+[660] - (i = 4.58, g_\Omega = 1.35) \otimes \nu 7/2^+[633] - (i = -3.45, g_\Omega = -0.26)$.

Band-2 - $\pi h_{11/2} \otimes \nu f_{7/2}$

Band-2 (See Fig. 5.9) is assigned as the $\pi 9/2^-[514] \otimes \nu 5/2^-[512]$ configuration based on analogy to the neighbouring ^{178}Ir and isotonic ^{176}Ir. This specific Nilsson orbitals originate from the $\pi h_{11/2}$ and $\nu f 7/2$ spherical orbitals. The $\pi 9/2^-[514] \otimes \nu 5/2^-[512]$ band in ^{176}Ir is shown for comparison in Fig. 5.9 with the energy of transitions being clearly similar to that of band-2.

The total aligned angular momentum of band-2 is shown in Fig. 6.4(a) compared with the $\pi 9/2^-[514] \otimes \nu 5/2^-[512]$ bands in ^{176,178}Ir with strong agreement between the three nuclei. Due to the construction of band-2 being limited, with only up to the $I = (16^+)$ state being observed, the alignment plot covers a much smaller rotational frequency range than that of the Ir neighbours shown.

The assignment of band-2 is also supported by the nuclear moments of inertia shown in Fig. 6.4(b) and (c), again showing strong agreement with neighbouring nuclei. Contrary to the $\nu i_{13/2}$ orbital in band-1, there is far less Coriolis compression associated with the $\nu f_{7/2}$ orbital in band-2 and therefore a slight increase is seen in $\Im^{(1)}$ value with rotational frequency is observed in both Ir isotopes. This trend cannot be established in ^{178}Au however as a much lower angular frequency range is shown.

The reduced kinematical moment of $\Im^{(1)} \approx 60\ \hbar^2\text{MeV}^{-1}$ compared to band-1 in which $\Im^{(1)} \approx 70$ suggests that band-1 is more deformed than band-2. The dynamic moment of inertia $\Im^{(2)} \approx 60\hbar^2\text{MeV}^{-1}$ is seen to gradual increase with rotational frequency similarly to neighbouring Ir isotopes.

The $K = 7^+$ bandhead of the $\pi 9/2^-[514] \otimes 5/2^-[512]$ band was observed in ^{176}Ir (see figure 5.9), ^{178}Ir and ^{182}Au, however was not seen in band-2. This is likely a consequence of the IDT technique used to construct band-2. As the tagged 56.7-keV transition decays from the 373-ns isomer to the α-decaying state ^{178}Au$^{\text{m}}$, it may be that the bandhead sits between the α-decaying state and the 246-keV 373-ns isomer (See Fig. 5.9). This could be confirmed if clean recoil decay tagging was possible, in which case the $9^+ \rightarrow 7^+ \approx 320$-keV transition would be observed in correlation with the

α-decays from ^{178}Au^{m}, however the RDT cannot be used in this case as previously discussed.

In the ISOLDE study [16], ^{178}Au^{m} was tentatively assigned $I^{\pi} = (7^{+})$ or (8^{-}) based on the β-decay feeding pattern to states in the daughter, ^{178}Pt. For the $I^{\pi} = 7^{+}$ assignment, the $\pi 9/2^{-}[514] \otimes 5/2^{-}[512]$ configuration was suggested based on the coupling of angular momentum and agreement seen between the expected and experimental magnetic dipole moments.

As band-2 is assigned the $\pi 9/2^{-}[514] \otimes 5/2^{-}[512]$ configuration with $K = 7^{+}$, this may rule out the $I^{\pi} = 7^{+}$ assignment for the alpha-decaying state ^{178}Au^{m}. This is because a 7^{+} state would require the same $\pi 9/2^{-}[514] \otimes 5/2^{-}[512]$ configuration as band-2 and results in ^{178}Au^{m} being the bandhead. If we disregard this possibility then this would result in a $I^{\pi} = 8^{-}$ ^{178}Au^{m}, however as the configuration of band-2 only is tentative this cannot be confirmed. The Nilsson orbitals associated with a spherical ground-state as well band-1 and band-2 are shown in Fig. 6.5.

The relative intensities of band-1 and 2 in the recoil-gated and IDT JGII γ-ray spectrum suggests that band-1 has a high probability of de-excitation that bypasses the 373-ns isomer. High bypass intensity of band-1 would be explained by the bandhead de-exciting either to an unknown isomer of ^{178}Au or directly feeding to the alpha-decaying state ^{178}Au^{m}. Without clean recoil decay tagging available however, it is not possible to confirm this explanation.

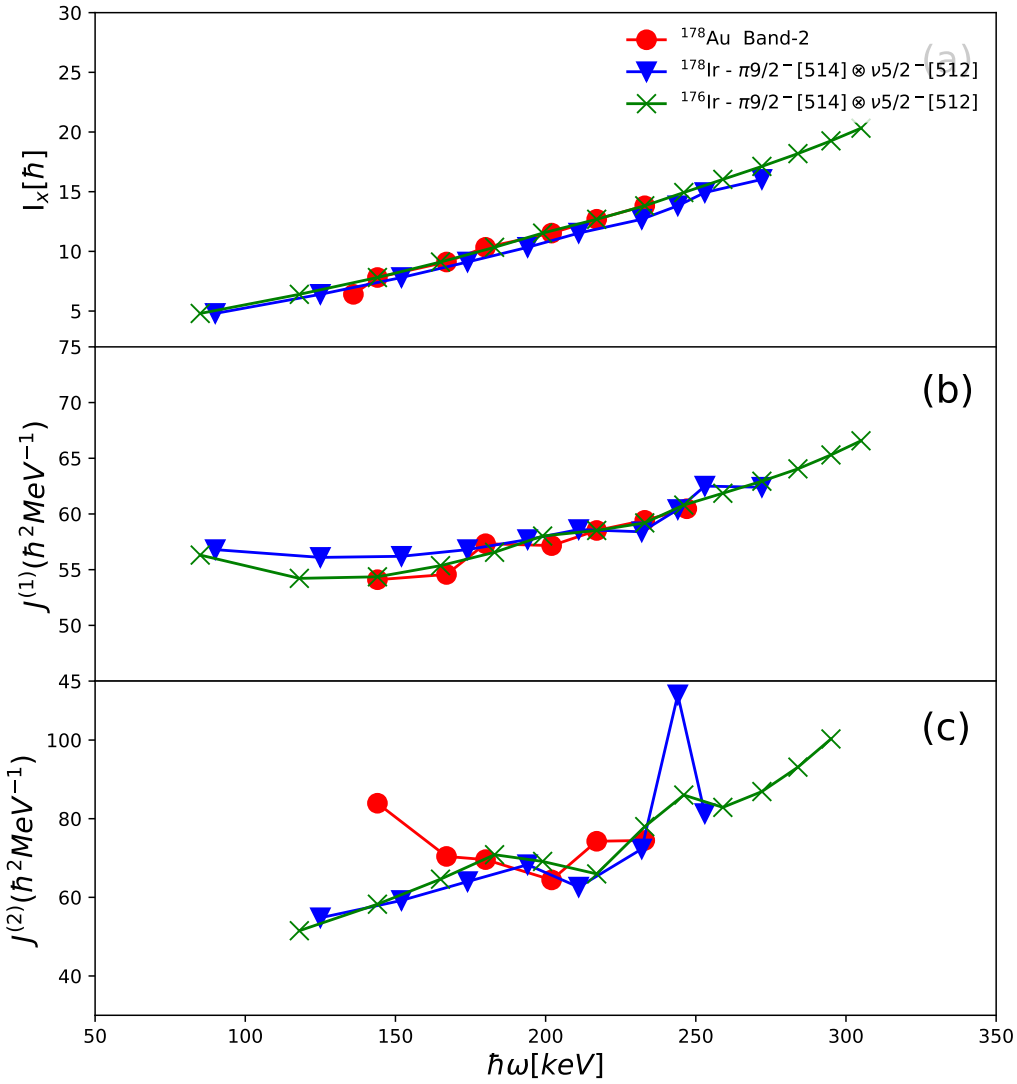

Fig. 6.4 (a) Total aligned angular momentum (I_x), (b) kinematic moment of inertia ($\mathfrak{I}^{(1)}$) and (c) dynamic moment of inertia ($\mathfrak{I}^{(2)}$) as a function of the rotational frequency ($\hbar\omega$), for band-2 in ^{178}Au and the $\pi 9/2^-[514] \otimes \nu 5/2^-[512]$ band in ^{176,178}Ir.

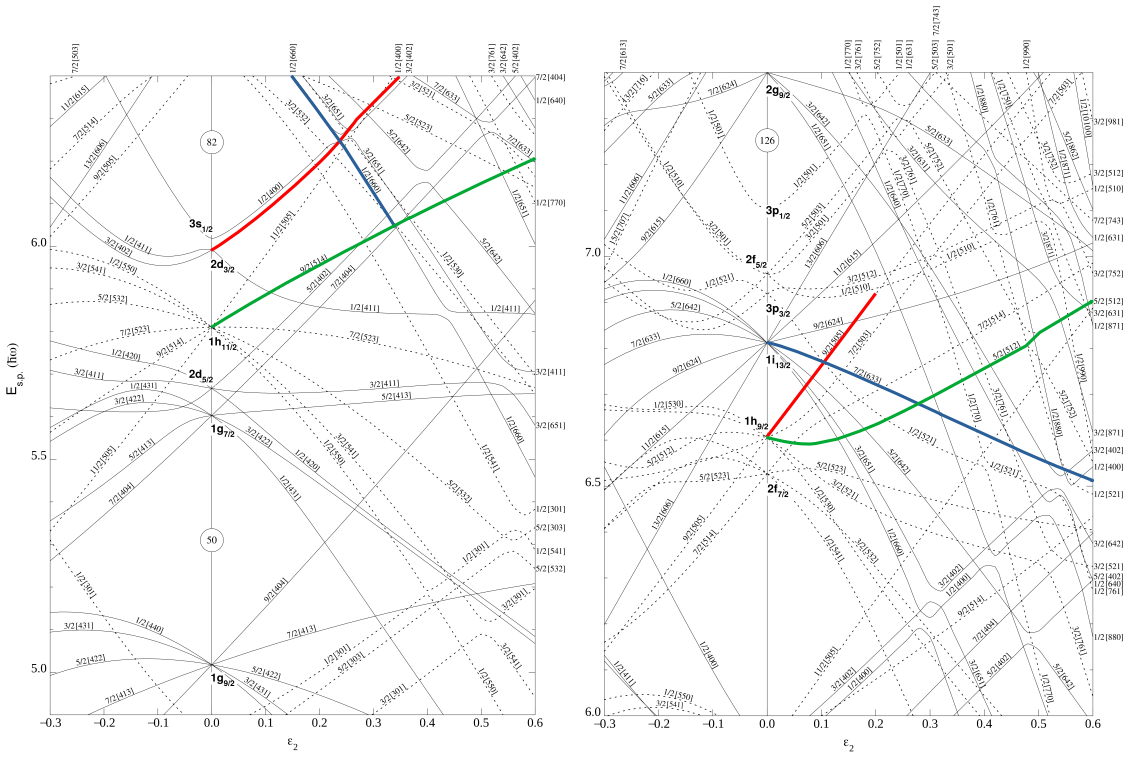

Fig. 6.5 Nilsson diagrams for proton (left) and neutron orbitals (right). The orbitals associated with the spherical shape, band-1 and band-2 are indicated with red, blue and green lines respectively. Figure adapted from [6].

56.7-keV isomeric transition

In this thesis an upper limit $\alpha_{\text{tot,exp}}(56.7) = 4.6(11)$ was deduced, which clearly rules out a pure $E2$ multipolarity assignment. This means the multipolarity of the 56.7-keV transition must be either $E1$ or $M1$, with each of these possibilities resulting in a unique interpretation for the 373-ns state.

Firstly if the transition has multipolarity $E1$, this would naturally explain its isomeric character. This is because the resulting reduced transition probability B($E1$, 56.7-keV) = 2.3×10^{-6} W.u would be typical of the hindrance seen in other low-energy $E1$ decays in this region of nuclei. For example, in the neighbouring odd-even ^{179}Au, two $E1$ transitions, with energies 62.4-keV and 89.5-keV, were observed decaying from a 328-ns isomer [21]. These transitions had reduced transition probabilities of B($E1$, 62.4-keV) = $1.88(1) \times 10^{-6}$ W.u, and B($E1$, 89.5-keV) = $5.3(2) \times 10^{-8}$ W.u similar to that estimated for an $E1$ 56.7-keV transition in ^{178}Au. For an $E1$ multipolarity to be justified 95% bypassing between band-1 and the 373-ns isomer would be needed.

A pure $M1$ multipolarity meanwhile would suggest strong hindrance with B($M1, 56.7$) = $4.6(15) \times 10^{-5}$ W.u. Several strongly hindered $M1$ decays are seen in ^{185,187,189}Au, for the $11/2^- \rightarrow 9/2^-$ transition [65], with these transitions having slightly shorter 26-190 ns half-lives and similar energies to the 56.7-keV transition. As $\alpha_{\text{tot,exp}}(56.7) = 4.6(11)$ is an upper limit, it seems very unlikely that the 56.7-keV transition is $M1$ $\alpha_{\text{tot, th}}(56.7) = 6.811$.

From the previous ISOLDE study, the alpha-decaying state ^{178}Au$^{\text{m}}$ is assigned spin-parity I^{π}=($7^+, 8^-$). This coupled with assumption that the 56.7-keV decay has a multipolarity of $E1$, results in 4 possible spin-parities for the 373-ns state ($I^{\pi} = 6^-, 8^-$ or $7^+, 9^+$). The positive spin-parity assignments would match closely with the lowest observed (9^+) and (8^+) states for bands-1 and 2 respectively which may rule out $I = 7^+$ assignment for ^{178}Au$^{\text{m}}$.

The tentative spin assignment of both band-1 and band-2 gives the lowest lying observed state of each band I^{π}(band-1) = (9^+) and I^{π}(band-2) = (8^+) with each band known to feed to the 373-ns isomer and places both bands only $\Delta I = 2$ or 1 from ^{178}Au$^{\text{m}}$. For this reason the 373-ns isomer is either directly fed by a transition in one of the bands, or by some unseen highly converted or low-energy transitions.

6.2 294-ns isomer

Whilst 50.2-keV, 60.0-keV, 63.4-keV and 113.4-keV transitions (See Fig. 6.6) are associated with the decay of the 294-ns isomer above the ground-state, ^{178}Au$^{\text{g}}$, only some of these will originate directly from the de-excitation of the isomeric state. The other transitions are prompt following the decay of the isomer with their *apparent* half-life influenced by the half-live of the isomer. To inform which γ ray is isomeric, the transitions strengths of each were considered based on their assigned multipolarities.

The 50.2-keV, 60.0-keV, and 63.4-keV transitions were all assigned mixed $M1/E2$ multipolarity based on their measured internal conversion coefficients (See Tab. 5.4). From Weisskopf estimates, transitions with energies in the range of 50 - 60 keV are expected to have half-lives of $\approx 10^{-11}$ to 10^{-10} s for pure $M1$ and several hundred nanoseconds for pure $E2$ multipolarity or a mixed $M1/E2$ transition with a strong $E2$ component. This means that a possible explanation for the 294-ns isomer is that the transition has $E2$ multipolarity. The 63.4-keV decay proves to be a good candidate for this situation, as is seen by its mixing ratio $\delta^2 E2/M1)[63.4] = 0.97(15)$, much higher than for the other transitions, $\delta^2(E2/M1)[50.2] = 0.55(7)$ and $\delta^2(E2/M1)[60.0] = 0.58(5)$. Furthermore the 63.4-keV γ ray has a calculated transition strength of B($E2$, 63.4)=0.63(10), nearly twice higher compared with B($E2, 50.2$) = 0.39 and B($E2, 60.0$) = 0.37. Therefore because of the strong $E2$ nature, the 294-ns

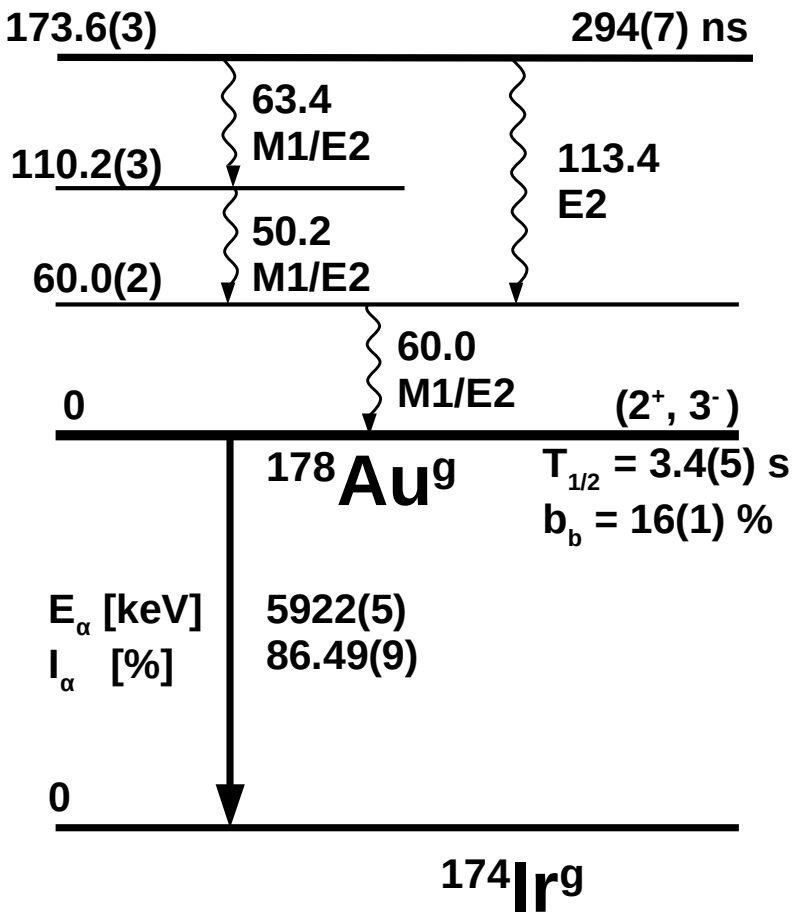

Fig. 6.6 Proposed decay scheme for the 294-ns isomer.

isomeric state is considered to likely decay by the 63.4-keV transition followed by prompt 50.2-keV and 60.0-keV γ rays as shown in Fig. 6.6. This ordering is fixed by the 113.4-keV γ ray observed in coincidence with the 60.0-keV transition.

The spin-parity of the 294-ns state is constrained using knowledge of the 50.0-keV, 60.0-keV, and 63.4-keV cascade which feeds to the ground state. The configuration of ^{178}Au^{g} was previously dis-

cussed to be either the $\pi 1/2^-[541] \otimes \nu 5/2^-[512](I^\pi = 2^+)$, or $\pi 1/2^-[541] \otimes \nu 7/2^+[633](I^\pi = 3^-)$ with this prediction made by comparison of the expected and experimental magnetic moments [16]. These two possible spin-parities $I = (2^+, 3^-)$, make it more complex to establish the spin-parity of the 294-ns isomer. This is because the angular momenta coupling for the ground state and transitions results in a number of possible I^π values for the isomer. As the 63.4-keV, 50.2-keV and 60.0-keV transitions all have mixed $M1/E2$ multipolarity, the 294-ns isomer must have angular momentum $I^\pi = (1^+, 3^+, 5^+)$ or $I^\pi = (0^-, 2^-, 4^-, 6^-)$ for a 2^+ or 3^- ground state respectively. If the difference in the angular momentum between the 294-ns isomer and the ground state was $\Delta I = 1$ or 2, then a direct decay would be expected resulting in the observation of a 173.6-keV $M1$ or $E2$ transition observed in the PGD. With no such transition observed the $I^\pi = (1^+, 3^+)$ and $(2^-, 4^-)$ assignments are disregarded. For this reason the 294-ns isomer most likely has spin-parity $I^\pi = (0^-, 5^+, 6^-)$, however no speculation on a tentative value will be made.

A dedicated β-decay study of ^{178}Au was performed in 2021 at the ISOLDE Decay Station (IDS). This experiment collected orders of magnitude higher statistics than the study described in [14, 16]. These data will hopefully help to establish the true spin/parities of both α-decaying states, and in turn may help to further clarify decay scheme.

6.3 Production cross sections

The fusion-evaporation cross sections for the ^{88}Sr + ^{92}Mo $\rightarrow ^{180}$Hg* reaction used during the experiment were derived. This estimate was completed by measuring the number of α decays seen in the DSSD recoil-α spectrum. The number of counts in the strongest α decay peak for each isotope was corrected for the known α-branching ratio (b_α) and relative alpha intensity. The value was then corrected for the full α-particle energy detection efficiency of the DSSD ($\varepsilon_{\mathrm{DSSD}} = 50(5)\%$) and the recoil transmission efficiency of RITU ($\sim 40\%$). After corrections, the number of α decays from each isotope corresponded to the number of nuclei produced at the target position r_x. This was used to calculate the experimental cross section (σ_x), dependent on the beam delivered on target Φ and the target density ρ_x.

$$\sigma_x = \frac{r_x}{\Phi \rho_x} \tag{6.3}$$

where the beam delivered to the target is calculated from the average beam current (I_x) of 6-npA and a total run time of 6 days (518400 seconds).

$$\Phi = I_x \times t = 6\mathrm{pnA} \times 518400 = \mathbf{1.944 \times 10^{16} particles} \tag{6.4}$$

The target density ρ_x, was calculated using the molar mass of the ^{92}Mo target (91.91 g/mol) and the known 600μg/cm^2 thickness,

$$\rho_x = (600\mu\text{g/cm}^2)/(91.91\text{g/mol}) \times \text{N}_{\text{Av}} = \mathbf{3.93 \times 10^{18} cm^2} \tag{6.5}$$

where N_{Av} is Avagadro's constant. The calculated experimental cross sections are shown in Table 6.1 and are compared with HIVAP calculations [45]. As Pt isotopes were produced both in the fusion evaporation reaction and by the decays of both Hg and Au isotopes after implantation in the DSSD they were not considered in this analysis.

Table 6.1 Estimated cross-section, σ_{exp} of Au, and Hg isotopes compared with calculations from the HIVAP code (σ_{HIVAP}).

	b_α [%]	N(ER-α)	r_x	σ_{exp} [mb]	σ_{HIVAP} [mb]
^{176}Au					3.51×10^{-5}
^{177}Au	59.7*	$5.25(4) \times 10^5$	$4.51(3) \times 10^6$	0.059(12)	0.536
^{178}Au	13.8*	$4.61(3) \times 10^5$	$1.66(12) \times 10^7$	0.218(44)	0.590
^{179}Au					0.15
^{177}Hg	85				0.184
^{178}Hg	70	$5.07(3) \times 10^5$	$3.62(3) \times 10^6$	0.047(9)	0.862
^{179}Hg	55	$5.06(9) \times 10^4$	$4.60(8) \times 10^5$	0.006(1)	0.005

HIVAP calculations use several adjustable parameters to estimate the production of fusion evaporation products. Crucially of these was a scaling parameter for liquid drop model component of the fission barrier (BARFAC), where a value of 0.69 was used. With this value, some agreement is seen in the production cross section of ^{178}Au, however other nuclei such as ^{178}Hg are seen with much lower cross sections than calculated. With more rigorous and accurate cross section measurements along with further utilisation of the HIVAP code it is possible that an estimate for the fission barrier of ^{180}Hg could be made.

Chapter 7

Summary

This thesis presents the results from studies of the neutron deficient, odd-odd nucleus ^{178}Au performed at JYFL Accelerator Laboratory at the University of Jyväskylä. ^{178}Au nuclei were produced by means of ^{92}Mo(^{88}Sr,np)^{178}Au, fusion evaporation reaction. The JUROGAM II γ-ray was used in combination with the RITU separator and the GREAT spectrometer, allowing for excited states of ^{178}Au to be studied.

The decay schemes for two sub-μs isomers of ^{178}Au with half-lives 294(7)- and 373(9)-ns were established, with these built on top of the α-decaying states ^{178}Au^{g,m}. Possible explanations for the nature of these isomers were discussed, however the exact nature of the 373-ns isomer could not be determined.

Knowledge of sub-μs isomeric states of ^{178}Au allowed for the isomer decay tagging technique to be utilised to identify prompt γ-ray transitions. Analysis of $\gamma\gamma$ coincidences in the JUROGAM-II array established two rotational bands above the 373-ns isomer and one band above the 294-ns isomer (Shown in Fig. 7.1). Band-1 and 2 were tentatively assigned the $\pi 1/2^+[660] \otimes \nu 7/2^+[633]$ and $\pi 9/2^-[514] \otimes \nu 5/2^-[512]$ configurations respectively based on analogy with structures identified in several neighbouring odd-odd isotopes.

One aim of this study was to identify the $\pi i_{13/2} \otimes \nu i_{13/2}$ band, to which band-1 was assigned. As seen in neighbouring odd-odd nuclei, this band exhibited signature inversion over the entire established spin range. Unfortunately as the $K = 4^+$ state in band-1 could not be established, the energy of the bandhead is not known.

The RDT technique could not be used to identify prompt transitions in ^{178}Au, due to the high recoil rate, low α-branching and relatively long half-lives (2.7-3.4s) of the alpha decaying states of ^{178}Au. For this reason transitions which feed directly to the α-decaying states bypassing the 294- and

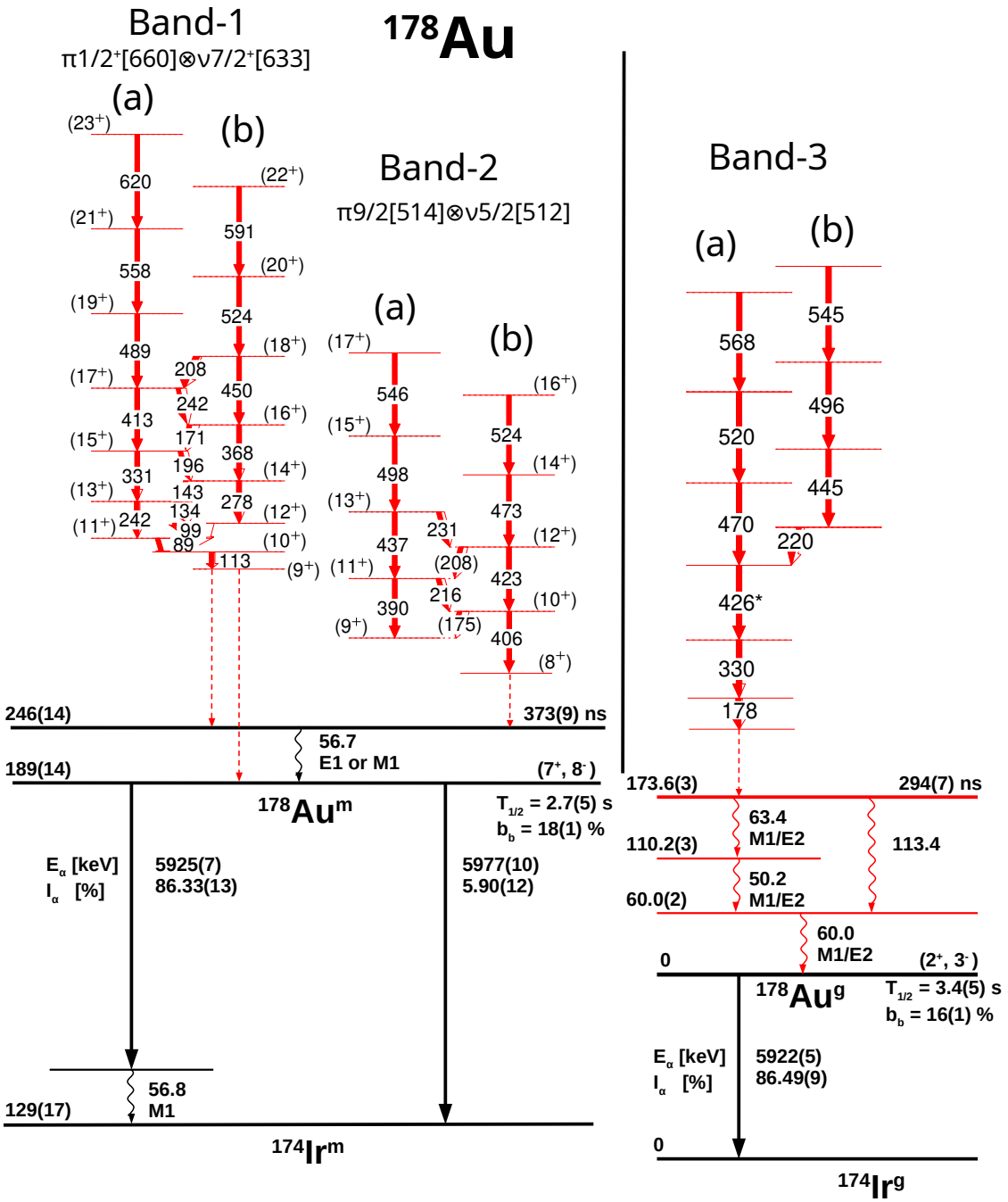

Fig. 7.1 Bands 1, 2, and 3 and the structure of the 294-ns isomer identified in this work are marked in red. The 373-ns isomer and the α-decaying states identified in [27] and [16] respectively are marked in black.

373-ns isomers could not be identified. A future experiment utilising more segmented DSSD's would allow the RDT technique to be effectively employed for nuclei with longer half-lives such as ^{178}Au. This could lead to an increased efficiency over the IDT technique, and allow for the identification of prompt transitions which bypass the 373- and 294-ns isomers. Such studies would also allow for additional bands in ^{178}Au to be establish and further the understanding of both α-decaying states.

Looking to the future, a β-decay study of ^{178}Hg will be performed using the IDS experiment at ISOLDE [66]. This will provide additional information about the low-energy excitations in the daughter nucleus, ^{178}Au. Analysis of a dedicated β-decay study of ^{178}Au performed at ISOLDE in August 2021 is still ongoing. These new data may firmly establish the spin/parity of both α-decaying states, which could allow outstanding questions to be answered, especially on the sub-μs isomers and their link to the newly established rotational bands.

Finally, a previous ISOLDE study established that ^{180}Au is strongly deformed however no level scheme is currently established for this nucleus, therefore an in-beam study of ^{180}Au would also be desirable in order to identify the $\pi i_{13/2} \otimes \nu i_{13/2}$ band.

References

[1] S. A. Gillespie, A. Stott, A. N. Andreyev, J. G. Cubiss, M. Al Monthery, C. J. Barton, S. Antalic, K. Auranen, H. Badran, D. Cox, T. Grahn, P. T. Greenlees, A. Herzan, E. Higgins, R. Julin, S. Juutinen, J. Klimo, J. Konki, M. Leino, M. Mallaburn, J. Pakarinen, P. Papadakis, J. Partanen, P. M. Prajapati, P. Rahkila, M. Sandzelius, C. Scholey, J. Sorri, S. Stolze, R. Urban, J. Uusitalo, M. Venhart, and F. Wearing. Identification of sub-μs isomeric states in the odd-odd nucleus ^{178}Au. *Phys. Rev. C*, 103:044307, Apr 2021.

[2] R. A. Bark, A. M. Baxter, A. P. Byrne, P. M. Davidson, G. D. Dracoulis, S. M. Mullins, T. R. McGoram, and R. T. Newman. Two-quasiparticle configurations, signature inversion, and the $\pi i_{13/2} \bigotimes \nu i_{13/2}$ band in ^{176}Ir. *Phys. Rev. C*, 67:014320, Jan 2003.

[3] Zhang Yu-Hu, T. Hayakawa, M. Oshima, Y. Toh, J. Katakura, Y. Hatsukawa, M. Matsuda, N. Shinohara, T. Ishii, H. Kusakari, M. Sugawara, T. Komatsubara, and K. Furuno. Search for signature inversion in the $\pi i_{13/2} \otimes \nu i_{13/2}$ band in odd-odd ^{178}Ir. *Chinese Physics Letters*, 18(10):1323–1326, oct 2001.

[4] Yuhu Zhang, Furong Xu, Jianjun He, Zhong Liu, Xiaohong Zhou, Zaiguo Gan, M. Oshima, T. Hayakawa, Y. Toh, T. Shizuma, J. Katakura, Y. Hatsukawa, M. Matsuda, H. Kusakari, M. Sugawara, K. Furuno, T. Komatsubara, T. Une, Shuxian Wen, and Zhimin Wang. High-spin states and signature inversion in odd-odd ^{182}Au. *Science in China Series G: Physics, Mechanics and Astronomy*, 46(4):382–389, Aug 2003.

[5] E. S Paul. personal communication.

[6] R.B. Firestone. *The 8th edition of the Table of Isotopes*. Wiley-InterScience, 1997.

[7] L. P. Gaffney, P. A. Butler, M. Scheck, A. B. Hayes, F. Wenander, M. Albers, B. Bastin, C. Bauer, A. Blazhev, S. Bönig, N. Bree, J. Cederkäll, T. Chupp, D. Cline, T. E. Cocolios, T. Davinson, H. De Witte, J. Diriken, T. Grahn, A. Herzan, M. Huyse, D. G. Jenkins, D. T. Joss, N. Kesteloot, J. Konki, M. Kowalczyk, Th. Kröll, E. Kwan, R. Lutter, K. Moschner, P. Napiorkowski, J. Pakarinen, M. Pfeiffer, D. Radeck, P. Reiter, K. Reynders, S. V. Rigby, L. M. Robledo, M. Rudigier, S. Sambi, M. Seidlitz, B. Siebeck, T. Stora, P. Thoele, P. Van Duppen, M. J. Vermeulen, M. von Schmid, D. Voulot, N. Warr, K. Wimmer, K. Wrzosek-Lipska, C. Y. Wu, and M. Zielinska. Studies of pear-shaped nuclei using accelerated radioactive beams. *Nature*, 497(7448):199–204, May 2013.

[8] P. Möller, A.J. Sierk, T. Ichikawa, and H. Sagawa. Nuclear ground-state masses and deformations: Frdm(2012). *Atomic Data and Nuclear Data Tables*, 109-110:1–204, 2016.

[9] H. Morinaga. Interpretation of some of the excited states of 4*n* self-conjugate nuclei. *Phys. Rev.*, 101:254–258, Jan 1956.

[10] NNDC Evaluated Nuclear Structure Data File (ENSDF), Accessed on Monday 3rd July, 2023.

[11] Kris Heyde and John L. Wood. Shape coexistence in atomic nuclei. *Rev. Mod. Phys.*, 83:1467–1521, Nov 2011.

[12] A. N. Andreyev, M. Huyse, P. Van Duppen, L. Weissman, D. Ackermann, J. Gerl, F. P. Hessberger, S. Hofmann, A. Kleinböhl, G. Münzenberg, S. Reshitko, C. Schlegel, H. Schaffner, P. Cagarda, M. Matos, S. Saro, A. Keenan, C. Moore, C. D. O'Leary, R. D. Page, M. Taylor, H. Kettunen, M. Leino, A. Lavrentiev, R. Wyss, and K. Heyde. A triplet of differently shaped spin-zero states in the atomic nucleus ^{186}Pb. *Nature*, 405(6785):430–433, May 2000.

[13] D. Little, A. D. Ayangeakaa, R. V. F. Janssens, S. Zhu, Y. Tsunoda, T. Otsuka, B. A. Brown, M. P. Carpenter, A. Gade, D. Rhodes, C. R. Hoffman, F. G. Kondev, T. Lauritsen, D. Seweryniak, J. Wu, J. Henderson, C. Y. Wu, P. Chowdhury, P. C. Bender, A. M. Forney, and W. B. Walters. Multistep coulomb excitation of ^{64}Ni: Shape coexistence and nature of low-spin excitations. *Phys. Rev. C*, 106:044313, Oct 2022.

[14] J.G. Cubiss *et al. In. Preparation*.

[15] B. A. Marsh, T. Day Goodacre, S. Sels, Y. Tsunoda, B. Andel, A. N. Andreyev, N. A. Althubiti, D. Atanasov, A. E. Barzakh, J. Billowes, K. Blaum, T. E. Cocolios, J. G. Cubiss, J. Dobaczewski, G. J. Farooq-Smith, D. V. Fedorov, V. N. Fedosseev, K. T. Flanagan, L. P. Gaffney, L. Ghys, M. Huyse, S. Kreim, D. Lunney, K. M. Lynch, V. Manea, Y. Martinez Palenzuela, P. L. Molkanov, T. Otsuka, A. Pastore, M. Rosenbusch, R. E. Rossel, S. Rothe, L. Schweikhard, M. D. Seliverstov, P. Spagnoletti, C. Van Beveren, P. Van Duppen, M. Veinhard, E. Verstraelen, A. Welker, K. Wendt, F. Wienholtz, R. N. Wolf, A. Zadvornaya, and K. Zuber. Characterization of the shape-staggering effect in mercury nuclei. *Nature Physics*, 14(12):1163–1167, Dec 2018.

[16] J. G. Cubiss, A. N. Andreyev, A. E. Barzakh, V. Manea, M. Al Monthery, N. A. Althubiti, B. Andel, S. Antalic, D. Atanasov, K. Blaum, T. E. Cocolios, T. Day Goodacre, A. de Roubin, G. J. Farooq-Smith, D. V. Fedorov, V. N. Fedosseev, D. A. Fink, L. P. Gaffney, L. Ghys, R. D. Harding, F. Herfurth, M. Huyse, N. Imai, D. T. Joss, S. Kreim, D. Lunney, K. M. Lynch, B. A. Marsh, Y. Martinez Palenzuela, P. L. Molkanov, D. Neidherr, G. G. O'Neill, R. D. Page, M. Rosenbusch, R. E. Rossel, S. Rothe, L. Schweikhard, M. D. Seliverstov, S. Sels, A. Stott, C. Van Beveren, P. Van Duppen, E. Verstraelen, A. Welker, F. Wienholtz, R. N. Wolf, and K. Zuber. Laser-assisted decay spectroscopy and mass spectrometry of ^{178}Au. *Phys. Rev. C*, 102:044332, Oct 2020.

[17] Antti Siivola. Alpha-active gold isotopes. *Nuclear Physics A*, 109(1):231–235, 1968.

[18] Céline Van Beveren, AN Andreyev, AE Barzakh, Thomas Elias Cocolios, RP De Groote, D Fedorov, VN Fedosseev, R Ferrer, Lars Ghys, Mark Huyse, et al. α-decay study of Tl. *Journal of Physics G: Nuclear and Particle Physics*, 43(2):025102, 2016.

[19] B. Andel, A. N. Andreyev, S. Antalic, A. Barzakh, N. Bree, T. E. Cocolios, V. F. Comas, J. Diriken, J. Elseviers, D. V. Fedorov, V. N. Fedosseev, S. Franchoo, L. Ghys, J. A. Heredia, M. Huyse, O. Ivanov, U. Köster, V. Liberati, B. A. Marsh, K. Nishio, R. D. Page, N. Patronis, M. D. Seliverstov, I. Tsekhanovich, P. Van den Bergh, J. Van De Walle, P. Van Duppen, M. Venhart, S. Vermote, M. Veselský, and C. Wagemans. Detailed α-decay study of ^{180}Tl. *Phys. Rev. C*, 96:054327, Nov 2017.

[20] M. Venhart, M. Balogh, A. Herzáň, J.L. Wood, F.A. Ali, D.T. Joss, A.N. Andreyev, K. Auranen, R.J. Carroll, M.C. Drummond, J.L. Easton, P.T. Greenlees, T. Grahn, A. Gredley, J. Henderson, U. Jakobsson, R. Julin, S. Juutinen, J. Konki, E.A. Lawrie, M. Leino, V. Matoušek, C.G. McPeake, D. O'Donnell, R.D. Page, J. Pakarinen, P. Papadakis, J. Partanen, P. Peura, P. Rahkila,

P. Ruotsalainen, M. Sandzelius, J. Sarén, B. Saygı, M. Sedlák, C. Scholey, J. Sorri, S. Stolze, A. Thornthwaite, R. Urban, J. Uusitalo, M. Veselský, and F.P. Wearing. Population of a low-spin positive-parity band from high-spin intruder states in ^{177}Au: The two-state mixing effect. *Physics Letters B*, 806:135488, 2020.

[21] Martin Venhart, A.N. Andreyev, John Wood, Stanislav Antalic, L. Bianco, P.T. Greenlees, Ulrika Jakobsson, Pete Jones, R. Julin, S. Juutinen, Steffen Ketelhut, and M. Leino. Shape coexistence in odd-mass au isotopes: Determination of the excitation energy of the lowest intruder state in 179au. *Physics Letters B - PHYS LETT B*, 695:82–87, 01 2011.

[22] Tuck-Meng Goon. *"Alpha and Gamma-ray Spectroscopic Studies of Au, Pt, and Ir Nuclei Near the Proton Dripline"*. PhD thesis, 2004.

[23] W. F. Mueller, H. Q. Jin, J. M. Lewis, W. Reviol, L. L. Riedinger, M. P. Carpenter, C. Baktash, J. D. Garrett, N. R. Johnson, I. Y. Lee, F. K. McGowan, C. H. Yu, and S. Cwiok. High-spin structure in ^{181,183}Au. *Phys. Rev. C*, 59:2009–2032, Apr 1999.

[24] R.A. Bark, H. Carlsson, S.J. Freeman, G.B. Hagemann, F. Ingebretsen, H.J. Jensen, T. Lönnroth, M.J. Piiparinen, I. Ragnarsson, H. Ryde, H. Schnack-Petersen, P.B. Semmes, and P.O. Tjøm. Band structures and proton-neutron interactions in ^{174}Ta. *Nuclear Physics A*, 630(3):603–630, 1998.

[25] Y. H. Zhang, M. Oshima, Y. Toh, M. Koizumi, A. Osa, T. Shizuma, T. Hayakawa, M. Sugawara, H. Kusakari, T. Morikawa, S. X. Wen, and L. H. Zhu. Rotational bands and signature inversion phenomena in $\pi h_{9/2}\nu i_{13/2}$ and $\pi i_{13/2} \otimes \nu i_{13/2}$ structures in odd-odd ^{176}Ir. *The European Physical Journal A - Hadrons and Nuclei*, 13(4):429–433, Apr 2002.

[26] Y. H. Zhang, Y. D. Fang, G. de Angelis, N. Marginean, A. Gadea, D. R. Napoli, M. Axiotis, C. Rusu, T. Martinez, H. L. Wang, X. H. Zhou, W. T. Guo, M. L. Liu, Y. X. Guo, X. G. Lei, M. Oshima, and Y. Toh. Properties of the $\pi i_{13/2} \otimes \nu i_{13/2}$ band in odd-odd ^{184}Au. *Phys. Rev. C*, 70:057303, Nov 2004.

[27] Monther Hamed AL-Monthery. *"Decay Studies of ^{178}Au and Its Daughter ^{174}Ir"*. PhD thesis, 2019.

[28] E. Rutherford F.R.S. The scattering of α and β particles by matter and the structure of the atom. *The London, Edinburgh, and Dublin Philosophical Magazine and Journal of Science*, 21(125):669–688, 1911.

[29] C. F. v. Weizsäcker. Zur theorie der kernmassen. *Zeitschrift für Physik*, 96(7):431–458, Jul 1935.

[30] Roger D. Woods and David S. Saxon. Diffuse surface optical model for nucleon-nuclei scattering. *Phys. Rev.*, 95:577–578, Jul 1954.

[31] Maria Goeppert Mayer. Nuclear configurations in the spin-orbit coupling model. i. empirical evidence. *Phys. Rev.*, 78:16–21, Apr 1950.

[32] S. G. Nilsson. Binding states of individual nucleons in strongly deformed nuclei. *Kong. Dan. Vid. Sel. Mat. Fys. Med.*, 29N16:1–69, 1955.

[33] Benjamin Roy Mottelson and Sven Gösta Nilsson. Classification of the nucleonic states in deformed nuclei. *Physical Review*, 99(5):1615, 1955.

[34] Tord Bengtsson and Ingemar Ragnarsson. Rotational bands and particle-hole excitations at very high spin. *Nuclear Physics A*, 436(1):14–82, 1985.

[35] A. Bohr and B R Mottelson. Single-particle and collective aspects of nuclear rotation. *Phys. Scr*, 24:1B, Jul 1981.

[36] Samuel M. Harris. Higher order corrections to the cranking model. *Phys. Rev.*, 138:B509–B513, May 1965.

[37] R. Bengtsson and S. Frauendorf. Quasiparticle spectra near the yrast line. *Nuclear Physics A*, 327(1):139–171, 1979.

[38] G. Gamow. The quantum theory of nuclear disintegration. *Nature*, 122(3082):805–806, Nov 1928.

[39] Ronald W. Gurney and Edw. U. Condon. Wave mechanics and radioactive disintegration. *Nature*, 122(3073):439–439, Sep 1928.

[40] E. Segre and E. Segrè. *Nuclei and Particles: An Introduction to Nuclear and Subnuclear Physics*. W.A. Benjamin, 1964.

[41] P. Van Duppen and M. Huyse. Shape coexistence around the z=82 closed shell probed by α-decay. *Hyperfine Interactions*, 129(1):149–161, Dec 2000.

[42] V. F. Weisskopf. Radiative transition probabilities in nuclei. *Phys. Rev.*, 83:1073–1073, Sep 1951.

[43] Alexander Michael Thornthwaite. *"Structure of the neutron-deficient nuclei ^{173}Au and ^{173}Pt and their α-decay descendants"*. PhD thesis, 2014.

[44] Kalle Auranen. *"Spectroscopy of ^{199,201}At"*. *Research report/Department of Physics*. PhD thesis, 2015.

[45] W. Reisdorf. Analysis of fissionability data at high excitation energies. *Zeitschrift für Physik A Atoms and Nuclei*, 300(2):227–238, Jun 1981.

[46] P. Heikkinen and E. Liukkonen. K130 Cyclotron - The First Years of Full Operation. In *14th International Conference on Cyclotrons and Their Applications*, page B08, 8 1996.

[47] G. Duchêne, F.A. Beck, P.J. Twin, G. de France, D. Curien, L. Han, C.W. Beausang, M.A. Bentley, P.J. Nolan, and J. Simpson. The clover: a new generation of composite ge detectors. *Nuclear Instruments and Methods in Physics Research Section A: Accelerators, Spectrometers, Detectors and Associated Equipment*, 432(1):90–110, 1999.

[48] C.W. Beausang, S.A. Forbes, P. Fallon, P.J. Nolan, P.J. Twin, J.N. Mo, J.C. Lisle, M.A. Bentley, J. Simpson, F.A. Beck, D. Curien, G. deFrance, G. Duchêne, and D. Popescu. Measurements on prototype ge and bgo detectors for the eurogam array. *Nuclear Instruments and Methods in Physics Research Section A: Accelerators, Spectrometers, Detectors and Associated Equipment*, 313(1):37–49, 1992.

[49] M Leino, J Äystö, T Enqvist, P Heikkinen, A Jokinen, M Nurmia, A Ostrowski, W.H Trzaska, J Uusitalo, K Eskola, P Armbruster, and V Ninov. Gas-filled recoil separator for studies of heavy elements. *Nuclear Instruments and Methods in Physics Research Section B: Beam Interactions with Materials and Atoms*, 99(1):653–656, 1995. Application of Accelerators in Research and Industry '94.

[50] R.D. Page, A.N. Andreyev, D.E. Appelbe, P.A. Butler, S.J. Freeman, P.T. Greenlees, R.-D. Herzberg, D.G. Jenkins, G.D. Jones, P. Jones, D.T. Joss, R. Julin, H. Kettunen, M. Leino, P. Rahkila, P.H. Regan, J. Simpson, J. Uusitalo, S.M. Vincent, and R. Wadsworth. The great spectrometer. *Nuclear Instruments and Methods in Physics Research Section B: Beam Interactions with Materials and Atoms*, 204:634–637, 2003. 14th International Conference on Electromagnetic Isotope Separators and Techniques Related to their Applications.

[51] A.N. Andreyev, P.A. Butler, R.D. Page, D.E. Appelbe, G.D. Jones, D.T. Joss, R.-D. Herzberg, P.H. Regan, J. Simpson, and R. Wadsworth. Geant monte carlo simulations for the great spectrometer. *Nuclear Instruments and Methods in Physics Research Section A: Accelerators, Spectrometers, Detectors and Associated Equipment*, 533(3):422–434, 2004.

[52] I. Lazarus, E.E. Appelbe, P.A. Butler, P.j. Coleman-Smith, J.R. Cresswell, S.J. Freeman, R.D. Herzberg, I. Hibbert, D.T. Joss, S.C. Letts, R.D. Page, V.F.E. Pucknell, P.H. Regan, J. Sampson, J. Simpson, J. Thornhill, and R. Wadsworth. The great triggerless total data readout method. *IEEE Transactions on Nuclear Science*, 48(3):567–569, 2001.

[53] K.S. Krane, R.M. Steffen, and R.M. Wheeler. Directional correlations of gamma radiations emitted from nuclear states oriented by nuclear reactions or cryogenic methods. *Atomic Data and Nuclear Data Tables*, 11(5):351–406, 1973.

[54] A. Herzáň, S. Juutinen, K. Auranen, T. Grahn, P. T. Greenlees, K. Hauschild, U. Jakobsson, P. Jones, R. Julin, S. Ketelhut, M. Leino, A. Lopez-Martens, P. Nieminen, M. Nyman, P. Peura, P. Rahkila, S. Rinta-Antila, P. Ruotsalainen, M. Sandzelius, J. Sarén, C. Scholey, J. Sorri, and J. Uusitalo. Detailed spectroscopy of ^{193}Bi. *Phys. Rev. C*, 92:044310, Oct 2015.

[55] E. S. Paul, P. J. Woods, T. Davinson, R. D. Page, P. J. Sellin, C. W. Beausang, R. M. Clark, R. A. Cunningham, S. A. Forbes, D. B. Fossan, A. Gizon, J. Gizon, K. Hauschild, I. M. Hibbert, A. N. James, D. R. LaFosse, I. Lazarus, H. Schnare, J. Simpson, R. Wadsworth, and M. P. Waring. In-beam γ-ray spectroscopy above ^{100}Sn using the new technique of recoil decay tagging. *Phys. Rev. C*, 51:78–87, Jan 1995.

[56] C. Scholey. Recoil-isomer tagging techniques at ritu. In Juha Äystö, Peter Dendooven, Ari Jokinen, and Matti Leino, editors, *Exotic Nuclei and Atomic Masses*, pages 494–494, Berlin, Heidelberg, 2003. Springer Berlin Heidelberg.

[57] S. A. Gillespie, A. N. Andreyev, M. Al Monthery, C. J. Barton, S. Antalic, K. Auranen, H. Badran, D. Cox, J. G. Cubiss, D. O'Donnell, T. Grahn, P. T. Greenlees, A. Herzan, E. Higgins, R. Julin, S. Juutinen, J. Klimo, J. Konki, M. Leino, M. Mallaburn, J. Pakarinen, P. Papadakis, J. Partanen, P. M. Prajapati, P. Rahkila, M. Sandzelius, C. Scholey, J. Sorri, S. Stolze, R. Urban, J. Uusitalo, M. Venhart, and F. Weaving. Identification of a 6.6 μs isomeric state in ^{175}Ir. *Phys. Rev. C*, 99:064310, Jun 2019.

[58] E. Hagberg, P.G. Hansen, P. Hornshøj, B. Jonson, S. Mattsson, and P. Tidemand-Petersson. Alpha decay of neutron-deficient mercury isotopes and their daughters. *Nuclear Physics A*, 318(1):29–44, 1979.

[59] T. Kibédi, T.W. Burrows, M.B. Trzhaskovskaya, P.M. Davidson, and C.W. Nestor. Evaluation of theoretical conversion coefficients using bricc. *Nuclear Instruments and Methods in Physics Research Section A: Accelerators, Spectrometers, Detectors and Associated Equipment*, 589(2):202–229, 2008.

[60] M. Balogh, E. Jajčišinová, M. Venhart, A. Herzáň, J. L. Wood, D. T. Joss, F. A. Ali, K. Auranen, S. Bánovská, M. Bírová, R. J. Carroll, D. M. Cox, J. G. Cubiss, T. Davis, M. C. Drummond, P. T. Greenlees, T. Grahn, A. Gredley, J. Henderson, U. Jakobsson, R. Julin, S. Juutinen, G. Kantay, J. Konki, P. Konopka, M. Leino, V. Matoušek, A. K. Mistry, C. G. McPeake, D. O'Donnell, R. D. Page, J. Pakarinen, P. Papadakis, J. Partanen, P. Peura, P. Rahkila, P. Ruotsalainen, M. Sandzelius, J. Sarén, B. Sayg ı, M. Sedlák, D. Seweryniak, C. Scholey, J. Sorri, A. Špaček, S. Stolze, M. Taylor, A. Thornthwaite, J. Uusitalo, M. Veselský, S. Vielhauer, and F. P. Wearing. New collective structures in ^{179}Au and their implications for the triaxial deformation of the ^{178}Pt core. *Phys. Rev. C*, 106:064324, Dec 2022.

[61] P.M Davidson, G.D Dracoulis, T Kibédi, A.P Byrne, S.S Anderssen, A.M Baxter, B Fabricius, G.J Lane, and A.E Stuchbery. Non-yrast states and shape co-existence in light Pt isotopes. *Nuclear Physics A*, 657(3):219–250, 1999.

[62] S. Agostinelli, J. Allison, K. Amako, J. Apostolakis, H. Araujo, P. Arce, M. Asai, D. Axen, S. Banerjee, G. Barrand, F. Behner, L. Bellagamba, J. Boudreau, L. Broglia, A. Brunengo, H. Burkhardt, S. Chauvie, J. Chuma, R. Chytracek, G. Cooperman, G. Cosmo, P. Degtyarenko, A. Dell'Acqua, G. Depaola, D. Dietrich, R. Enami, A. Feliciello, C. Ferguson, H. Fesefeldt, G. Folger, F. Foppiano, A. Forti, S. Garelli, S. Giani, R. Giannitrapani, D. Gibin, J.J. Gómez Cadenas, I. González, G. Gracia Abril, G. Greeniaus, W. Greiner, V. Grichine, A. Grossheim, S. Guatelli, P. Gumplinger, R. Hamatsu, K. Hashimoto, H. Hasui, A. Heikkinen, A. Howard, V. Ivanchenko, A. Johnson, F.W. Jones, J. Kallenbach, N. Kanaya, M. Kawabata, Y. Kawabata, M. Kawaguti, S. Kelner, P. Kent, A. Kimura, T. Kodama, R. Kokoulin, M. Kossov, H. Kurashige, E. Lamanna, T. Lampén, V. Lara, V. Lefebure, F. Lei, M. Liendl, W. Lockman, F. Longo, S. Magni, M. Maire, E. Medernach, K. Minamimoto, P. Mora de Freitas, Y. Morita, K. Murakami, M. Nagamatu, R. Nartallo, P. Nieminen, T. Nishimura, K. Ohtsubo, M. Okamura, S. O'Neale, Y. Oohata, K. Paech, J. Perl, A. Pfeiffer, M.G. Pia, F. Ranjard, A. Rybin, S. Sadilov, E. Di Salvo, G. Santin, T. Sasaki, N. Savvas, Y. Sawada, S. Scherer, S. Sei, V. Sirotenko, D. Smith, N. Starkov, H. Stoecker, J. Sulkimo, M. Takahata, S. Tanaka, E. Tcherniaev, E. Safai Tehrani, M. Tropeano, P. Truscott, H. Uno, L. Urban, P. Urban, M. Verderi, A. Walkden, W. Wander, H. Weber, J.P. Wellisch, T. Wenaus, D.C. Williams, D. Wright, T. Yamada, H. Yoshida, and D. Zschiesche. Geant4—a simulation toolkit. *Nuclear Instruments and Methods in Physics Research Section A: Accelerators, Spectrometers, Detectors and Associated Equipment*, 506(3):250–303, 2003.

[63] F Dönau and S Frauendorf. *Proceedings of the Conference on High Angular Momentum Properties of Nuclei, Oak Ridge*. Harwood Academicm Chur, Swizerland,1982, 1982.

[64] Daniel Hojman, Miguel Cardona, D. Napoli, S. Lenzi, Jorge Davidson, M. Davidson, C. Ur, Greta Lo Bianco, C. Petrache, Michail Axiotis, D. Bazzacco, Mario De Poli, Giacomo de Angelis, E. Farnea, Thorsten Kröll, S. Lunardi, Nicolae Mărginean, T. Martı´nez, R. Menegazzo, and C. Alvarez. Signature inversion and deformation driving effects in ^{178}Ir. *Physical Review C*, 67, 02 2003.

[65] MO Kortelahti, EF Zganjar, HK Carter, CD Papanicolopulos, MA Grimm, and JL Wood. Nuclear systematics far from the line of beta stability: the low-lying excited states of 185,187,189 Au. *Journal of Physics G: Nuclear Physics*, 14(11):1361, 1988.

[66] A Andreyev. personal communication.

Appendix A

Appendix

Experimental Setup

Table A.1 Angular position for each detector in the JUROGAM II array. θ and ϕ are the vertical and horizontal angles respectively with respect to the beam direction.

Ring Number	Detector name	θ deg	ϕ deg
1	T01	157.6	0
1	T02	157.6	72
1	T03	157.6	144
1	T04	157.6	216
1	T05	157.6	288
2	T06	133.57	18
2	T07	133.57	54
2	T08	133.57	90
2	T09	133.57	126
2	T10	133.57	162
2	T11	133.57	198
2	T12	133.57	234
2	T13	133.57	270
2	T14	133.57	306
2	T15	133.57	342
3	Q01	104.5	15
3	Q02	104.5	45
3	Q03	104.5	75
3	Q04	104.5	105
3	Q05	104.5	135
3	Q06	104.5	165
3	Q07	104.5	195
3	Q08	104.5	225
3	Q09	104.5	255
3	Q10	104.5	285
3	Q11	104.5	315
3	Q12	104.5	345
4	Q13	75.5	15
4	Q14	75.5	45
4	Q15	75.5	75
4	Q16	75.5	105
4	Q17	75.5	135
4	Q18	75.5	165
4	Q19	75.5	195
4	Q20	75.5	225
4	Q21	75.5	255
4	Q22	75.5	285
4	Q23	75.5	315
4	Q24	75.5	345